

**ISTANBUL TECHNICAL UNIVERSITY ★ GRADUATE SCHOOL OF
SCIENCE ENGINEERING AND TECHNOLOGY**

**A COMPARATIVE NUMERICAL INVESTIGATION OF FLOW AROUND AN
AIRFOIL USED IN OFFSHORE TURBINES**

M.Sc. THESIS

Sertaç BULUT

Department of Naval Architecture and Marine Engineering

Naval Architecture and Marine Engineering Programme

AUGUST 2015

**ISTANBUL TECHNICAL UNIVERSITY ★ GRADUATE SCHOOL OF
SCIENCE ENGINEERING AND TECHNOLOGY**

**A COMPARATIVE NUMERICAL INVESTIGATION OF FLOW AROUND AN
AIRFOIL USED IN OFFSHORE TURBINES**

M.Sc. THESIS

**Sertaç BULUT
(508131019)**

Department of Naval Architecture and Marine Engineering

Naval Architecture and Marine Engineering Programme

Thesis Advisor: Prof. Dr. Selma ERGİN

AUGUST 2015

İSTANBUL TEKNİK ÜNİVERSİTESİ ★ FEN BİLİMLERİ ENSTİTÜSÜ

**OFFSHORE TÜRBİNLERDE KULLANILAN BİR RUZGAR KANADI PROFİLİ
ÜZERİNDEKİ HAVA AKIŞININ KARŞILAŞTIRMALI NUMERİK ANALİZİ**

YÜKSEK LİSANS TEZİ

**Sertaç BULUT
(508131019)**

Department of Naval Architecture and Marine Engineering

Naval Architecture and Marine Engineering Programme

Tez Danışmanı: Selma ERGİN

Anabilim Dalı : Herhangi Mühendislik, Bilim

Programı : Herhangi Program

AĞUSTOS 2015

Sertaç Bulut, a **M.Sc.** student of **ITU Graduate School of Science Engineering and Technology** student ID **508131019**, successfully defended the **thesis/dissertation** entitled “**A Comparative Numerical Investigation of Flow around an Airfoil Used in Offshore**”, which he prepared after fulfilling the requirements specified in the associated legislations, before the jury whose signatures are below.

Thesis Advisor : **Prof. Dr. Selma ERGİN**

İstanbul Technical University

Jury Members : **Prof. Dr. Şakir BAL**

İstanbul Technical University

Prof. Dr. Fahri ÇELİK

Yıldız Technical University

Date of Submission : 20 June 2015

Date of Defense : 03 August 2015

Anneme ve Babama,

FOREWORD

I would like to express my deep appreciation and thanks for my advisor, Prof.Dr. Selma Ergin and Prof.Dr. Moustafa Abdel-Maksoud for their time and interest in this thesis; and my loving family for their never-ending love, support and belief.

July 2015

Sertaç BULUT
Naval Arch. and Marine Eng.

TABLE OF CONTENTS

	<u>Page</u>
FOREWORD	ix
TABLE OF CONTENTS	xi
ABBREVIATIONS	xiii
LIST OF TABLES	xv
LIST OF FIGURES	xvii
ÖZET	xix
SUMMARY	xxiii
1. INTRODUCTION	1
1.1 Motivation.....	1
1.2 Objectives and Content.....	3
2. WIND ENERGY	6
2.1 Wind	10
2.1.1 The local effects	11
2.1.2 Wind shear	12
2.1.3 Turbulence	13
2.1.4 Acceleration effect	15
2.1.5 Time variation	16
2.2 Wind Turbines Technology.....	17
2.2.1 Components of a wind turbine	17
2.2.2 Classification of wind turbines	19
2.2.3 Historical development of the wind turbines	22
2.2.4 Offshore wind turbines.....	23
2.2.5 Advantages and disadvantages.....	24
2.2.6 Offshore wind technology development	25
3. GEOMETRIC AND AERODYNAMIC CHARACTERISTICS OF AIRFOILS	35
3.1 Airfoil Geometry and Nomenclature	35
3.2 Aerodynamic Properties.....	37
3.2.1 Angle of attack	37
3.2.2. Lift characteristics	38
3.2.3. 2-D moment	41
3.2.4 Aerodynamic center	42
3.2.5 Center of pressure	43
3.3 The NACA Airfoils.....	45
3.4 An Overview of NACA 6-digit airfoil series	46
4. THEORETICAL BACKGROUND	49
4. 1 Underlying Method For <i>panMARE</i>	49
4.1.1 Boundary element method	49
4.1.2 Numerical formulation	50
4.2 Aspects Regarding the <i>Ansys CFX</i> Process.....	52
4.2.1 Model creation	53
4.2.2 Boundary conditions	54
4.2.3 Domain decomposition	57
4.2.4 Grid generation	57
4.2.5 Solver	61
4.2.6 Post-processing	62

5. RESULTS.....	63
5.1. <i>Ansys CFX</i> Analysis	63
5.2 panMARE Analysis.....	77
5.3 Comparison Between The Experimental Data And Numerical Values	83
5.4 Cell Count Dependence Study.....	89
6. CONCLUSIONS AND RECOMMENDATIONS.....	91
REFERENCES.....	93
CURRICULUM VITAE.....	95

ABBREVIATIONS

A	:Cross- sectional area of stream, (m ²)
a	:Axial induction factor
a'	:Angular induction factor
α	: Empirical wind shear exponent
AR	:Aspect ratio.Span length divided by chord width
α_{stall}	:Attack angle at stall, (8degree)
B	:Blade number
BEM	:Blade element momentum
C	:Chord length, (m)
C_D	:Drag coefficient.Ratio of the drag force to the dynamic pressure for unit span area, $D/(\rho V^2 A)$.
C_{D stall}	:Drag coefficient at stall
C_L	:Lift coefficient. Ratio of the lift force to the dynamic pressure for unit span area, $L/(\rho V^2 A)$.
C_{L stall}	:Lift coefficient at stall
C_p	:Power coefficient
C_{p, rat}	:Rated power coefficient
D	:Drag force, (N)
dr	:Annulus width, (m)
Φ	:Inflow angle,(degree)
F	:Correction factor
F_{Hub}	:Hub correction factor
F_{Tip}	:Tip correction factor
F_{Total}	:Total correction factor
H₀	:Surface roughness length, (m)
L	:Lift force, (N)
λ	:Tip speed ratio
λ_r	:Local tip speed ratio
ν	:Kinematic viscosity of air (m ² /s)
NACA	:National Advisory Committee for Aeronautics
P_D	:Power calculated by actuator disc theory, (Watt)
PFC	:Power factor correction
P_{rat}	:Rated power, (Watt)
P_{tot}	:Total power, (Watt)
P_w	:Power calculated by energy theory, (Watt)
P_{w0}	:Power in free stream wind, (Watt)
Q	:Torque, (N.m)
r	:Radial position, (m)
ρ	:Incoming wind density, (kg/m ³)
rpm	:Revolution per minute
T	:Thrust, (N)
U	:Wind speed at rotor surface, (m/s)
V₂	:Far stream wind velocity, (m/s)
V_a	:Wind speed at height "a", (m/s)
V_b	:Wind speed at height "b", (m/s)
V_{total}	:Local velocity component, (m/s)
V_w	:Free stream wind velocity, (m/s)
Ω	:Turbine angular velocity, (rad/s)

ω	:Induced angular velocity, (rad/s)
A	:Angle of attack,(degree)
B	:Pitch angle, (degree)
\dot{m}	:Mass-flow rate, (kg/s)

LIST OF TABLES

	<u>Page</u>
Table 2.1: Typical values of roughness length z_0 and roughness exponent α for different types of surfaces.....	13
Table 2.2 : Number of turbines and MW fully connected to the grid during 2013 per country (2013).....	28
Table 5.1: Lift and drag coefficients ($Re=4.22 \times 10^4$).....	64
Table 5.2: Lift and drag coefficients ($Re=1.6 \times 10^5$).....	66
Table 5.3: Lift and drag forces ($Re=4.22 \times 10^4$) (panMARE).....	82
Table 5.4: Comparisons between calculated and experimental aerodynamic coefficients, lift coefficient.....	88
Table 5.5 : Comparisons between calculated and experimental aerodynamic coefficients, drag coefficient.....	89

LIST OF FIGURES

	<u>Page</u>
Figure 2.1: New renewable power capacity additions by technology, 2004-2013.....	7
Figure 2.2: Wind power capacity in the world, 2014.....	7
Figure 2.3: Wind energy impact on avoiding carbon dioxide emissions.....	8
Figure 2.4: Representation of the extreme environmental conditions for a offshore wind turbine (in case a floating turbine).....	9
Figure 2.5 : Wind direction affected by the coriolis force.....	11
Figure 2.6: Variation of wind velocity with height.....	12
Figure 2.7 : Variation of wind velocity with height.....	14
Figure 2.8 : The acceleration effect over ridges.....	15
Figure 2.9 : Time variation of wind velocity.	17
Figure 2.10: Diagram of a wind turbine.....	18
Figure 2.11: Blade shape and cross sections.....	19
Figure 2.12: Vertical wind turbine.....	20
Figure 2.13: Horizontal wind turbine.....	21
Figure 2.14: Windmill (Dutch ground windmill) with spring sails	22
Figure 2.15: Offshore wind turbines.....	24
Figure 2.16: Share of annual offshore wind capacity installations per country (MW) (2013).....	27
Figure 2.17: Share of consented offshore capacity per country (MW) (2014).....	28
Figure 2.18: Share of offshore wind farms under construction by sea basin(MW)..	29
Figure 2.19: Technology progression for offshore wind turbines	29
Figure 2.20: Cost of offshore wind turbine substructures with water depth.....	30
Figure 2.21: Floating deepwater platform concepts.....	31
Figure 3.1 : Basic nomenclature of an airfoil.....	36
Figure 3.2 : Angle of attack.	37
Figure 3.3 : Lift coefficient vs angle of attack.....	38
Figure 3.4 : Angle of attack, coefficient of drag and coefficient of lift.	40
Figure 3.5 : 2-D moment.....	41
Figure 3.6 : Centre of pressure.....	43
Figure 3.7 : Drag coefficient.	44
Figure 3.8 : Drag coefficient – mach numbers.....	44
Figure 3.9 : NACA 64(3)618 profile.	47
Figure 4.1 : Discretisation of a propeller blade and wake	50
Figure 4.2 : Centre, collocation and node points on a blade profile	51
Figure 4.3: Surface representation of NACA 643618 airfoil.....	53
Figure 4.4: Stations and ordinates given in percent of airfoil chord for NACA-64 ₃ 618.....	54
Figure 4.5: Schematic representation of boundary conditions.....	55
Figure 4.6: The circular domain around the blade profile.	56
Figure 4.7: The representation of the outer domain.....	56

Figure 4.8: Domain decomposition in Ansys CFX.	57
Figure 4.9: A typical 2D structured grid consisting of rectangular elements.....	58
Figure 4.10: A 3D unstructured grid around a finite cylinder consisting of tetrahedral elements.	59
Figure 4.11: Unstructured mesh consisting of 2 million tetrahedral elements around a wind turbine rotor.....	60
Figure 4.12: Surface mesh showing triangular elements on a wind turbine blade. ...	60
Figure 5.1: Lift coefficient vs angle of attack ($Re=4.22 \times 10^4$).	65
Figure 5.2 Lift coefficients for reynolds numbers 1.6×10^5 and 4.22×10^4	65
Figure 5.3 Drag coefficients for reynolds numbers 1.6×10^5 and 4.22×10^4	66
Figure 5.4: The changing of the C_L/C_D via angle of attack.....	67
Figure 5.5 : Static pressure at zero degree(Ansys CFX).	67
Figure 5.6 : Dynamic pressure at zero degree(Ansys CFX).	68
Figure 5.7 : Total pressure at zero degree(Ansys CFX).	68
Figure 5.8 : Velocity at zero degree (Ansys CFX).	69
Figure 5.9 : Flow turbulence on the airfoil at zero degree(Ansys CFX).	69
Figure 5.10 : Static pressure at five degrees(Ansys CFX).	70
Figure 5.11 : Dynamic pressure at five degrees(Ansys CFX).	70
Figure 5.12 : Total pressure at five degrees (Ansys CFX).	71
Figure 5.13 : Velocity at five degrees (Ansys CFX).	71
Figure 5.14 : Flow turbulence on the airfoil at five degrees (Ansys CFX).	72
Figure 5.15 : Static pressure at ten degrees (Ansys CFX).	72
Figure 5.16 : Static pressure at ten degrees (Ansys CFX).	73
Figure 5.17 : Total pressure at ten degree (Ansys CFX).	73
Figure 5.18 : Velocity at ten degrees (Ansys CFX).	74
Figure 5.19 : Flow turbulence on the airfoil at ten degrees (Ansys CFX).	74
Figure 5.20 : Static pressure at fifteen degrees (Ansys CFX).	75
Figure 5.21 : Dynamic pressure at fifteen degrees (Ansys CFX).	75
Figure 5.22 : Total pressure at fifteen degrees (Ansys CFX).	76
Figure 5.23 : Velocity at fifteen degrees (Ansys CFX).	76
Figure 5.24 : Flow turbulence on the airfoil at fifteen degrees (Ansys CFX).	77
Figure 5.25 : The coordinates of the airfoil NACA64(3)618.	78
Figure 5.26: An example of panMARE code.	79
Figure 5.27: The velocity distrubition at zero degree (panMARE).	80
Figure 5.28: The pressure distrubition at 5 degrees (panMARE).	81
Figure 5.29: The force distrubition at 5 degrees (panMARE).	81
Figure 5.30: Drag coefficients for reynolds numbers 1.6×10^5 and 4.22×10^4 (panMARE).	82
Figure 5.31: Lift coefficients for reynolds numbers 1.6×10^5 and 4.22×10^4 (panMARE).	83
Figure 5.32: The comparison of the lift coefficients ($Re=4.22 \times 10^4$).	84
Figure 5.33: The comparison of the lift coefficients ($Re=1.6 \times 10^5$).	84
Figure 5.34: The comparison of the drag coefficients ($Re=4.22 \times 10^4$).	85
Figure 5.35: The comparison of the drag coefficients ($Re=1.6 \times 10^5$).	86
Figure 5.36: Lift coefficient Comparison of NACA 64 ₃ -618($Re = 1,6 \times 10^5$).	87
Figure 5.37: Drag Coefficient Comparison of NACA 64 ₃ -618($Re = 1,6 \times 10^5$).	88
Figure 5.38: Mesh dependence study for the NACA64 ₃ 618.	90

OFFSHORE TÜRBİNLERDE KULLANILAN BİR RUZGAR KANADI PROFİLİ ÜZERİNDEKİ HAVA AKIŞININ KARŞILAŞTIRMALI NUMERİK ANALİZİ

ÖZET

Son yıllarda, artan çevresel kaygılar ve enerji temini sürekliliği konuları sebebiyle, yenilenebilir enerji kaynakları büyük önem kazanmaya başlamıştır. Rüzgar enerjisi ise, bu yenilenebilir enerji kaynaklarından en önemlileri arasında yer alır. Bu anlamda rüzgar enerjisinde yapılan yatırımlar, özellikle son on yıl içerisinde büyük artış kazanmıştır. Açık deniz (offshore) rüzgar teknolojisi ise, rüzgar enerjisi alanında kullanılmaya başlanmış olan yeni bir teknolojidir. Bu teknolojinin karasal rüzgar sistemlerine göre avantajları bulunmaktadır. Açık denizlerde daha güçlü ve düzenli rüzgârların oluşu, yerleşim alanlarındaki gürültü ve görüntü kirliliğinin azaltılması, doğaya verilen olumsuz etkilerin daha az olması, kurulum aşamasındaki taşıma kolaylığı ve enerji iletim verimliliği yatırımcıları bu alana yönelten faktörler arasında sayılabilir. Bu anlamda açık deniz rüzgar enerjisi karasal alandaki uygulamaların yanında, özellikle Almanya ve İngiltere olmak üzere Avrupa’da büyük bir büyüme oranına sahip olmuştur. Kuzey Denizi başta olmak üzere Baltık Denizi ve Atlantik Okyanusu’nda yaygın olarak kullanım alanı bulan açık deniz rüzgar sistemleri, önemli avantajlarıyla rüzgar enerjisinin bir sonraki adımı, yani bu alanda geleceğin enerji çözümü olarak görülmektedir.

Rüzgar türbinlerinin performansında şüphesiz ki kanat aerodinamik yapısının büyük bir etkisi bulunmaktadır. Kanat profili üzerine etkiyen kuvvetler; havanın hızı, havanın yoğunluğu, profil alanı, profil geometrisi, profil yüzey pürüzlülüğü, havanın viskozitesi ve hücum açısı gibi değişkenlere göre farklılık göstermektedir. Bu kuvvetlerden en önemlisi olarak görülen taşıma kuvveti ise kanat alanı, kamburluk, hücum açısı ve havanın hızı faktörlerinin etkisi altında değişir. Bu çalışmada, hücum açısı ve hava hızının kanat profili üzerindeki hava akışına etkileri incelenmiştir.

Çalışmada, son zamanlarda offshore rüzgar türbinlerinde de geniş bir kullanım alanı olan NACA 64₃618 kanat profilinin numerik analizi ele alınmaktadır. Analizler farklı hesaplama metotlarına dayanan Ansys CFX ve panMARE programları ile gerçekleştirilmiştir. Yapılan analiz sonuçları, kullanılan kanat profili ile ilgili yapılmış deney verileri ile karşılaştırılmış ve buna göre elde edilen sonuçlar üzerine değerlendirilmelerde bulunulmuştur.

Tez dökümanı altı ana bölümden meydana gelmektedir. İlk bölümde; dünya üzerindeki yenilenebilir enerji kaynaklarına olan yönelimden ve rüzgar enerjisinden genel olarak bahsedilmiştir. Yapılan çalışmanın içeriği, aşamaları ve hedeflenen noktalar sunulmuştur. Bir sonraki bölümde; rüzgarların oluşumunda etkili olan faktörlere değinilmiş, son yıllardaki rüzgar enerjisinin gelişimi, rüzgar türbinleri elemanları ve açık deniz rüzgar teknolojisi ele alınmıştır. Üçüncü bölüm ise rüzgar kanadı geometrisi ve aerodinamik özellikleri hakkında bilgi vermekte, ayrıca özel olarak NACA profillerinin yapısı ve kullandığımız NACA 6 serisi özelliklerine de yer vermektedir. Dördüncü bölümde, kullanılan analiz programları olan Ansys CFX ve panMARE’nin

dayandığı metotlar ve analiz aşamaları incelenmiştir. Bu kapsamda, Ansys CFX’de yapılan analiz aşamaları modelin oluşturulması, sınır şartlarının belirlenmesi, mesh işleminin gerçekleştirilmesi, analizin çözümlenmesi ve çözücü modülün ayarlarının yapılması, analiz verilerinin tablolar halinde ve görsel olarak görüntülenmesi gibi bölümlerde detaylı olarak ele alınmıştır. Bir sonraki bölümde, yapılan analizlerin sonuçları farklı rüzgar hızları ve farklı hücum açıları için grafikler şeklinde düzenlenerek sunulmuştur. Ansys CFX analizi için, farklı hücum açılarındaki rüzgar hızı, statik basınç, dinamik basınç ve türbülans dağılımları, boyutsuz katsayıların hücum açısına göre değişimleri bu bölümde incelenmiş; veriler panMARE programının verileri ile karşılaştırılmıştır. Daha sonra bu iki analiz verileri, deneysel sonuçlar ile karşılaştırılarak, verilerin doğruluk dereceleri incelenmiştir. Son bölüm olan altıncı bölümde ise, karşılaştırılmalı grafik ve tablolara, verilerin değerlendirilmesi ve öneriler kısmına yer verilmiştir.

Bu çalışmada, NACA 64₃618 kanat profilinin etrafındaki hava akışı, -5° ile 15° açıları arasında bir hücum açısı aralığında incelenmiştir. Hücum açısı değişimlerinin, kanat profili için taşıma ve sürüklenme katsayısı üzerindeki etkilerine bakılmıştır. Analiz metotları deneysel verilerle karşılaştırılmış, sonuçların doğruluk dereceleri incelenmiştir. Ayrıca, analizler sırasında 3 m/sn ve 11,4 m/sn olmak üzere iki farklı rüzgar hızı kullanılmıştır. Bu kapsamda, rüzgar hızı değişiminin de kanat profili etrafındaki hava akışına etkileri gözlenmektedir.

Öncelikle Ansys CFX programına dayalı sayısal analiz gerçekleştirilmiştir. Kanat geometrisi modelinin oluşturulması bu analizin ilk aşamasını oluşturmaktadır. Üretici firmanın sunduğu kaynaklardan yararlanarak Ansys Design Modeller modülünde kanat geometrisi elde edilmiştir. Sonraki aşamada kanat profilini de içerisine alan analiz sistemi kurulmuştur. Bu aşamada iki farklı analiz alanı kullanılmıştır. Bu alanlardan içtekinе, her hücum açısı değişiminde kanat profili ile birlikte dönme hareketi verilmiş; bunun aksine dıştaki alan ise sabit tutulmuştur. Bu sayede her bir hücum açısı değişimi için hesap kolaylığı sağlanarak, işlem hızı arttırılmıştır. Analiz alanları oluşturulduktan sonra, sistem sınır şartları belirlenmiştir. Sınır şartı olarak, havanın giriş yaptığı bölge “inlet”, havanın çıkış yaptığı bölge “outlet”, sistem dış alanı alt ve üst duvarları ile kanat profili “wall” ve sistem dış alanı ile iç alanı arasında kalan bölge “symmetry” sınır şartı olarak tanımlanmıştır. Analiz ayarları tamamlandıktan sonra, sistem Ansys CFX çözücü modülünde çözdürülmüştür. Yapılan işlemlerde 1×10^{-6} mertebesinde hassasiyet kullanılmıştır. Sonuçlar, dinamik ve statik basınç dağılımları, hız dağılımları ve kuvvet dağılımları olarak Ansys CFX Post bölümünden elde edilmiş, bu veriler ışığında boyutsuz katsayılar hücum açısı değişimleri ve hız değişimlerine göre hesaplanmıştır. Aynı şekilde bu hesaplamalar aynı değişkenler için panMARE programında tekrarlanmıştır. Sistem aynı değişken aralığında, programın kendi kod sistemine uygun bir şekilde panMARE içerisinde tanımlanmıştır. İlgili kodun oluşturulması hesaplamalarda en uzun zamanı alan bölümdür. Bu aşamada Python programlama dili kullanılmıştır. Analizle ilgili kodun oluşturulmasından sonra, sistemin çözdürülmesi Ansys CFX programına nazaran çok daha kısa bir süre almaktadır. Analiz sonuçları, panMARE programı ve Paraview yazılımı kullanılarak elde edilmiştir.

Her iki programla yapılan analizler tamamlandıktan sonra, elde edilen veriler deneysel sonuçlar ile karşılaştırılmıştır. Bu karşılaştırma sonunda her bir analizin hata oranları her bir hücum açısı için belirlenmiştir.

Yapılan Ansys CFX sayısal simülasyonunda, NACA 64₃618 kanat profilinin hücum açısı -5°'den 10°'ye kadar arttırıldığında, profilin taşıma katsayısı değerinin düzenli bir şekilde arttığı, 11°'lik hücum açısında ise (ayrılma durumunun meydana geldiği nokta) ani bir azalma gösterdiği gözlemlenmiştir. Kanat profili hücum açısı -5°'den 11°'ye arttırıldığında, profilin sürüklenme katsayısı değerinin düzenli bir artış gösterdiği, 11°'lik hücum açısından sonra ise sürüklenme katsayısındaki artışın ivmesinin arttığı görülmüştür.

Anahtar Kelimeler: Kanat profili, NACA 643618, hücum açısı, panMARE, Ansys CFX

A COMPARATIVE NUMERICAL INVESTIGATION OF FLOW AROUND AN AIRFOIL USED IN OFFSHORE TURBINES

SUMMARY

It is obvious that renewable energy has started to gain more importance in the recent years with increasing concerns about environmental issues and security of energy supply. Wind energy is one of the most important sources in renewable energy. Having much more growth rate than onshore and with numerous advantages, offshore wind energy is believed to be next step in wind energy and the energy solution of the future. The research conducted in this thesis is motivated by the numerical analysis of NACA 64(3)618 blade profile of the offshore wind turbines which has been widely used in the wind energy sector recently. These analyses have been carried out by Ansys CFX and panMARE working according to different calculation methods. The effects of changing of the angle of attack on lift and drag coefficients have been examined for the blade profile. The numerical studies have been performed between -5° and 15° in different values of angle of attack. Besides, two different wind velocity (3 m/s and 11.4 m/s) are used in these studies. By this means, the effects of the altering wind velocity on the airflow around the blade profile have been investigated.

The research report is composed of six chapters. In the first two sections, the information related to offshore wind turbine technology and wind energy are handled and also the scope of the thesis and the purpose are mentioned. After examining the key factors that effect wind energy in detail, the geometry and aerodynamics of airfoil and the characteristics of NACA profiles are discussed in the third part. Additionally, the information about the underlying methods of Ansys CFX and panMARE programs and their solution methods are presented. The fifth section covers the numerical analyses of NACA 64(3)618 airfoil by Ansys CFX and panMARE and the comparison of the results between these analyzers. The conclusion part and recommendations are addressed with key factors in the last part of the thesis.

Key Words: Blade profile, NACA 643618, angle of attack, panMARE, Ansys CFX

1. INTRODUCTION

Although there are numerous factors that drive the use of wind energy throughout the world, three among them dominantly impose the utilization of wind energy. First factor is the limited amount of fossil fuel resources. Energy demand has increased tremendously proportional to the population growth and technological developments. Although fossil fuels are the main energy resource, they are neither capable of meeting all energy requirement nor they are distributed evenly throughout the world. Due to these reasons, fossil fuel prices frequently become unstable generating many oil crisis situations. As a result, countries have been seeking for alternative energy resources that are both easily accessible and sustainable.

Another factor for the increased trend in the utilization of wind energy is the danger of global warming caused by the increased amount of greenhouse gases in the atmosphere due to the burning of fossil fuels. Kyoto Protocol, which targets to reduce the harmful gases in the atmosphere, has been accepted by many countries today. Reduction of atmospheric pollution can be achieved by utilization of green energy resources such as solar, wind and hydrodynamic energy.

Final factor is the need for potentially available and cheap energy resources. Wind energy is a favorable resource since it is available commonly and it is free. All these three factors bring out the wind energy as an alternative resource to fossil fuels in terms of being cheap, clean and potentially available[1].

1.1 Motivation

The rapidly depleting energy resources all over the world are a major cause of concern for mankind. These energy resources primarily the fossil fuels are also responsible for the fast global climate change. The Energy Information Administration estimates that about 86 percent of the world's total energy production results from the burning of fossil fuels[1]. Fossil fuels take millions of years to form, but in order to cater to the growing energy needs of the world, these reserves are being utilized at a much faster rate than they were created. Such is the rate of consumption of fossil fuels that the time seems near when these valuable sources of energy will be depleted.

A closer look at some numbers will be helpful in understanding this problem. Estimates from the U.S. Dept. of Energy predict that the years of production left in the ground for oil is 43 years, gas 167 years, and coal 417 years [2]. This has led to the growing demand of renewable sources of energy production. Another major concern over the use of fossil fuels is the emission of tremendous amounts of harmful gases into the atmosphere. Burning of fossil fuels results a net increase of 10.65 billion tonnes of atmospheric carbon monoxide every year which deteriorates the environmental balance. Therefore a need for clean and renewable sources of energy has been felt[3].

Large amounts of research and resources are being spent today in order to harness the energy from wind effectively. Wind energy as a source of energy is being favoured widely as an alternative to fossil fuels, as it is plentiful, renewable, widely distributed, clean, and produces no greenhouse gas emissions. Wind turbines convert kinetic energy from the wind into mechanical energy which can be used to generate electricity. They are clean and inexpensive devices. Largest devices to date are capable of delivering upto 6MW power. However, the air flow environment in which wind turbines operate presents them with numerous challenges. Wind turbines experience large changes in angle of attack, atmospheric turbulence, wakes from the previous turbine in a wind farm, tower wakes, etc. Therefore, whenever a wind turbine is designed or a wind farm is being setup, all the above factors must be considered[4].

Winds can be broadly classified as planetary and local. Planetary winds are caused by greater solar heating of the earth's surface near the equator than near the northern or southern poles. This causes warm tropical air to rise and flow through the upper atmosphere toward the poles and cold air from the poles to flow back to the equator nearer to the earth's surface. The direction of motion of planetary winds with respect to the earth is affected by the rotation of the earth. The western motion toward the equator and the eastern motion toward the poles result in large counterclockwise circulation of air around low-pressure areas in the northern hemisphere and clockwise circulation in the southern hemisphere[5].

Local winds are caused by two mechanisms. The first one is differential heating of water and land. Solar insolation during the day is readily converted to sensible energy of the land surface and partly consumed in evaporating some of that water. The landmass becomes hotter than the water, which causes the air above land to heat up

and become warmer than the air above water. The warmer lighter air above the land rises, and the cooler heavier air above the water moves in to replace it. This is the mechanism of shore breezes. At night, the direction of the breezes is reversed because the landmass cools more rapidly than the water. Hills and mountain sides cause the second mechanism of local winds. The air above the slopes heats up during the day and cools down at night, more rapidly than the air above the low lands. This causes heated air during the day to rise along the slopes and relatively cool heavy air to flow down at night.

Winds are very much influenced by the ground surface at altitudes up to 100 meters. The wind will be slowed down by the earth's surface roughness and obstacles. Wind speeds are affected by the friction against the surface of the earth. In general, the more pronounced the roughness of the earth's surface; the more the wind will be slowed down. Forests and large cities obviously slow the wind down considerably, while concrete runways in airports will only slow the wind down a little. Water surfaces are even smoother than concrete runways, and will have even less influence on the wind, while long grass and shrubs and bushes will slow the wind down considerably[6].

In offshore environments the winds are typically stronger and are more sustained than inland, providing a more reliable source of energy. Increased wind speeds also imply that the blades of much larger diameter (120–190 m) must be designed and built for better performance. These are significant engineering challenges that must be addressed through advanced research and development, which also involves large-scale advanced simulation.

The air flow Reynolds number is of the order of 10^7 – 10^8 , which is challenging in terms of both flow modeling and simulation. This Reynolds number necessitates the use of fine grids, good quality basis functions, and large-scale high-performance computing. Wind turbine blades are long and slender structures that are made of several structural components with complex distribution of material properties, requiring both advanced computational model generation and simulation methods. The numerical approach for structural mechanics must have good accuracy and avoid locking[7].

1.2 Objectives and Content

In this thesis, primarily the wind energy and the wind turbines in literature are studied, and then some information about new wind turbine technologies are given in more

detail. At this point, offshore wind turbines, which are one of the latest technologies in wind energy sector, are worked on and the advantages of these turbines are mentioned.

Blade geometry and the air flow around the airfoil are crucial in terms of the efficiency of the wind turbines. In this prospect, in the course of numerical analyses, a blade profile used also in offshore wind turbines was examined. These analyses have been implemented in this research for a certain range of angle of attack and varied wind speeds. The purpose here is to evaluate the effects of the variables mentioned above on the air flow around the blade profile. The numerical solutions were carried out by using different calculation methods, such as panel methods and RANS methods. The other purpose here is to investigate the accuracy of the panMARE simulation tool, which solves the equations faster than Ansys CFX by means of its panel structures.

By using the datas related to the change of pressure, velocity and force distributions coupled with angle of attack and by adding three dimensional analyses to this study, a model to understand and absorb the undesirable effects of the wave motion on the efficiency of the wind turbines can be developed in future.

The first analysis was performed by Ansys Cfx based on RANS solvers. The angle of attack were altered for the airfoil and the target here is to examine the influence by the pitching motion of blade on pressure, velocity and force variants. The nondimensional coefficients were calculated with these variables obtained by the analyses in the end. In addition, examining the alternation of the wind acting on the blade is the other target of the study. In this respect, two different air velocity values were used for the analyses.

It is the second analysis that enables to solve equation faster by using parallel panels in the panMARE software. Writing the computer program getting to calculate desired values is the part taking most time for panMARE. The panel method has a better computation speed than Ansys CFX; however, the accuracy of this method is required to control by comparing other methods or experimental datas. At this point, another aim of the research is defined by the checking the stability of the panMARE. The same values are used as defined in the Ansys CFX for the angle of attack and air velocity. During the analyses, the results of each computation tool has been reviewed whether this method meets the requirements for accuracy or not. At the end of the section, the solution interval which panMARE gives good accuracy and and reliability was

defined. The limits that the deviations began for the analyzer and its reasons were determined. The last section of the thesis consists of the conclusion part and suggestions.

2. WIND ENERGY

The last decade (2004 – 2014) saw a steady increase in the global demand for renewable energy. While overall primary energy supply from renewables in 2004 was 57.7 EJ(exajoules) per year, by 2013 the total supply had grown to 76 EJ annually—an overall increase of 30%. By 2013, renewables supplied approximately 19% of the world’s final energy consumption, a little less than half of which came from traditional biomass.

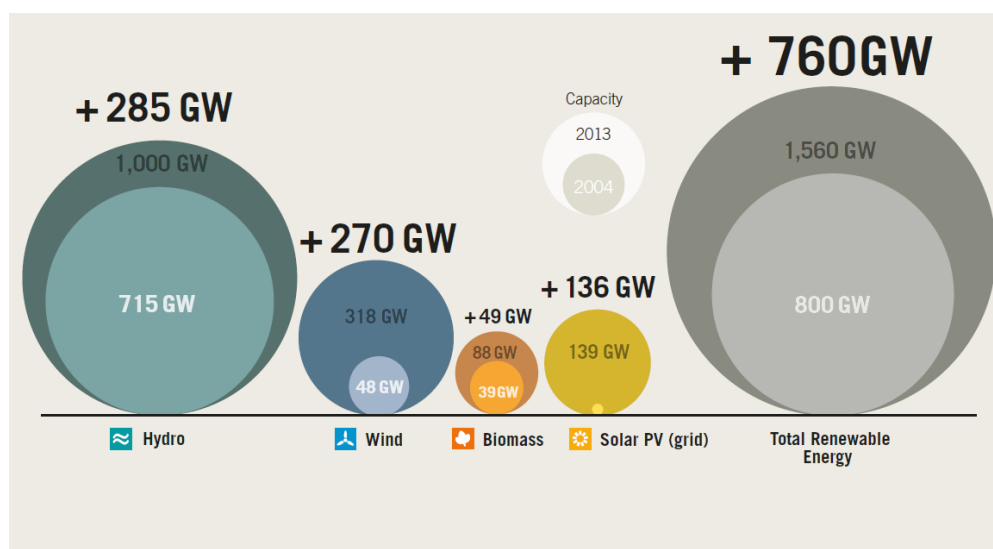


Figure 2.1: New renewable power capacity additions by technology, 2004-2013[9].

Figure 2.1 shows that by the end of 2013 cumulative global wind capacity was 318 GW, an increase of 270 GW since 2004. However in 2013, after more than 20 years of steady growth, the annual wind market dropped for the first time; down 10 GW to 35.5 GW. This decline was due primarily to the steep drop in US installations, from 13 GW in 2012, to just over 1 GW in 2013. The failure of the US Congress to re-authorise the US Production Tax Credit, which expired end- 2012, effectively killed the 2013 market. The United States— which was the largest global market from 2006 to 2008 and in 2012—fell to sixth place behind Canada. However it is likely that it will rise again in 2014; this time to second place behind China[8].

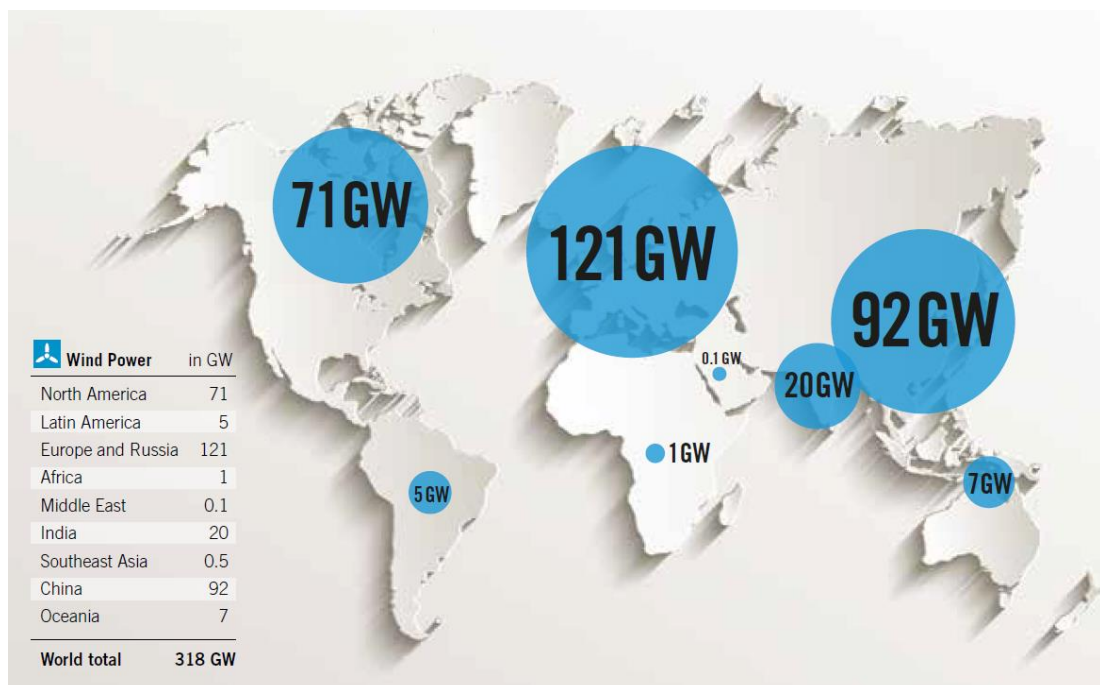


Figure 2.2: Wind power capacity in the world, 2014[8].

It can be seen in Figure 2.2 that elsewhere wind power is expanding. While the roots of the modern wind power industry are in Denmark, Germany and the United States, 2004 saw the wind market spread. From 2004 to 2010 China doubled its wind installations annually from 0.5 GW to 19 GW. It led in annual, yearly installations (except in 2012) and held the top spot in 2011 in terms of cumulative installations. Although the Chinese market dipped to just below 13 GW in 2012, it grew to 16 GW in 2013 and is back on an upward trajectory. In addition to Europe, China, and the United States, Canada, Brazil and India have become important markets with Mexico and South Africa growing rapidly. Falling prices due to high competition and

technology improvements make wind power an economically feasible power generation technology competing directly with heavily subsidised fossil fuels in an increasing number of markets. As of 2014 over 240,000 wind turbines are operating in more than 90 countries[8].

Human activity is overloading our atmosphere with carbon dioxide and other global warming emissions, which trap heat, steadily drive up the planet’s temperature, and create significant and harmful impacts on our health, our environment, and our climate. Electricity production accounts for more than one-third of U.S. global warming emissions, with the majority generated by coal-fired power plants, which produce approximately 25 percent of total U.S. global warming emissions; natural gas-fired power plants produce 6 percent of total emissions . In contrast, most renewable energy sources produce little to no global warming emissions.

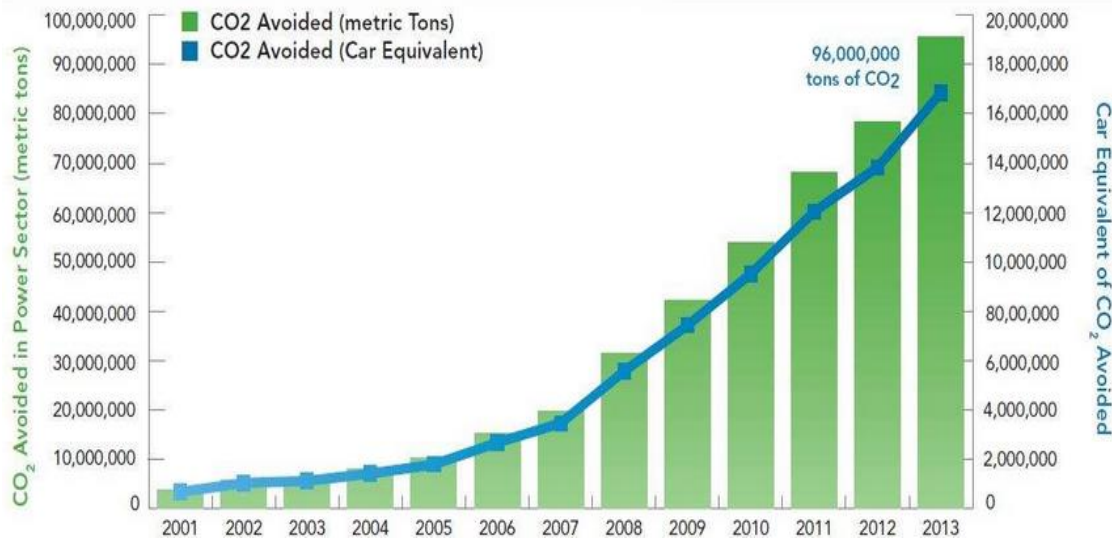


Figure 2.3: Wind energy impact on avoiding carbon dioxide emissions[8].

Figure 2.3 indicates that in 2013, the roughly 168 million megawatt-hours (MWh) generated by wind energy delivered 4.1% of U.S. generation and avoided over 96 million metric tons of carbon dioxide (CO2) -- the equivalent of reducing power-sector CO2 emissions by 4.4%, or taking over 16 million cars off the road.

Adding the 12,000 MW of wind capacity under construction at the end of 2013, U.S. wind power capacity will avoid over 117 million tons of CO2 annually when those projects are completed -- the equivalent of reducing power-sector CO2 emissions by 5.3%, or taking over 20 million cars off the road.

On average across the regions of the U.S., wind generation today will avoid roughly 0.6 metric tons (1,300 pounds) of CO₂ for every megawatt-hour (MWh) of wind generation produced. This means a single typical wind turbine of average size would avoid over 3,500 metric tons of CO₂ annually, the equivalent of taking more than 600 cars off the road.

To produce the same amount of electricity that today's U.S. wind turbine fleet (over 61,108 MW) generated during 2013 would require burning over 87 million tons of coal (8,900 miles of railcars) or 318 million barrels of oil each year[9].

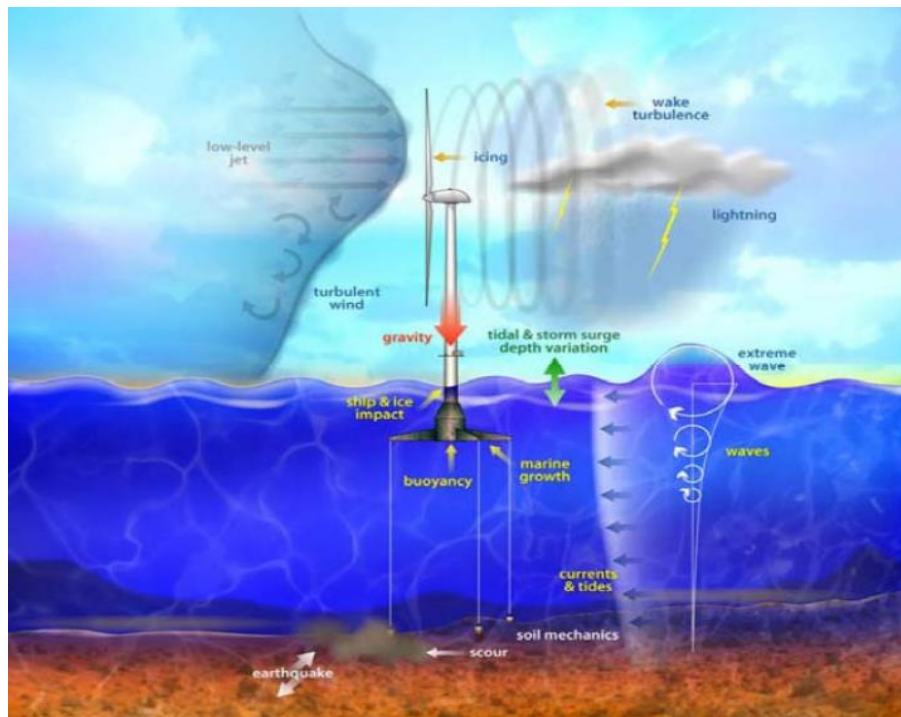


Figure 2.4: Representation of the extreme environmental conditions for a offshore wind turbine (in case a floating turbine)[9].

The main difference between offshore and onshore is the support structure, with respect to the technological specificity of the marine foundation. This is fundamental for a preliminary evaluation of the seabed. Another different element, compared to onshore sites, is the wind velocity that is higher and more constant (so more predictable) and is associated with a lower turbulence. This favorable wind condition allows offshore wind turbines to produce more electrical energy than onshore ones with the same rated power (the Capacity Factor is higher offshore). However a more intense state of stress is created on the turbines. In fact offshore there are extreme environmental conditions, because of waves, strong storms and brackish water (illustrated in Figure 2.4), which force wind turbines constructors to raise the necessary

structural requirements, in particular concerning with the innovative floating turbines designed for large water depths[9],[10].

2.1 Wind

The world receives around 1.7×10^{14} kW of power from the sun in the form of solar radiation. This radiation heats up the atmospheric air. The intensity of this heating will be more at the equator (0° latitude) as the sun is directly overhead. Air around the poles gets less warm, as the angle at which the radiation reaches the surface is more acute. The density of air decreases with increase in temperature. Thus lighter air from the equator rises up into the atmosphere to a certain altitude and then spreads around. This causes a pressure drop around this region, which attracts the cooler air from the poles to the equator. Thus, the wind is generated due to the pressure gradient resulting from the uneven heating of earth's surface by the sun. As the very driving force causing this movement is derived from the sun, wind energy is basically an indirect form of solar energy. One or two per cent of the total solar radiation reaching the earth's surface is converted to wind energy in this way[11].

The wind described above, which is driven by the temperature difference, is called the geostrophic wind, or more commonly the global wind. Global winds, which are not affected by the earth surface, are found at higher altitudes. The rotation of earth leads to another phenomenon near its surface called the Coriolis Effect, named after the famous mathematician Gustave Paspard Coriolis. Due to the Coriolis Effect, the straight movement of air mass from the high pressure region to the low pressure region is diverted as shown in Figure 2.5. Under the influence of Coriolis forces, the air move almost parallel to the isobars. Thus, in the northern hemisphere, wind tends to rotate

clockwise where as in the southern hemisphere the motion is in the anticlockwise direction[11].

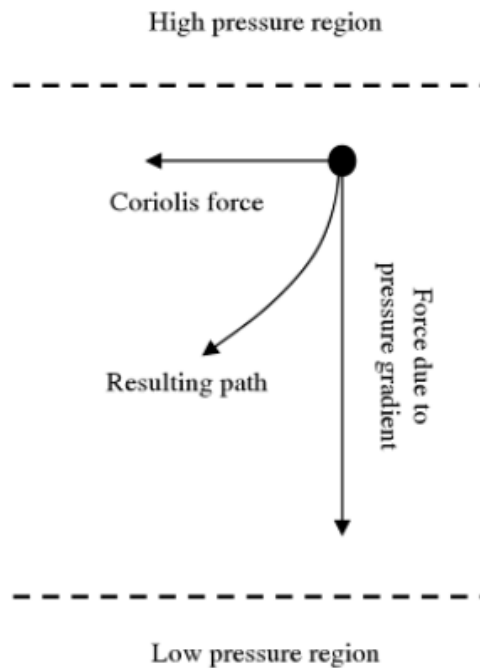


Figure 2.5 : Wind direction affected by the coriolis force[11].

2.1.1 The local effects

Changes in velocity and direction of wind near the surface, say up to 100 m above the ground, is more important as far as energy conversion is concerned. In this region, the wind pattern is further influenced by several local factors.

Land and sea breezes are examples for the local wind effects. During the day time, land gets heated faster than the sea surface. As a result, the air near the land rises, forming a low pressure region. This attracts cool air to the land from the sea. This is called the sea breeze. During night time, the process gets reversed as cooling is faster on the land. Thus wind blows from the land to the sea, which is called the land breeze.

In mountain valleys, the air above the surface gets heated and rises up along the slopes during the day time. This is replaced by the cool air, resulting in the valley winds. During the night, the flow is from the mountain to the valley which is known as the mountain wind. Quite often, this phenomenon may create very strong air currents,

developing powerful wind. Wind shear, turbulence and acceleration over the ridges are some other examples for local wind effects[11].

2.1.2 Wind shear

The flow of air above the ground is retarded by frictional resistance offered by the earth surface (boundary layer effect). This resistance may be caused by the roughness of the ground itself or due to vegetations, buildings and other structures present over the ground. For example, a typical vertical wind profile at a site is shown in Figure 2.6. Theoretically, the velocity of wind right over the ground surface should be zero [11].

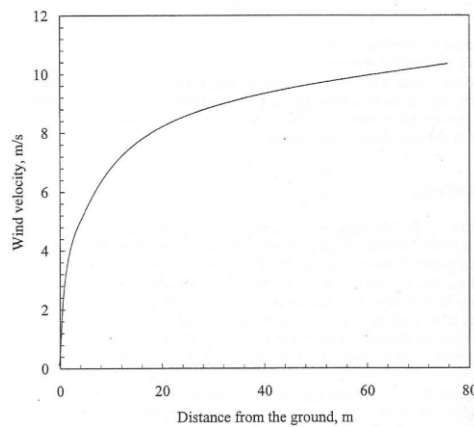


Figure 2.6: Variation of wind velocity with height[11].

This phenomenon, called wind shear, is more appreciable as height decreases and has important effects on wind turbine operation. Different mathematical models have been proposed to describe wind shear[1]. One of them is the Prandtl logarithmic law (2.1):

$$\frac{V_m(z)}{V_m(z_{ref})} = \frac{\ln(z/z_0)}{\ln(z_{ref}/z_0)} \quad (2.1)$$

where z is the height above ground level, z_{ref} is the reference height (usually 10 m) and z_0 is the roughness height [12]. Typical values of this parameter for different types

of terrain are listed in Table 2.1. Another empirical formula often used to describe the effect of the terrain on the wind speed gradient is the following exponential law (2.2):

$$V_m(z) = V_m(z_{ref}) \left(\frac{z}{z_{ref}} \right)^\alpha \quad (2.2)$$

where the surface roughness exponent α is also a terrain-dependent parameter[12]. Values of α for different types of surface are presented in the last column of Table 2.1.

Table 2.1: Typical values of roughness length z_0 and roughness exponent α for different types of surfaces[12].

Type of Surface	$z_0(\text{mm})$	α
Sand	0.2 to 0.3	0.10
Mown grass	1 to 10	0.13
High grass	40 to 100	0.19
Suburb	1000 to 2000	0.32

2.1.3 Turbulence

By definition, turbulence includes all wind speed fluctuations with frequencies above the spectral gap . Therefore, it contains all components in the range from seconds to minutes [12]. The speed and direction of wind change rapidly while it passes through rough surfaces and obstructions like buildings, trees and rocks. This is due to the turbulence generated in the flow [11]. Extent of this turbulence at the upstream and downstream is shown in Figure 2.7. In general, turbulence has a minor incidence on

the annual energy capture. However, it has a major impact on aerodynamic loads and power quality [11].

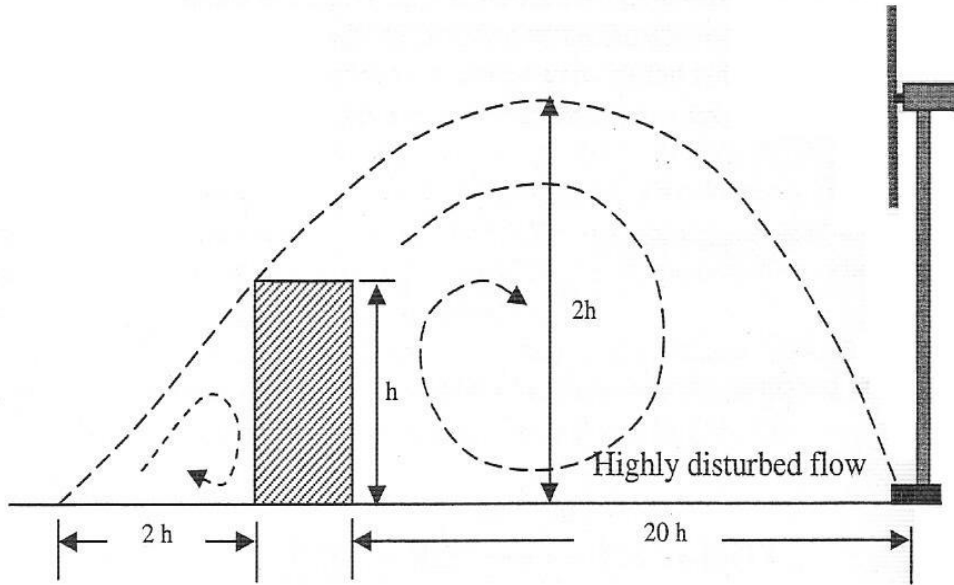


Figure 2.7 : Variation of wind velocity with height[11].

Wind turbulence at a given point in space is stochastically described by means of its power spectrum. Two widely accepted models are the Von Karman spectrum (2.3):

$$\varphi(w) = \frac{K_v}{(1+(wT_v)^2)^{5/6}} \quad (2.3)$$

and the Kaimal spectrum (2.4):

$$\varphi(w) = \frac{K_v}{(1+wT_v)^{5/3}} \quad (2.4)$$

Both models are parameterized by constants T_v and K_v . Constant T_v determines the frequency bandwidth of the turbulence whereas K_v is associated to the turbulence power. In the time domain T_v is also a measure of the correlation time of the turbulence. Both parameters depend on the mean wind speed as well as on the topography of the terrain. For instance, in the case of the Von Karman spectrum, these coefficients [(2.5) & (2.6)] are approximated by:

$$K_v = 0.475\sigma_v^2 \frac{L_v}{V_m(z)} \quad (2.5)$$

$$T_v = \frac{L_v}{V_m(z)} \quad (2.6)$$

where L_v is the correlation length of the turbulence and K_v is the turbulence intensity defined as the ratio of turbulence power(2.7):

$$\sigma_V = \sqrt{\int_{-\infty}^{\infty} \varphi(w) dw} \quad (2.7)$$

to mean wind speed(2.8):

$$\sigma_V \cong \frac{\sigma_V}{V_m(z)} \cong \frac{1}{\ln(z/z_0)} \quad (2.8)$$

Both L_v and σ_v are specific to the terrain and are experimentally obtained from wind measures. The correlation length generally takes values ranging from 100 m to 300 whereas the turbulence intensity takes values between 0.1 and 0.2[12].

Equation (2.8) shows that turbulence intensity decreases with height. It also turns out that turbulence intensity is higher when there are obstacles in the surroundings[12]. Intensity of the turbulence depends on the size and shape of the obstruction. Based on its nature, the turbulent zone can extend up to 2 times the height of the obstacle in the upwind side and 10 to 20 times in the downwind side. Its influence in the vertical direction may be prominent to 2 to 3 times the obstacle height. Hence before citing the turbine, the obstacles present in the nearby area should be taken into account. The tower should be tall enough to overcome the influence of the turbulence[11].

2.1.4 Acceleration effect

A smooth ridge, as shown in Figure 2.8, accelerates the wind stream passing over it. The acceleration is caused by the squeezing of wind layers over the mount. The degree of acceleration depends on the shape of the ridge. This effect can be fully exploited for energy generation, if the slope of the ridge is between 6° and 16° . Angles greater than 27° and less than 3° are not favorable [12].

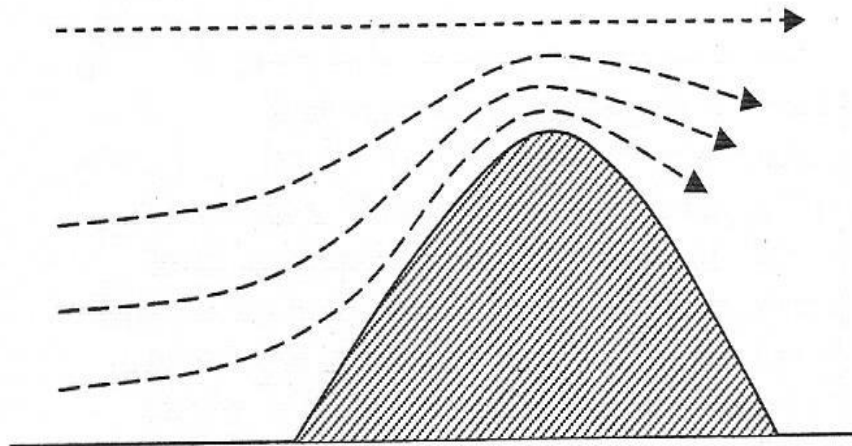


Figure 2.8 : The acceleration effect over ridges[12].

Another important factor is the orientation of the ridge. The acceleration effect is high when the prevailing wind is perpendicular and low when it is parallel to the ridge line. Similarly, if the ridge concave side facing the wind, the effect is more desirable. Triangular shaped ridges offer better acceleration followed by the smooth and round geometry. Flat topped ridges may pose the problem of turbulence, especially in the lower region[12].

Mountain passes are another geographical feature causing acceleration of wind. While the flow passes through the notches in the mountain barriers, due the ventury effect, the wind velocity is enhanced. Geometrical configuration (Width, length, slope etc.) of the pass itself is the major factor determining the degree of this acceleration. A pass between two high hills, oriented parallel to the wind direction, would be a cleverly chosen site for wind turbines. The smoother the surface, the higher will be the acceleration[12].

2.1.5 Time variation

Velocity and direction of wind change rapidly with time. In tune with these changes, the power and energy available from the wind also vary. The variations may be short time fluctuation, day-night variation or the seasonal variation.

An example for the short time variation of wind speed is shown in Figure 2.9 (A), where the velocity is recorded for 30 s. Here the velocity fluctuates between 5.1 m/s to 7.2 m/s within this time. This short-spanned change in wind speed is primarily due to the local geographic and weather effects. Stronger wind may be experienced during the day time rather than in night hours. This is termed as the diurnal variation. An example is illustrated in Figure 2.9 (B). The major reason for the velocity variation here is the difference in temperature between sea and land surface. It should be noted that the diurnal variation can be advantageous for wind energy generation as we may need more power during the day hours than at night.

Wind speed at a location may also change form season to season as shown in Figure 2.9 (C). In this case, the period between July to October is more or less lean for wind energy conversion. The root cause for seasonal variation is changes in daylight during the year due to the earth's tilt and elliptical orbit. This effect is more prominent near the poles. Knowledge of these time variations of velocity at a potential wind site is essential to ensure that the availability of power matches with the demand[11].

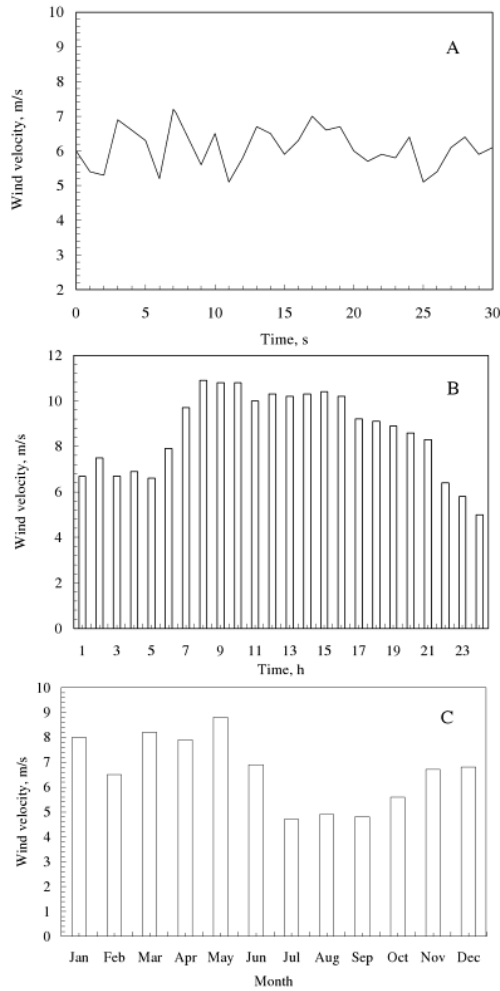


Figure 2.9 : Time variation of wind velocity[11].

2.2 Wind Turbines Technology

2.2.1 Components of a wind turbine

Wind turbines consist of four large main components: a foundation unit, a tower, a nacelle (turbine housing) and a rotor. The following section provides a brief explanation of the various parts of modern horizontal axis wind systems. They are the most widely used and this chapter will focus on them.

The forthcoming Figure 2.10 shows the diagram of a wind turbine where the different parts are indicated.

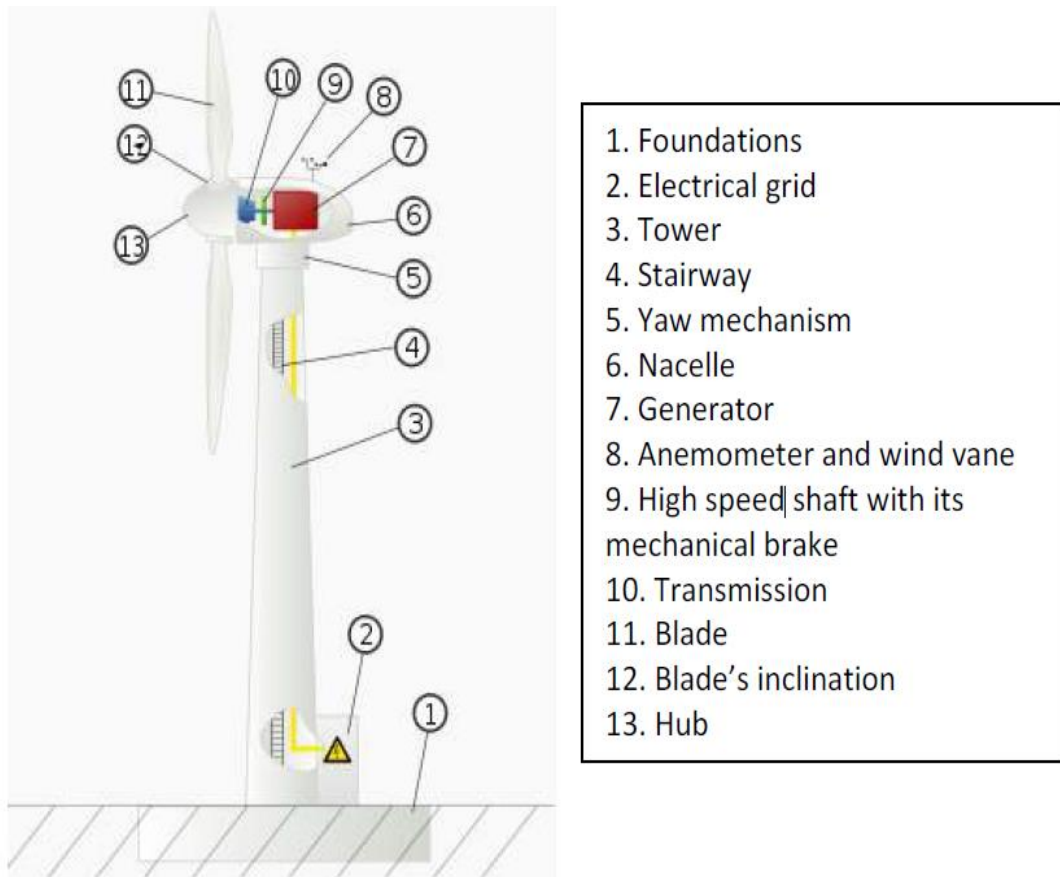


Figure 2.10: Diagram of a wind turbine[13].

The nacelle contains the key components of the wind turbine, including the gearbox and the electric generator. The hub is at the junction of the blades with the rotation system. The hub and blade assembly is called wind rotor. The gearbox is responsible for converting the low speed of the blades' rotation. The electrical generator is actually an alternator which is coupled to the gearbox through the small shaft. It has the charge of producing electricity, which is conveyed through the interior of the tower to the transformer. The anemometer measures wind speed, and sends this information to the controller, which logs it and acts accordingly on the brake. Low speed shaft attaches the gearbox with the rotor. The braking system is used to block the rotor when the maintenance is being carried out or the system must be repaired. The radiator is used to refrigerate the generator. In some wind turbines, the generator is cooled by water. The wind vane informs the control system of the wind direction at any time. The electronic controller is a computer that continuously monitors the conditions of the turbine and controls the yaw mechanism. Orients the nacelle into the wind and allows the rotor to start when the wind vane indicates that there is enough wind.

The blades are the components which interact with the wind. Their shape is designed in order to obtain good aerodynamic efficiency. The next Figure 2.11 shows a typical wind turbine blade outline, together with several cross-sections at different locations along the length[13].

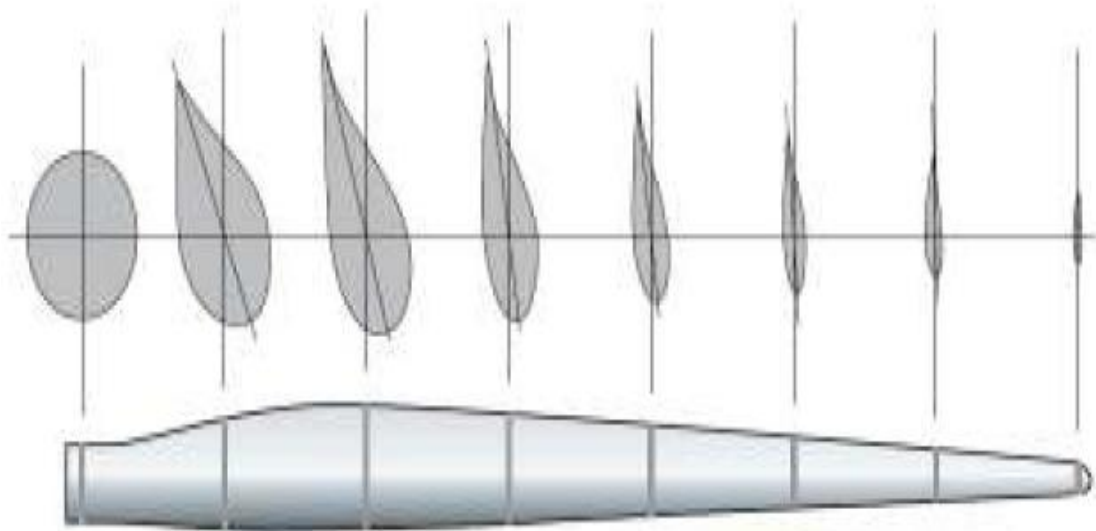


Figure 2.11: Blade shape and cross sections[13].

The aerodynamic forces vary with the square of the local relative air velocity and increase rapidly with the radius. It is thus important to design the part of the blade near the tip with good lift and low drag coefficients. The tower of the wind turbine carries the nacelle and the rotor[13].

2.2.2 Classification of wind turbines

Nowadays, there is a wide variety of wind turbine models, different from each other, both for the power provided as from the number of blades or even how they produce electricity. They can be classified, therefore, by different criteria:

I. By the position of the turbine.

a) Vertical axis: It seems in Figure 2.12 that its main feature is that the rotation axis is perpendicular to the ground. They are also called VAWTs (vertical axis wind turbines). The main advantage of this kind of turbine is the absence of a yaw system. This kind of turbine is less efficient than the horizontal-axis type but its simplification is of interest for small units used in harsh zones like high mountains or the Arctic. The rotor can have high solidity and therefore strong mechanical resistance.



Figure 2.12: Vertical wind turbine[13].

b) Horizontal axis:

They are the most common and are also called HAWTs (horizontal axis wind turbines). It can be seen an example of HAWTs in Figure 2.13. All grid-connected commercial wind turbines today are built with a propeller-type rotor on a horizontal axis. Therefore, this type of wind turbines will be studied in this thesis. The purpose of the rotor is to convert the linear motion of the wind into rotational energy that can be used to drive a generator.



Figure 2.13: Horizontal wind turbine[13].

II. By the number of blades.

a) One blade: Wind turbines with one blade are not very widespread commercially. They have the advantage of saving the cost of two rotor blades and its weight. This obviously negates the savings on weight. In addition, they need a higher rotational speed and have the noise and visual intrusion impact.

b) Two blades: Rotors equipped with two blades must rotate faster than those with three blades and as a consequence, the aerodynamic noise level is higher. A two-bladed rotor is subject to severe imbalance due to wind speed variation with height and to gyroscopic effects when the nacelle is yawed. Because of these disadvantages, they tend to have a difficulty in penetrating the market.

c) Three blades: Most modern wind turbines are three-bladed designs with the rotor position maintained upwind using electrical motors in their yaw mechanism. This design is usually called the classical Danish concept, and tends to be a standard against which other concepts are evaluated.

d) Multi-bladed turbines: The rotation speed decreases when the number of blades is increased, but the torque is raised. In low wind areas, these turbines are frequently used in agriculture to drive water pumps[13].

2.2.3 Historical development of the wind turbines

Wind energy had been utilized for about 3000 years, starting with invention of windmills, which are machines that convert wind energy to mechanical energy for milling and water pumping purposes. First examples of vertical axis windmills are found in China and Afghan-Persian regions [13]. The first horizontal axis windmills were invented in Europe and they were developed, especially in Holland region. An example of an advanced Dutch type windmill can be seen in Figure 2.14.



Figure 2.14: Windmill (Dutch ground windmill) with spring sails [13].

There are important milestones in the evolution of windmills from simple mechanical power producing machines to modern electricity producing wind turbines. First step was the attempt to modify windmills to generate electricity, which was achieved by Poul La Cour [13], a Danish professor. Industrialization of successful trials of first “wind turbines” was accelerated due to increased price of oil during World War I and they were used for electrification of rural areas even after World War II [13]. Another

milestone, achieved by the German scientist Albert Betz in 1920, was the theoretical proof that the maximum possible potential energy in the wind is limited. Moreover, his works on aerodynamic shaping of rotor blades are important sources of development for modern wind turbines. Although many experimental wind turbines are constructed and tested in different sizes, they could not be industrialized since their prices were not low enough to compete with the very low fossil fuel prices. So a successful attempt could not be achieved until the “Energy Crisis” in 1973.

Development of modern wind turbines accelerated after the establishment of various scientific institutions on wind energy in different countries to reduce the dependence on the fossil fuels[13].

Today, three bladed, upwind wind turbines dominate the market for grid connected applications. Three bladed configurations are popular mainly due to easy handling of rotor moment inertia and aesthetic aspects [14]. Moreover since it is not an efficient way to use wind turbines as isolated units, wind farms are constructed to maximize the power production from a selected wind site.

2.2.4 Offshore wind turbines

The use of wind power in the open sea offers numerous opportunities, in order to achieve ambitious climatic and energy political objectives. Offshore projects are therefore considered to be the important future market for wind power. The wind speeds at sea are higher and more constant than those on land. This is due to the fact that the sea has a limited surface roughness and obstacles to the wind are few. Another advantage of offshore is that the period of useful work of a wind turbine increases as the wind is usually less turbulent. The low turbulence at sea is primarily due to the fact that temperature variations between different altitudes in the atmosphere above the sea are smaller than above land. Sunlight will penetrate several metres below the sea surface, whereas on land the radiation from the sun only heats the uppermost layer of the soil, which thus becomes much warmer. Consequently the temperature difference between the surface and the air will be smaller above sea than above land[15].

On the other hand, the planning of wind farms offshore is a great technical challenge: the wind turbines must be designed for use in the open sea and the foundations must be adapted to cope with great depths and waves. Last but not least, the long cable

connection must also be laid at the bottom of the ocean. Figure 2.15 illustrates an example of offshore wind farm. [15].



Figure 2.15: Offshore wind turbines [15].

2.2.5 Advantages and disadvantages

Offshore locations have several advantages over land-based locations for the wind farms siting.

Aesthetics: Offshore wind turbines are obviously coming into much less human contact than those on land. Thus, people do not need to deal with the noise pollution and eye sore that turbine cause for some. Farmers have complained that the whirring noise of turbines scare their livestock, while others simply do not like the sight of the turbines. Thus, with a move off land, the sounds and images of the turbines are nearly unnoticeable.

From the environmental point of view, when constructing offshore wind farms constructors have to make sure to minimize any disturbancy to the nearby marine ecosystems. The constructors also must be careful not to build offshore wind farms in areas where they would interfere with shipping lanes, or in fishing areas.

Less Harm to Birds: Approximately 40,000 birds each year die by flying into wind turbines on land in the United States. Though this number is relatively very small in comparison to the number of deaths associated with pesticides, power lines, and other

man-made structures, it is still an unacceptable statistic. Fortunately, offshore wind turbines mitigate this danger. In an attempt to cut down on bird deaths, offshore wind farms are located in specific areas of the ocean where birds do not frequently fly.

More Wind: One of the greatest advantages that offshore wind farms have over those on land is the frequency of strong winds over the ocean. Studies have shown that winds offshore blow nearly 40 percent more often than on land. Consequently, offshore wind farms can outpace those on land in terms of capacity and possibly offset the higher construction costs[15].

Transportation: Another advantage that offshore wind energy projects have over wind energy projects on land is transport. The transport of big wind turbine components such as tower sections, nacelles, and blades is significantly easier with ships as they can handle large cargo more easily than trucks or trains, and there is no traffic jam on sea like there is on land.

More Efficient Energy Transmission: Since winds increase rapidly with distance from the coast, excellent wind sites exist within reasonable distances from major urban areas, reducing the onshore concern of long distance power transmission.

The main disadvantage of offshore wind energy farms are high construction costs. Offshore wind energy projects need to be powerfully built in order to withstand rough weather conditions. Offshore wind turbines must be fixed on the seabed, which demand a more solid supporting structure. Submarine cables are needed for transmission of electricity and special vessels and equipments are required for building and maintenance work.

The combination of all three makes a significant reason for people to maintain the development of onshore wind farms in places where there is an economic (i.e. enough wind), aesthetic and environmental sense, and to intensify their support for offshore wind[15].

2.2.6 Offshore wind technology development

Offshore wind energy has a promising future, especially in countries with a high population density which reduces the chances of finding suitable sites onshore. At sea, the wind finds variable surface roughness, such as waves, and no obstacles apart from islands. This implies that the wind speed does not experience major changes. Thus, high towers as in onshore are not necessary, reducing materials and therefore costs. In

addition to this, wind is generally less turbulent than on land, extending thereby the period of useful work of a wind turbine. Moreover, the turbulence of the sea floor is lower due to the fact that temperature differences at different altitudes of the atmosphere are lower when they occur over the sea than onshore.

There are also negative aspects, such as the current inability to build wind farms in areas of great depths and certain structural changes are required in the electricity network. Finally, a great funding is needed to build a wind farm.

In spite of the drawbacks of this technology, it is predicted a decreasing of costs and therefore an expansion of this green mode of energy production is expected.

Why offshore wind energy?

- Lack of suitable wind turbine sites on land :

One of the primary reasons for moving wind farm development offshore is the lack of suitable wind turbine sites on land. This is particularly the case in densely populated countries like Denmark or the Netherlands with a relatively flat landscape.

- Higher wind speeds:

Equally important, however, is the fact that wind speeds are often significantly higher offshore than onshore. An increase of about 20% at some distance from the shore is not uncommon. Given the fact that the energy content of the wind increases with the cube (the third power) of the wind speed, the energy yield may be about 73% higher than on land. Economically optimized turbines, however, will probably yield about 50% more energy at sea than at nearby land locations.

- More stable winds:

It is a frequent misunderstanding that wind power generation requires very stable winds. In fact, in most wind turbine sites around the globe, the wind varies substantially, with high winds occurring rather infrequently, and low winds occurring most of the time. If we look at the typical statistical wind distribution, most of the energy output is in fact produced at wind speeds close to twice the average wind speed at the site.

- Huge offshore wind resources:

Offshore wind resources are enormous: Wind energy resources in the European Union seas with water depths up to 50 metres are easily several times larger than the total European electricity consumption. The offshore wind resource is obviously somewhat unevenly distributed among countries. In the case of Denmark, offshore wind energy may theoretically supply more than ten times national electricity consumption, due to large areas with shallow waters (5 to 15 m depth).

- Lower turbulence: longer lifetime:

The temperature difference between the sea surface and the air above it is far smaller than the corresponding difference on land, particularly during the daytime. This means that the wind is less turbulent at sea than over land. This, in turn, will mean lower mechanical fatigue load and thus longer lifetime for turbines located at sea rather than land[15].

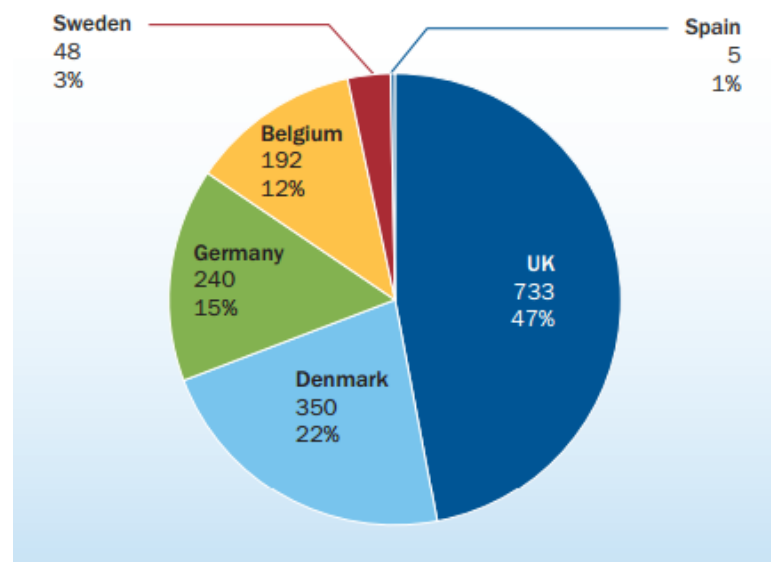


Figure 2.16 : Share of annual offshore wind capacity installations per country (MW) (2013)[16,17].

Figure 2.16 represents that 1,567 MW of new offshore wind power capacity were connected to the electricity grid during 2013 in Europe: 34% more capacity than the previous year. 47% of all new capacity was installed in the UK (733 MW). The share of total capacity installed in the UK was significantly less than in 2012 (73%). The second largest amount of installations were in Denmark (350 MW or 22%), followed by Germany (240 MW, 15%) and Belgium (192 MW, 12%)[17]. The consented capacity per country in 2014 is indicated in Figure 2.17.

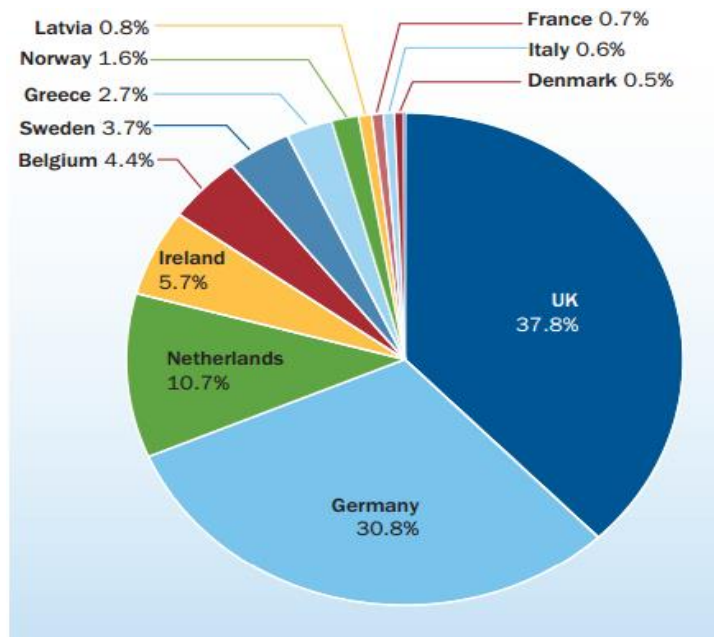


Figure 2.17 : Share of consented offshore capacity per country (MW) (2014) [16,17].

As Table 2.2 displays that 418 new offshore wind turbines, in 13 wind farms, were fully grid connected between 1 January and 31 December 2013, totalling 1,567 MW, 34% more than in 2012.

Table 2.2 : Number of turbines and MW fully connected to the grid during 2013 per country (2013)[16,17].

Country	Belgium	UK	Germany	Denmark	Sweden	Spain	TOTAL
No. of Farms	3	8	8	1	1	1	22
No. of Turbines Connected	44	212	48	97	16	1	418
MW connected to Grid	192	733	240	350	48	5	1567

When looking at wind farms currently under construction per sea basin, it is clear that the North Sea will continue to be the main region for offshore deployment (84.8% of total capacity under construction). It is clear in Figure 2.18 that the Baltic Sea (10%) and the Atlantic Ocean (5.1%) will, however, continue to attract important developments. No significant developments are expected in the Mediterranean Sea in the short term[16,17].

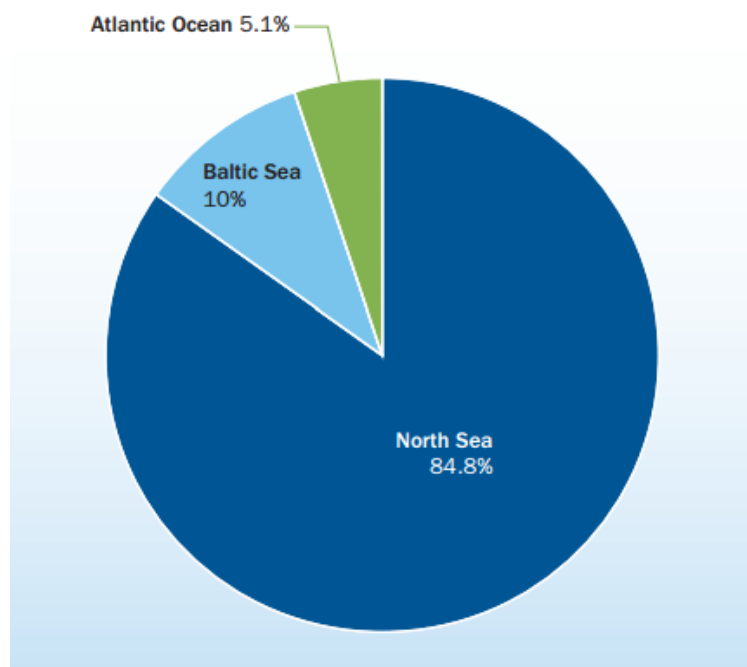


Figure 2.18: Share of offshore wind farms under construction by sea basin(MW) [16].

The Path to Deeper Water

The offshore wind industry is likely to develop along the path illustrated in Figure 2.19.

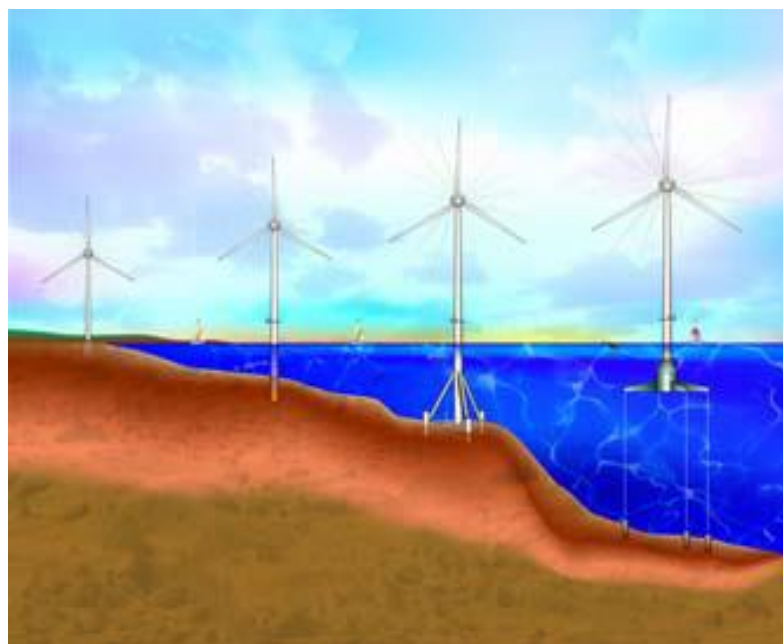


Figure 2.19: Technology progression for offshore wind turbines[18].

Preliminary mesoscale weather model assessments of the offshore wind indicate a sharp increase in wind speed with distance to shore. Siting options also improve with distance from shore, as there are more viable high wind sites with less visual impacts and competing uses for the seabed. These matters primarily, will gradually attract developers to deeper waters.

This progression to deeper water will make its way from experience gained from more sheltered projects in shallow water, similar to the petroleum industry’s march into deep water during the twentieth century. As a result, much of the technology to do this has already been developed by the existing oil and gas industry, and a concerted effort to transfer that technology is already underway in the wind industry today. However, new technology is still needed to make wind energy economically competitive over a broad range of deeper water sites[18].

Offshore Substructures

The most critical aspect in the development and expansion of offshore wind energy lies with the substructures. As water depth increases, it is likely that the cost of offshore foundations will increase due to the added complexity and resources needed below the waterline. One of the goals of a new USDOE research and development program is to develop new substructure technologies and make them commercially available as the current designs reach their depth limits, and thereby minimize the water depth cost penalty. Figure 2.20 gives a conceptual view of how these technologies may evolve.

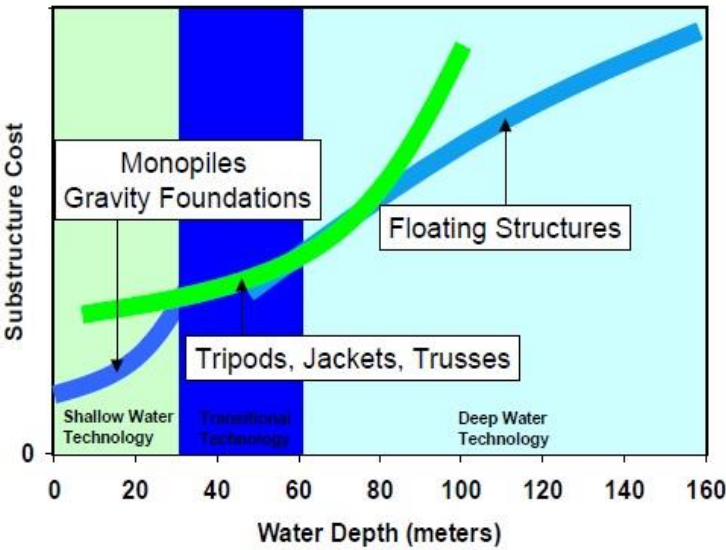


Figure 2.20 : Cost of offshore wind turbine substructures with water depth[12].

Tripods, jackets, and truss-type towers will replace monopiles and gravity bases, initially using conventional oil and gas offshore practices, but later implementing new strategies that can take advantage of the lower environmental and safety risks, and higher production volume associated with offshore wind turbines. At some depth, fixed bottom foundations will be replaced by floating systems that have a high potential for site independence, mass production, and wide-ranging wind turbine innovation.

Floating Technology

At some water depth, a floating substructure may be the best option. A floating structure must provide enough buoyancy to support the weight of the turbine and to restrain pitch, roll, and heave motions within acceptable limits. A primary difference between the load characteristics of a floating wind turbine and a floating oilrig is that, for a wind turbine, large wind-driven overturning moments dominate the design while an oilrig's design is payload and wave driven. System-wide interactions such as coupled turbine/platform dynamics could potentially impose additional inertial loading requiring more dynamically tolerant turbines. Any added complexities must be offset by higher offshore winds, and greater public acceptance due to lower visual and environmental impacts.

No full-scale floating systems have been deployed yet but some private groups in Norway claim to be working on full-scale prototypes[12].

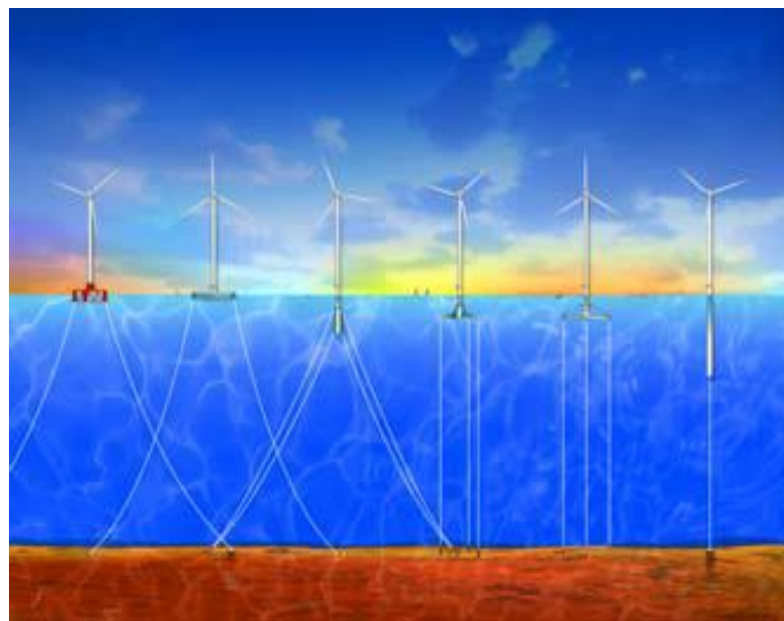


Figure 2.21: Floating deepwater platform concepts[12].

Figure 2.21 shows a wide range of platform architectures that are being considered for floating offshore platforms. Platform types are labeled numerically in the figure (from left to right): 1) semi-submersible Dutch Tri-floater , 2) barge, 3) spar-buoy with two tiers of guy-wires [3], 4) three-arm mono-hull tension leg platform (TLP), 5) concrete TLP with gravity anchor, and 6) deep water spar[12].

Some preliminary studies have been done already to assess floating systems but none of the public studies to date have attempted to optimize the platform cost and geometry [19].

The wind turbine platform and mooring system should provide the most potential for system cost reduction because the application is new and the most significant cost saving design tradeoffs have not yet been explored. However, a solid basis from which to determine the optimum design has not yet been established.

Many of the same issues that govern oil and gas platforms will also be present in the design of wind platforms, but the importance of each variable will be weighted differently. There are a vast number of possible offshore wind turbine platform configuration permutations when one considers the variety of available anchors, moorings, buoyancy tanks, and ballast options in the offshore industry. Unfortunately, designers will find that most of the resulting topologies will have some undesirable aspects that could drive the system cost out of range for wind applications. The optimum platform probably does not exist due to real-world constraints, but there are many features that such a platform would embody that most designers could agree on. To narrow the range of options, a study is now underway at the National Renewable Energy Laboratory (NREL) to compare each platform design to features that an optimized platform should have. From this comparison, we can begin to determine the key issues that limit each platform type and that will direct future study in this area. Some of the variables to be assessed are identified by Butterfield et al[19] and are given below:

- ✓ Requirements for design tools and methods- controls complexity
- ✓ Buoyancy Tank Cost/Complexity/Material options
- ✓ Mooring Line System Cost/Complexity/Options

- ✓ Anchors Cost/Complexity/Options
- ✓ Load Out Cost/Complexity/Options/Requirements
- ✓ On-site installation requirements
- ✓ Decommissioning and maintainability
- ✓ Corrosion Resistance requirements – coatings, cathodic protection, etc.
- ✓ Depth Independence/ Specify depth range
- ✓ Sensitivity to Bottom Conditions / Specify limitations
- ✓ Required footprint (as a function of depth)
- ✓ System Weight Sensitivity/ CG sensitivity
- ✓ Induced Tower Top Motions - Wave Sensitivity-Allowable heel angle
- ✓ First Order Costs for Candidate Configurations

Butterfield also provided a framework for assessing various platform concepts on the basis of how a platform type achieves static stability. This approach argues that static stability and a range of associated operational and technical factors largely determine the first order economics of a floating platform. An optimization study to determine the lowest cost platform architecture will follow from these analyses[19].

Technologically, it is recognized that the commercial undertaking of floating wind turbines will be a bold step, but is necessary to unlock an additional 500-GW of offshore wind energy potential in the United States and become one of the major contributors to the world's electric grid. However, it will require substantial experience in shallower water, with parallel and substantive research and development initiatives to realize this technology over the next 15 years[20].

3. GEOMETRIC AND AERODYNAMIC CHARACTERISTICS OF AIRFOILS

3.1 Airfoil Geometry and Nomenclature

2-D airfoil section consists of the leading edge (LE), the trailing edge (TE) and the line joining the two called the chord (c). The angle-of-attack is generally measured between the velocity (or relative velocity) vector V and the chord line. (Although the angle-of-attack can be defined as the angle between the velocity vector and any fixed line in the airfoil) [21].

A line that is midway between the upper surface and lower surface is called the camber line. The maximum distance from the chord line to the camber line is designated as the airfoil camber, generally expressed as a percent of the chord line, such as 5% camber. The maximum distance between the upper and lower surface is the airfoil thickness, t_{\max} (3.1), also designate as a percent of chord length. Then we have:

$$\frac{\delta}{c} \cdot 100 = \% \text{ camber} \quad \frac{t_{\max}}{c} \cdot 100 = \% \text{ thickness} \quad (3.1)$$

As defined earlier, the lift and drag on an airfoil are defined perpendicular and parallel to the relative wind respectively. In addition, we can define the aerodynamic pitch-moment relative to some point on the airfoil (usually located on the chord), with the sign convention that a positive pitch moment is in the direction that would move the nose up. (If we recall, that the y body axis points out the right hand wing, then the moment about the y axis, using the right hand rule, would give us a nose up moment as positive).

We generally designate airfoil 2-D aerodynamic properties by lower case letters. For example the lift coefficient, 2-D is C_l as compared to CL used for the 3-D lift coefficient. With this in mind, we can define the 2-D lift, drag, and pitch moment(3.2) in the following manner:

$$C_l = \frac{L}{\frac{1}{2}\rho V^2 c (1)}$$

$$C_d = \frac{D}{\frac{1}{2}\rho V^2 c (1)} \quad f(\alpha, Re, M) \quad (3.2)$$

$$C_m = \frac{M}{\frac{1}{2}\rho V^2 c^2 (1)}$$

where $c (1)$ is the chord times the unit width that we use for area in the case of 2-D bodies. We can also note that the pitch-moment requires an additional length in the denominator to retain a non-dimensional form; here we use the chord length[21].

An airfoil is a body of such a shape that when it is placed in an airstreams, it produces an aerodynamic force. This force is used for different purposes such as the cross sections of wings, propeller blades, windmill blades, compressor and turbine blades in a jet engine, and hydrofoils are examples of airfoils. The basic geometry of an airfoil is shown in Figure 3.1.

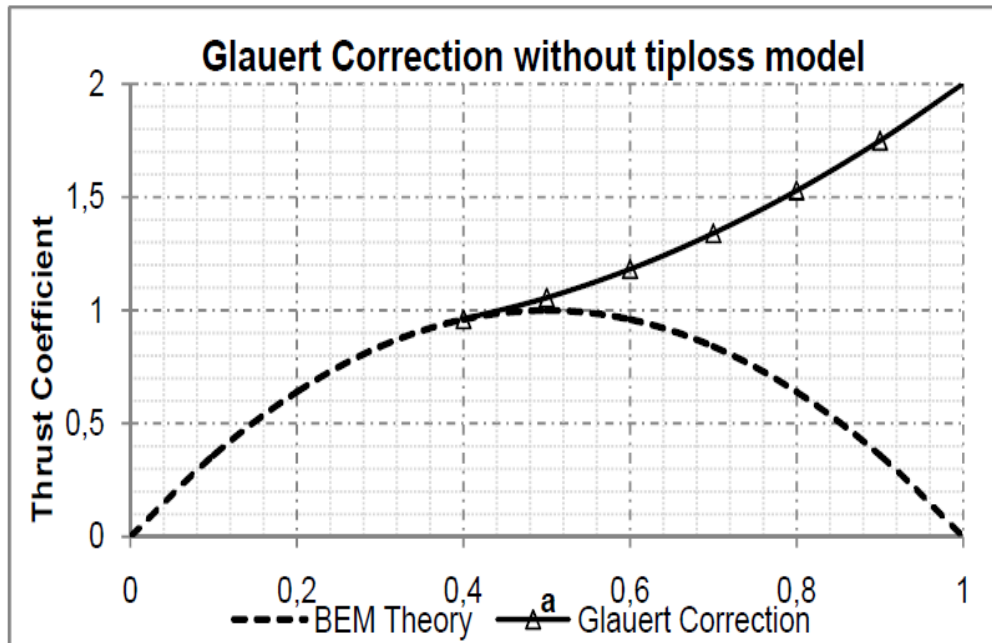


Figure 3.1 : Basic nomenclature of an airfoil[21]

The leading edge is the point at the front of the airfoil that has maximum curvature. The trailing edge is defined similarly as the point of maximum curvature at the rear of the airfoil. The chord line is a straight line connecting the leading and trailing edges of the airfoil. The chord length or simply chord is the length of the chord line and is the characteristic dimension of the airfoil section[21].

3.2 Aerodynamic Properties

3.2.1 Angle of attack

If you stretch your arm out through the window of car that is moving at a good speed, you can feel your arm pushed backward. If you hold your arm straight with your hand parallel to the road, and change the angle slightly, you can suddenly feel that it is down upwards. The hand and arm work like the wing of an airplane and with the right angle (of attack) you can feel a strong lift force [22]. AOA is the angle between the oncoming air or relative wind and a reference line on the airplane or wing. Sometimes the reference line is a line connecting the leading edge and trailing edge at some average point on a wing. Most commercial jet airplanes use the fuselage center line or longitudinal axis as the reference line. It makes no difference what the reference line is as long as it is used consistently. As the nose of the wing turns up, AOA increases, and lift increases. Drag goes up also, but not as quickly as lift as shown in Figure 3.2. During take-off an airplane builds up to a certain speed and then the pilot “rotates” the plane that is, the pilot manipulates the controls so that the nose of the plane comes up and, at some AOA, the wings generate enough lift to take the plane into the air. Since an airplane wing is fixed to the fuselage, the whole plane has to rotate to increase the wing's angle of attack. Front wings on racecars are fabricated so the angle of attack is easily adjustable to vary the amount of down force needed to balance the car for the driver[21].

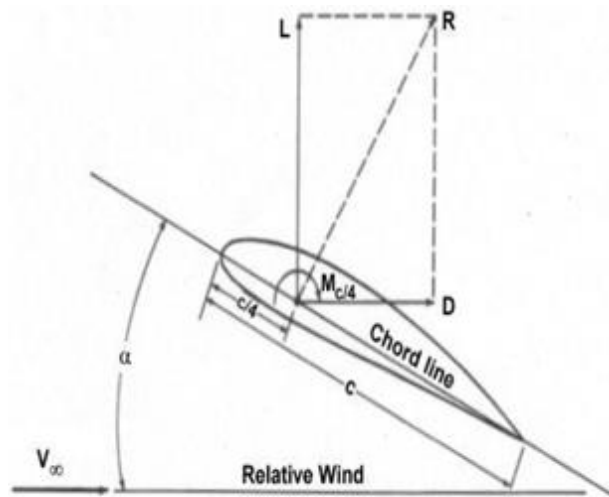


Figure 3.2: Angle of attack[21].

3.2.2. Lift characteristics

The aerodynamic properties of most interest to us for performance considerations are those associated with lift and drag. A plot of lift coefficient vs angle-of-attack is called the lift-curve. A typical lift curve appears below. We can note the following: 1) for small angles-of-attack, the lift curve is approximately a straight line. We will make that assumption and hence deal almost exclusively with “linear” aerodynamics.

2) That for some angle-of-attack called the stall angle-of-attack, the lift coefficient reaches a maximum, $C_{l_{max}}$.

3) There are two intercepts that we can designate, one the alpha axis for zero lift, designated as α_{0L} , the zero-lift angle-of-attack, and the one at zero angle-of-attack designated as C_{L_0} , the lift at zero angle-of-attack.

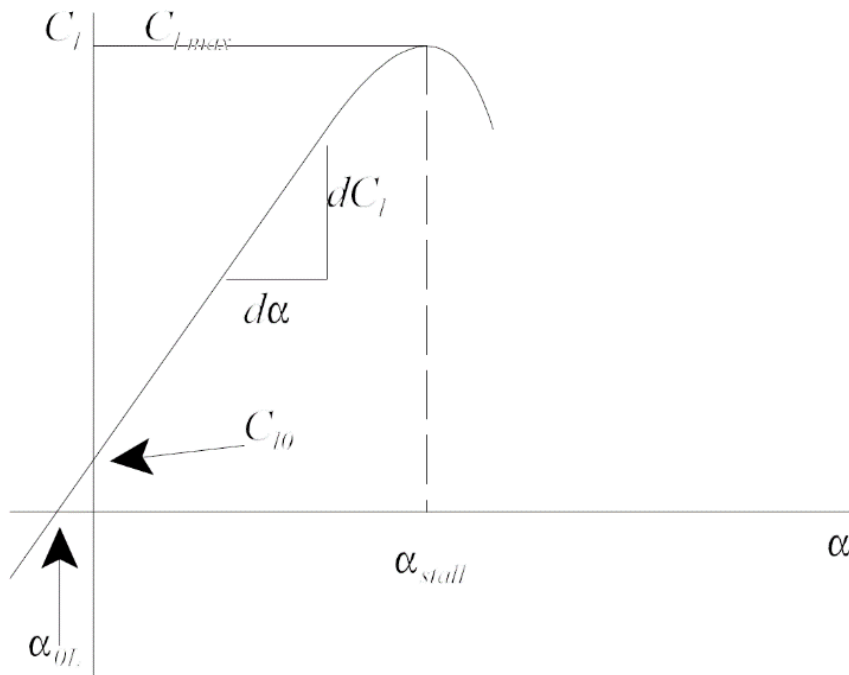


Figure 3.3 : Lift coefficient vs angle of attack[21].

With the assumption of linear aerodynamics, as it can be seen in Figure 3.3, a mathematical model of how the lift coefficient varies with angle-of-attack can be created. To simplify the resulting expressions(3.3), we can first define the 2-D lift-curve slope:

$$a_0 = \frac{d C_l}{d \alpha} \quad (3.3)$$

where the subscript “0” is used to designate that this is a 2-D lift-curve slope. With this definition, we can write our mathematical model for the lift coefficient:

2-D Lift Curve(3.4) can be defined as below:

$$\begin{aligned} C_l &= C_{l_0} + a_0 \alpha \\ &= a_0 (\alpha - \alpha_{0L}) \end{aligned} \quad (3.4)$$

where it is easily seen that $C_{l_0} = a_0 \alpha_{0L}$ or $\alpha_{0L} = -\frac{C_{l_0}}{a_0}$

Coefficient of Drag and Coefficient of Lift

The drag equation, $F_d = \frac{1}{2} \rho v^2 C_d A$ so coefficient of drag is given by the, $C_d =$

$\frac{2 F_d}{\rho v^2 A}$ is essentially a statement that the drag force on any object is proportional to

the density of the fluid and proportional to the square of the relative speed between the object and the fluid. In fluid dynamics the C_d is a dimensionless quantity that is used to quantify the drag or resistance of an object in a fluid environment such as air or water. It is used in the drag equation where a lower drag coefficient indicates the object will have less aerodynamic or drag. The drag coefficients always associated with a particular surface area. The drag coefficient of any object comprises the effects of the two basic contributors to fluid dynamics drag: skin friction and form drag. The drag coefficient of a lifting airfoil or hydrofoil also includes the effects of lift induced drag. The drag coefficient of a complete structure such as an aircraft also includes the effects of interference drag. The overall drag coefficient defined in the usual manner is The reference area depends on what type of drag coefficient is being measured. For automobiles and many other objects, the reference area is the projected frontal area of the vehicle. This may not necessarily be the cross sectional area of the vehicle, depending on where the cross section is taken and for an airfoil the surface area is a

plane form area. The lift equation, $L = \frac{1}{2} \rho v^2 A C_L$ so coefficient of lift is given by

$$\text{the, } C_L = \frac{L}{\frac{1}{2} \rho v^2 S} = \frac{2L}{\rho v^2 S} = \frac{L}{qS}$$

A fluid flowing past the surface of a body exerts a force on it. Lift is the component of this force that is perpendicular to the oncoming flow direction. It contrasts with the

drag force, which is the component of the surface force parallel to the flow direction. If the fluid is air, the force is called an aerodynamic force[21].

Relationship between Angle of Attack, Coefficient of Drag and Coefficient of Lift

Increasing angle of attack is associated with increasing lift coefficient up to the maximum lift coefficient, after which lift coefficient decreases. As the angle of attack of a fixed-wing aircraft increases, separation of the airflow from the upper surface of the wing becomes more pronounced, leading to a reduction in the rate of increase of the lift coefficient. There is a typical curve for a cambered straight wing. A symmetrical wing has zero lift at 0 degrees angle of attack. The lift curve is also influenced by wing platform. A swept wing has a lower, flatter curve with a higher critical angle. Identically the value of drag coefficient is zero at the zero AOA and it increase slowly till the stall condition and at the time of stall as well as after stall it increase readily as shown in Figure 3.4. Particular airspeed, the airspeed at which the aircraft stalls varies with the weight of the aircraft, the load factor, the center of gravity of the aircraft and other factors. However the aircraft always stalls at the same critical angle of attack. The critical or stalling angle of attack is typically around 15° for many airfoils[21].

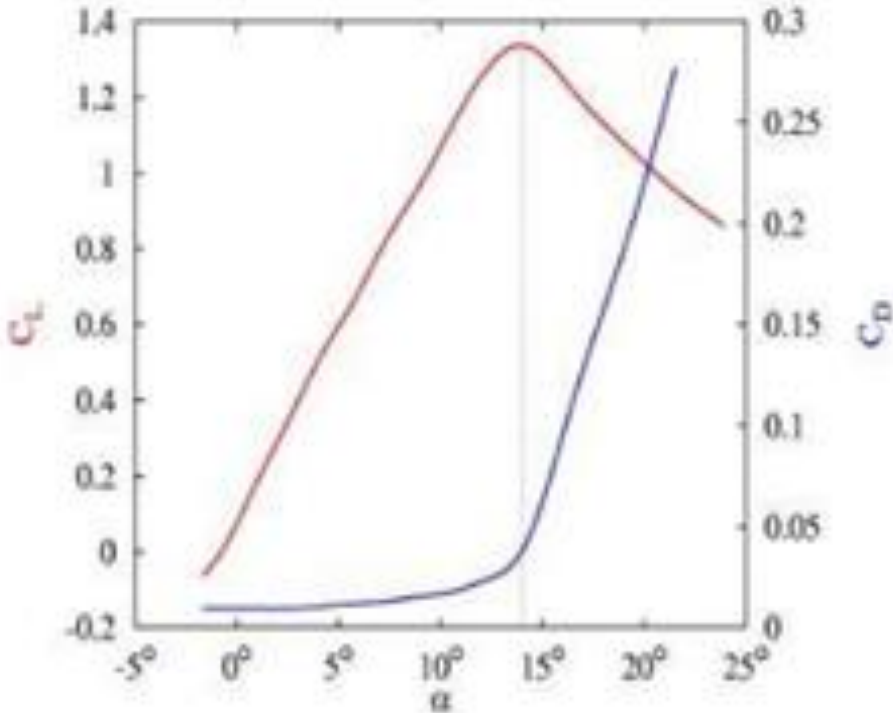


Figure 3.4 : Angle of attack, coefficient of drag and coefficient of lift[21].

3.2.3. 2-D moment

In order to calculate an aerodynamic moment for an airfoil, we need to define a reference point about which to define the moment. Typical reference points are the leading edge of the airfoil and the 1/4 chord location of the airfoil (for reasons to be determined later). The force and moment system on an airfoil is shown in the Figure 3.5:

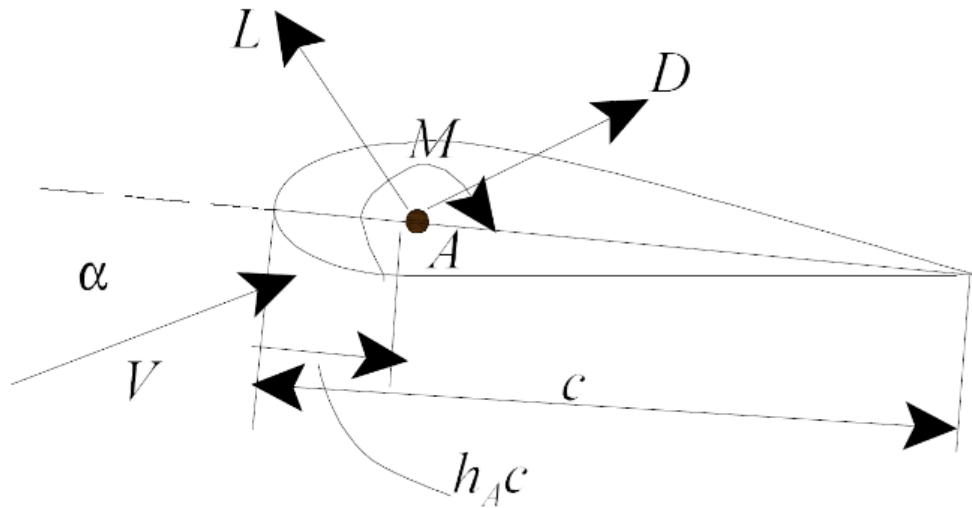


Figure 3.5 : 2-D moment[23].

The drag is parallel to the relative wind, and the lift is perpendicular to the relative wind. The aerodynamic moment is positive nose up. Here we are taking the moment about point A. Once we pick a point, we can use some theorems from statics that say that we can represent a force and moment system by assuming that the forces act through a given point and that there is a pure moment about that point.

Here we locate the reference point from the leading edge of the airfoil at a distance, $h_A c$ from the leading edge of the airfoil along the chord line. We could also select another point, B and assume the lift and drag act through that point, and that, in addition, there is a pure moment about B (different from that about A). We can arrive at an equation that allows us to transfer moments from one point to another in the following way: Consider taking moments(3.5) about the leading edge of the airfoil[23]. Then we have:

$$\begin{aligned}
 M_{LE} &= M_A - L_A \cos\alpha(h_A c) - D_A \sin\alpha(h_A c) \\
 &= M_B - L_B \cos\alpha(h_B c) - D_B \sin\alpha(h_B c)
 \end{aligned}
 \tag{3.5}$$

However the forces are the same so that $LA = LB = L$, and $DA = DB = D$. The moments (3.6) are different and are related by the above equation that we can rewrite as:

$$M_A = M_B - L(h_A - h_B)(c)\cos\alpha + D(h_A - h_B)(c)\sin\alpha \quad (3.6)$$

This equation can be simplified by making a few observations: 1) the angle α is $\ll \pi$, so that the cosine of the angle is approximately 1 and the sine of the angle equals the angle, $\cos\alpha = 1$, and $\sin\alpha = \alpha$, 2) the lift is much less than the drag, $L \ll D$. With these two assumptions, we can note that the last term in Eq. (5) is the product of two small quantities and is therefore second order compared to the first two terms, and can be neglected. With these assumptions we have the equation(3.7) that we are looking for:

$$M_A = M_B + L(h_A - h_B)c \quad (3.7)$$

If we put this in coefficient form, then we have general rule for transferring moments:

$$C_{m_A} = C_{m_B} - C_l(h_A - h_B) \quad (3.8)$$

Equation (3.8) is used for changing reference points for taking moments. Here $h(\)$ is the nondimensional location (in chord lengths) of the reference point from the leading edge of the wing.

3.2.4 Aerodynamic center

The aerodynamic center is the reference point about which the aerodynamic moment(3.9) does not change with changes in angle-of-attack:

$$\frac{dC_{m_{ac}}}{d\alpha} \equiv 0 \quad (3.9)$$

The location of the aerodynamic center[(3.10)&(3.11)] can be determined from experimental data from its definition:

$$C_{m_{ac}} = C_{m_B} - C_l(h_{ac} - h_B) \quad (3.10)$$

and

$$\frac{dC_{m_{ac}}}{d\alpha} = 0 = \frac{dC_{m_B}}{d\alpha} + \frac{dC_l}{d\alpha}(h_{ac} - h_B) \rightarrow h_{ac} = h_B - \frac{\frac{dC_{m_B}}{d\alpha}}{\frac{dC_l}{d\alpha}} \quad (3.11)$$

Since the pitch moment (coefficient) is constant at the aerodynamic center, it is evident that when the lift is zero, the pitch moment at the aerodynamic center is unchanged and is still the same. However from Eq. (3.11), it is clear that when there is zero lift, the pitch moment is the same about any point on the airfoil (since there are no forces, it is a pure couple)[23]. Consequently, we can note that:

$$C_{m_{oL}} = C_{m_{ac}} = \text{constant}.$$

3.2.5 Center of pressure

The center of pressure is defined as the location on the airfoil where the pitch moment is zero. We can determine an expression for the center of pressure from the general moment equation, Eq. (3.12):

$$C_{m_{ac}} = 0 = C_{m_B} + C_l (h_B - h_{ac}) \rightarrow h_{cp} = h_B - \frac{dC_{m_B}}{dC_l} \quad (3.12)$$

It would be convenient to make the point B the aerodynamic center so that $C_{m_B} = C_{m_{ac}} = \text{const}$ Then the center of pressure(3.13) would be :

$$h_{cp} = h_{ca} - \frac{C_{m_{ac}}}{C_l} \quad (3.13)$$

As it can be seen in Figure 3.6, note that unlike the aerodynamic center, the location of the center of pressure depends upon the lift coefficient[23].

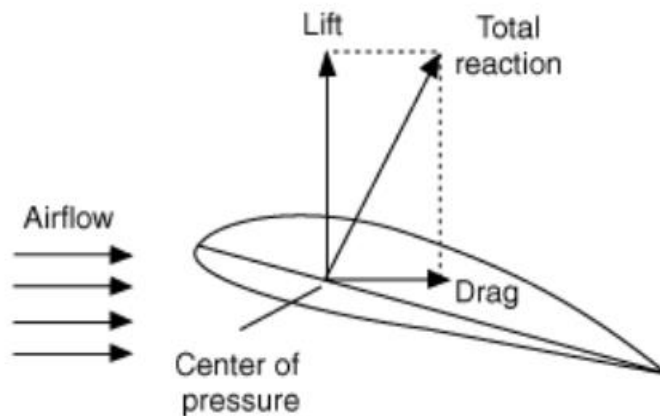


Figure 3.6 : Centre of pressure[23].

Airfoil Drag Characteristics

The drag on an airfoil (2-D wing) is primarily due to viscous effects at low speed and compressibility effects (wave drag) at high speed. In addition, at high angles of attack, the flow can separate from the upper surface and cause additional drag. Hence as indicated in our dimensional analysis, the drag coefficient depends on three quantities, Reynolds number, Mach number, and the angle-of-attack. Typically the Reynolds number is important at low speeds, the Mach number at high speeds and the angle-of-attack at all speeds. Some typical curves are shown in Figure 3.7:

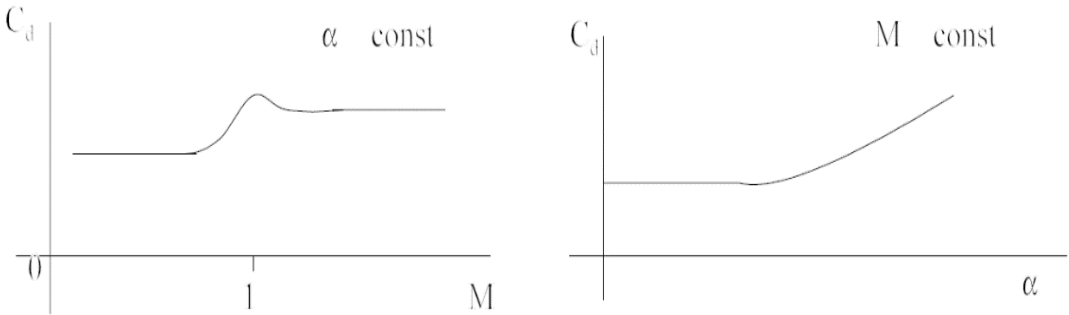


Figure 3.7 : Drag coefficient[23].

Here we see that the drag coefficient is nearly constant at subsonic speeds and tends to rise just before Mach = 1. The biggest variation is in the neighborhood of Mach 1, called the transonic region. Above that region, say about Mach 1.2, the 2-D drag coefficient tends to be constant or it could increase or decrease slightly. Figure 3.7 on the right represents a typical change of drag coefficient with angle-of-attack at a given Mach number. It tends to increase slightly with angle of-attack at low angles, and increases more rapidly at high angles-of-attack. The curve is approximately quadratic in angle-of-attack.

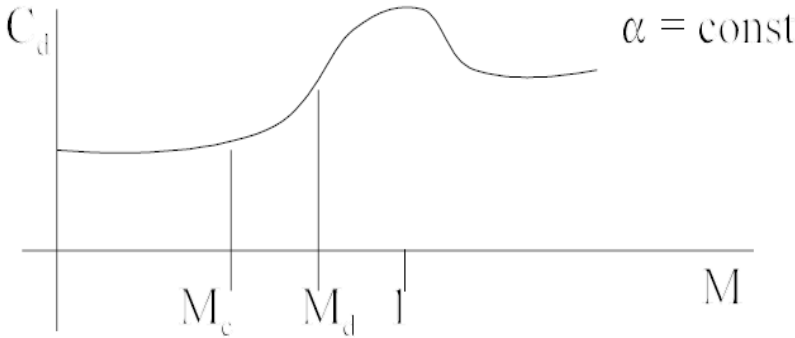


Figure 3.8 : Drag coefficient – mach numbers[23].

If we look at a close up of the drag coefficient in the transonic region in Figure 3.8, we can define certain specific Mach numbers. As the Mach number is increased, the first specific Mach number that we encounter is the critical Mach number, M_c . Definition: Critical Mach Number

The critical Mach number is defined as the Mach number at which the flow somewhere on the airfoil is sonic, $Mach = 1$.

The next Mach number encountered is called the Drag Divergence Mach Number [23].

3.3 The NACA Airfoils

The NACA (National Advisory Committee for Aeronautics) airfoils were designed during the period from 1929 through 1947 under the direction of Eastman Jacobs at the NACA's Langley Field Laboratory. Most of the airfoils were based on simple geometrical descriptions of the section shape, although the 6 and 6A series were developed using theoretical analysis and don't have simple shape definitions. Although a new generation of airfoils has emerged as a result of improved understanding of airfoil performance and the ability to design new airfoils using computer methods, the NACA airfoils are still useful in many aerodynamic design applications. A number of references have been included to allow the reader to study both the older NACA literature and the new airfoil design ideas. Taken together, this literature provides a means of obtaining a rather complete understanding of the ways in which airfoils can be shaped to obtain desired performance characteristics.

The NACA airfoils are constructed by combining a thickness envelope with a camber or mean line. The equations[(3.14)&(3.15)] which describe this procedure are:

$$x_u = x - y_t(x)\sin\theta \quad (3.14)$$

$$y_u = y_c(x) + y_t(x)\cos\theta$$

and

$$x_l = x - y_t(x)\sin\theta \quad (3.15)$$

$$y_l = y_c(x) - y_t(x)\cos\theta$$

where $y_t(x)$ is the thickness function, $y_c(x)$ is the camber line function, and

$$\theta = \tan^{-1}\left(\frac{dy_c}{dx}\right) \quad (3.16)$$

is the camber line slope(3.16). It is not unusual to neglect the camber line slope, which simplifies the equations and makes the reverse problem of extracting the thickness envelope and mean line for a given airfoil straightforward.

which gives a value of $a = \frac{1}{3}$

Hence,

This upper-bound applies for any type of wind turbine, even for vertical-axis ones though its derivation is different. The power coefficient of modern commercial wind turbines reaches values of about 0.5, well below the theoretical limit, though greater values have been reported for some particular designs. The power coefficient is usually provided by manufacturers. However, this data is not given as function of the interference factor a , but as function of the tip-speed-ratio and pitch angle that will be explained later in this thesis[24].

3.4 An Overview of NACA 6-digit airfoil series

In the beginning of the revival of wind energy as an energy source in the seventies of the last century, NACA airfoils were adopted for wind turbine blades as a result of the availability of two-dimensional aerodynamic characteristics, even for airfoils with a fairly large relative thickness. The NACA four and five-digit series were later on abandoned for their sensitivity to roughness, but airfoils from the NACA 63 and 64 six-digit series are still being used in wind turbine blades today.

Since the seventies special wind turbine dedicated airfoil designs have found their way to blade and turbine manufacturers. Many of these designs were experimentally verified in wind tunnels up to Reynolds numbers of 3 to 4 million. With the present trend towards very large turbines the Reynolds numbers have grown to about 10 million. Testing at these high Reynolds numbers is very expensive since this requires a large atmospheric tunnel, a pressure tunnel or a cryogenic tunnel. For all three types of facilities a fairly expensive model is needed as well. This leads to the situation that little experimental data is available for existing wind turbine dedicated airfoils at Reynolds numbers higher than 4 million. Blade designers now have to rely on the predictive value of airfoil analysis codes such as XFOIL or Navier-Stokes solvers. Since the NACA airfoils we are discussing here were tested at Reynolds numbers up to 9 million these data can be used to verify the accuracy of the prediction codes and

even a renewed interest for these airfoils may be noticed among wind turbine blade manufacturers.

The design and testing of the NACA airfoils some 70 years ago was a tremendous effort and rendered valuable information to many aerodynamicists world wide. However, when using it for verification, we have to take a closer look at the various test results. It appears that some anomalies in the data can be detected, which invites us to critically investigate all the relevant data[24]. The blade geometry in two dimensional, which is used in our analyses, is in Figure 3.9.

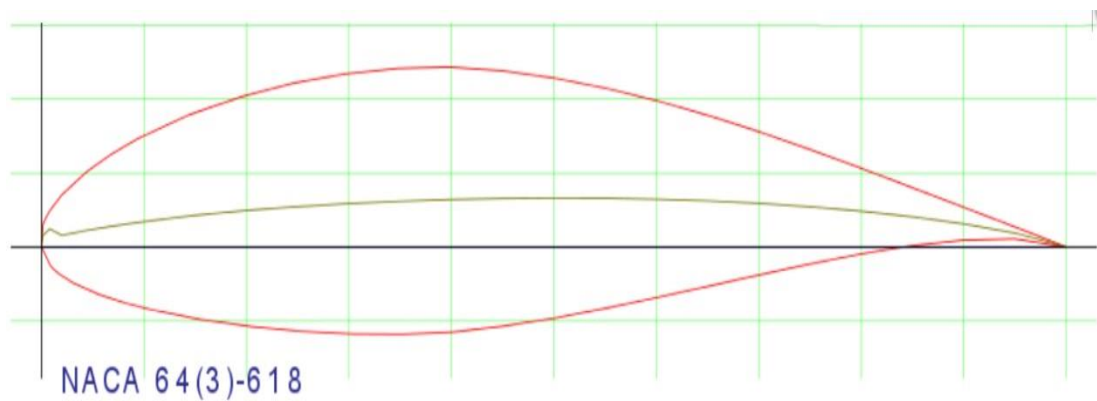


Figure 3.9 : NACA 64(3)618 profile[24].

4. THEORETICAL BACKGROUND

4.1 Underlying Method For *panMARE*

The panel code *panMARE* (panel Code for Maritime Applications and Research) is a command driven program aimed to simulate arbitrary potential flows in marine applications. The program is based on a three-dimensional first-order panel method where the geometry of the considered body is discretised into flat quadrilateral elements. On the discretised body adequate boundary conditions are applied and a linear system of equations is solved to obtain a local velocity and pressures distribution on the body.

PanMARE is based on panel method, which is able to calculate steady and unsteady flows on the basis of potential theory. In this work, it is used exclusively to determine the properties of air flow around an airfoil. The program is developed at the Technical University of Hamburg for various shipbuilding applications.

4.1.1 Boundary element method

The method used here for the evaluation of the airfoil variants in Stage 5 is the in-house boundary element solver *panMARE*, which is aimed to simulate arbitrary potential flows in marine applications [25]. This boundary element code is based on a three-dimensional panel method with flat quadrilateral panel elements and a constant source and dipole distribution over one panel.

The governing equations for the numerical scheme are derived from the potential flow assumptions where the flow is considered to be irrotational, incompressible and inviscid. The equations for the conservation of mass and momentum are then simplified to the Laplace's equation for the total potential Φ^* and the Bernoulli equation(4.1) for the pressure p [26].

$$\nabla^2 \Phi = \nabla^2 (\Phi + \Phi_\infty) = 0 ,$$
$$\rho + \frac{1}{2} \rho |V|^2 + \rho \frac{\partial \Phi}{\partial t} + \rho g z = \rho_\infty + \frac{1}{2} \rho |V_\infty|^2 + \rho g z_\infty \quad (4.1)$$

$\forall \in \Omega$ where Ω is the flow domain, Φ is the induced potential Φ_∞ is the undisturbed free stream potential and $V = \nabla \Phi$ and $V_\infty = \nabla \Phi_\infty$ are the total velocity and the reference velocity, respectively. The induced velocity is the difference between the total and the undisturbed velocity $V_{\text{ind}} = V - V_\infty$. The constants p_∞, ρ, g and z_∞ are the constant atmospheric pressure, water density, gravity constant and the distance to the undisturbed free water surface, respectively.

The continuous solution of the Laplace's equation is obtained by Green's third identity (4.2) as a distribution of sources and dipoles on the body's surface [26].

$$\int_{\partial\Omega} \left[\mu(x) \nabla \left(\frac{1}{\|x_0 - x\|} \right) \cdot n - \frac{\sigma(x)}{\|x_0 - x\|} \right] dS(x) = 0, \sigma(x) := -\nabla \Phi(x) \cdot n \text{ and} \\ \mu(x) := -\Phi(x) \quad (4.2)$$

where x_0 is a collocation points inside a solid body [26]. To obtain a unique solution of the above equation, boundary conditions are required on the boundaries of the flow domain.

4.1.2 Numerical formulation

For the numerical simulation the in-house simulation tool panMARE is used. This programme is based on a three-dimensional panel method where the body and wake surfaces are discretised in flat quadrilateral elements and the governing equations of the potential flow problem are applied on a collocation point of each panel element (As shown in Figure 4.1 and Figure 4.2)

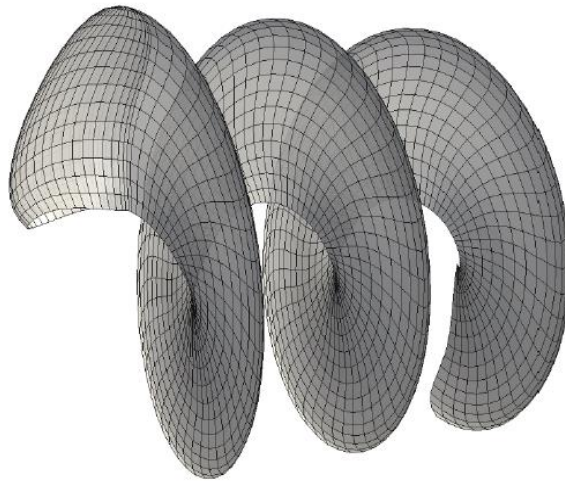


Figure 4.1 : Discretisation of a propeller blade and wake [26].

The collocation points are defined in panMARE as the centre points of the surface panels which are slightly displaced inside the body. They will be denoted in the following by $x_i, \forall j = 1, \dots, N$ where N is the number of body panels. The centre points of the body and wake panels will be denoted by $x_i, \forall i = 1, \dots, N, N + 1, \dots, N_{wake}$ where N_{wake} is the number of wake panels.

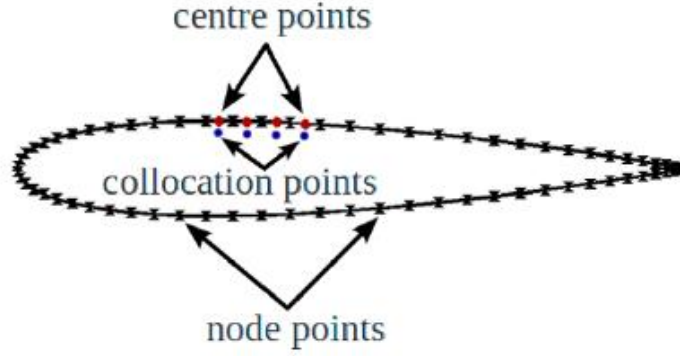


Figure 4.2 : Centre, collocation and node points on a blade profile[26].

On each body panel element a source and a dipole is distributed with a constant strength over one panel. On the wake panels only dipoles are distributed since no displacement is induced by the wake. Due to the discretisation of the geometry, equation [(4.3)&(4.4)] results in a linear equation for each collocation point

$$\int_S \left[\mu \left(\vec{x}, t \right) \frac{\partial}{\partial n} \nabla \left(\frac{1}{r_{\vec{x}_0 \vec{x}}} \right) \cdot \vec{n} - \frac{\sigma(\vec{x}, t)}{r_{\vec{x}_0 \vec{x}}} \right] dS(\vec{x}) = 0, \forall \vec{x}_0 \in \Omega_{inner} \quad (4.3)$$

$$\sum_{i=1}^{N+N_{wake}} \mu_i^n A_{i,j} - \sum_{i=1}^N \sigma_i^n B_{i,j} = 0 \quad (4.4)$$

where $\mu_i^n := \mu(x_i, t_n), \sigma_i^n := \sigma(x_i, t_n)$, are the discrete dipole and source strength(4.5) for the discrete time step t_n and

$$A_{i,j} := A \left(\vec{x}_i, \vec{x}_j \right) = \int_{Panel_i} \frac{\partial}{\partial n} \frac{1}{r_{\vec{x}_i \vec{x}_j}} dS \left(\vec{x}_i \right), \forall i = 1, \dots, N, \dots N + N_{wake}$$

$$B_{i,j} := B \left(\vec{x}_i, \vec{x}_j \right) = \int_{Panel_i} \frac{1}{r_{\vec{x}_i \vec{x}_j}} dS \left(\vec{x}_i \right), \forall i = 1, \dots, N, \quad (4.5)$$

$\forall j = 1, \dots, N$ are the influence functions which describe the dipole or source influence of the panel i on the panel j . [26].

4.2 Aspects Regarding the *Ansys CFX* Process

ANSYS CFX is a commercial CFD software designed to simulate fluid flows. It has been applied to a wide range of engineering applications, such as water flowing past ship hulls, gas turbine engines, aircraft aerodynamics, pumps, fans, HVAC systems, mixing vessels and many others. ANSYS CFX has its roots in Flow3D and TASCflow, which were developed by United Kingdom Atomic Energy Authority (UKAEA) and Advanced Scientific Computing (ASC) in Canada respectively. Flow3D was released in late 1980s and it has been renamed CFX-4 in the middle 1990s. Initially, CFX-4 was orientated to multiphase chemistry models, while TASCflow was basically used for turbo-machinery applications delivering solutions of hydrodynamic flow properties (velocities and pressures). Both of the ancestors of ANSYS CFX offered multi-block structured hexahedral meshing codes.

The toolbox ANSYS CFX mainly consists of different sub tools:

- ANSYS Designmodeller
- ANSYS CFX-Pre
- ANSYS ICEM CFD (not included in the standard package)
- ANSYS CFX-Solve
- ANSYS CFX-Post

The toolbox ANSYS CFX is fully integrated into ANSYS Workbench which is the framework for the engineering simulation tools provided by ANSYS [27]. For example, by using the Workbench framework, results from CFD simulations can be directly transferred to structural mechanics tools from ANSYS to perform fluid-structure-interaction simulations. The range of tools included in ANSYS CFX covers the complete process of preparing, running and evaluation of simulations. With ANSYS Designmodeller, which is in principal a basic CAD tool, geometry files can be generated and/or imported and modified. The created or modified models can be imported into CFX-Pre, where the pre-processing of the simulation is conducted. Using the grid generation algorithms of ANSYS CFX-Pre, geometry can be meshed

based on different grid types and refinement parameters. To complete the pre-processing, simulation parameters like turbulence models, boundary conditions and solver/output settings can be defined. For advanced mesh generation of complex geometry, a separate program module called ANSYS ICEM CFD exists and can be integrated into the toolbox. Based on the pre-processing process, simulations can be run using ANSYS CFX-Solve. The solver program supports parallel computing and provides several functions like the plotting of the residuals and the simulation variables. The evaluation of the simulation results can be conducted within ANSYS CFX-Post. Supported by several pre-defined functions (for example to extract forces from the simulation results) and a broad variety of filters, CFX-Post enables the user to conduct an efficient post-processing of the data. Furthermore the program is very stable, even when dealing with big meshes.

In the beginning of this work ANSYS CFX 14.5 was used. Later ANSYS CFX was updated to the actual version 15.0.

4.2.1 Model creation

NACA 64(3)618 airfoil has been used as blade model in our numerical analysis. Figure 4.3 shows us the surface structure of the blade profile. As seen in Figure 4.4, the datas necessary to create the blade model was obtained from the website of the related public enterprise. The script file was arranged to form the airfoil geometry in Ansys ICEM module.

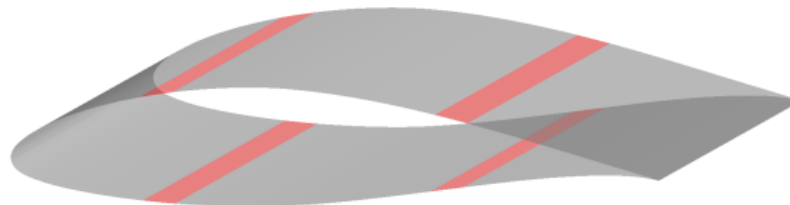


Figure 4.3: Surface representation of NACA 643618 airfoil[27].

Upper surface		Lower surface	
Station	Ordinate	Station	Ordinate
0	0	0	0
.50	1.428	.50	-1.428
.75	1.720	.75	-1.720
1.25	2.177	1.25	-2.177
2.5	3.005	2.5	-3.005
5.0	4.186	5.0	-4.186
7.5	5.076	7.5	-5.076
10	5.803	10	-5.803
15	6.942	15	-6.942
20	7.782	20	-7.782
25	8.391	25	-8.391
30	8.789	30	-8.789
35	8.979	35	-8.979
40	8.952	40	-8.952
45	8.630	45	-8.630
50	8.114	50	-8.114
55	7.445	55	-7.445
60	6.658	60	-6.658
65	5.782	65	-5.782
70	4.842	70	-4.842
75	3.866	75	-3.866
80	2.888	80	-2.888
85	1.951	85	-1.951
90	1.101	90	-1.101
95	.400	95	-.400
100	0	100	0

L. E. radius: 2.208

Figure 4.4: Stations and ordinates given in percent of airfoil chord for NACA-643618[27].

4.2.2 Boundary conditions

In order to complete the CFX problem that we are solving, it is necessary to specify boundary conditions for the domain patches. Patches of the domain on the boundaries are recognized by the solver as the boundary patches. The boundary conditions can be divided broadly into two types viz. Dirichlet and Neumann boundary conditions.

If a dependent variable is described by a value on a patch, then such type of boundary condition is called as Dirichlet boundary condition. Similarly, if a gradient is specified at the boundary patches, then the boundary condition at those patches is called as Neumann boundary condition. The inlet patch of the computational domain is set to a fixed value of velocity.

The major objective of this research was to establish a good match between *Ansys CFX* results of the simulations and *panMARE* analyses values for the flow over wind turbines. Many cases were simulated for different values of constant in-flow wind speeds. Thus, a change in the velocity boundary condition at the inlet ultimately results in the change in wind speeds all across the computational domain.

Similarly, the outlet boundary of the domain was set to a constant pressure value. The pressure at the outlet was set to be atmospheric pressure. The objects in the computational domain, around which the flow was simulated, were set to be no-slip boundaries. The no-slip boundary conditions set the stream wise and the transverse velocities to zero. Figure 4.5 shows a schematic representation the boundary conditions. In these simulations, velocity in the entire domain was set to the inlet value as the initial condition. Similarly, for pressure and eddy-viscosity term $\tilde{\nu}$, initial conditions in the domain were set to the inlet value.

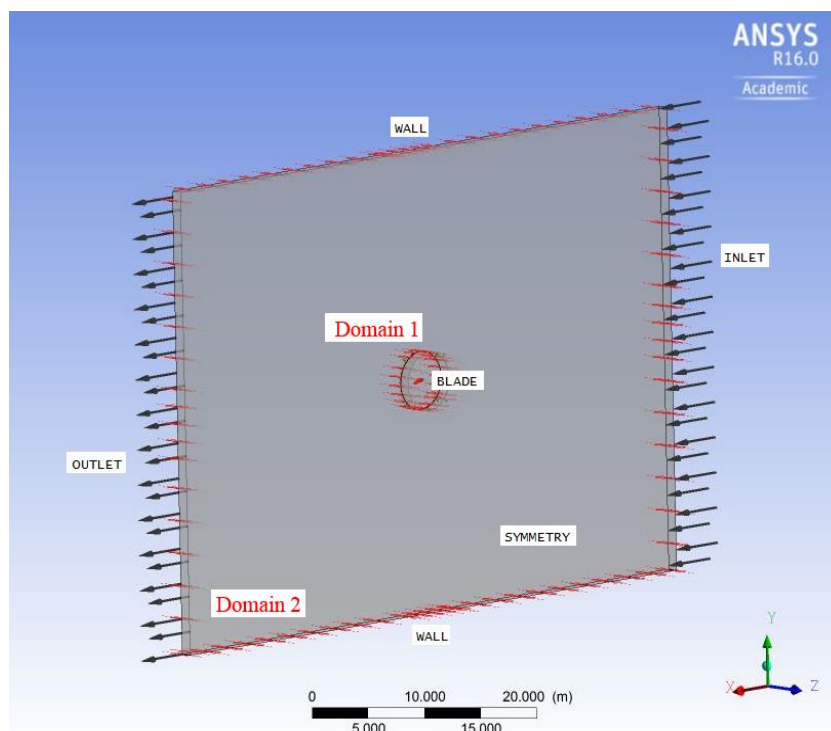


Figure 4.5: Schematic representation of boundary conditions.

In Ansys CFX Numeric Analysis, two different domain are used. The domain inside, which has circular shape, encloses the blade profile and airfoil rotates with this domain. The rectangle shaped domain is outside and stable. These two domains are interconnected with an interface surface. The circular domain are rotated instead of turning the all domains by using the interface surface. By this way, the total calculation number are reduced.

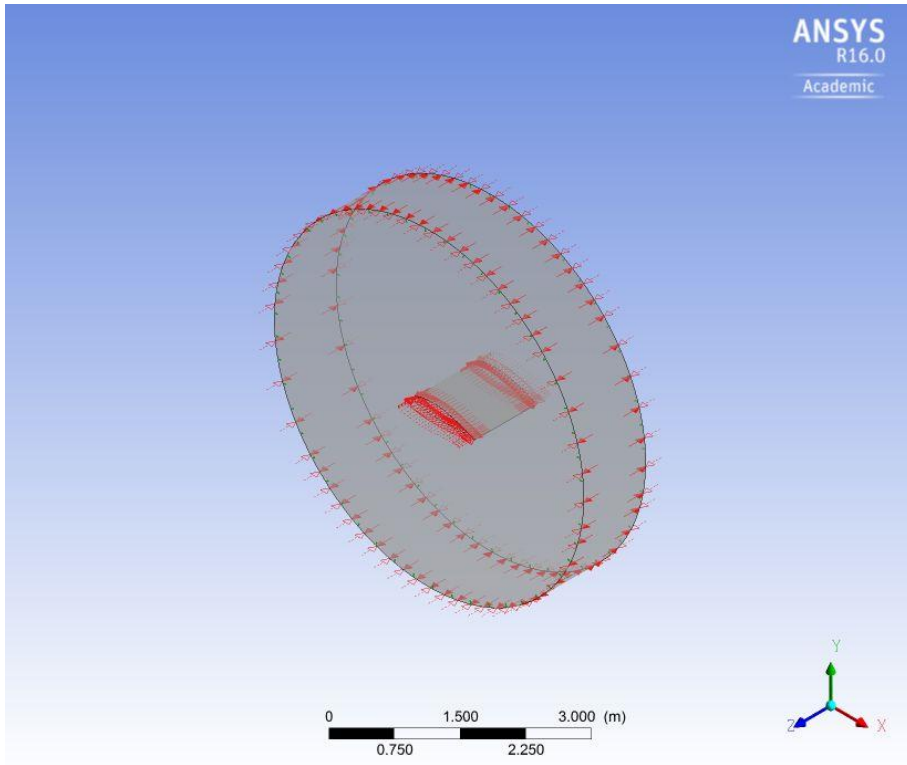


Figure 4.6: The circular domain around the blade profile.

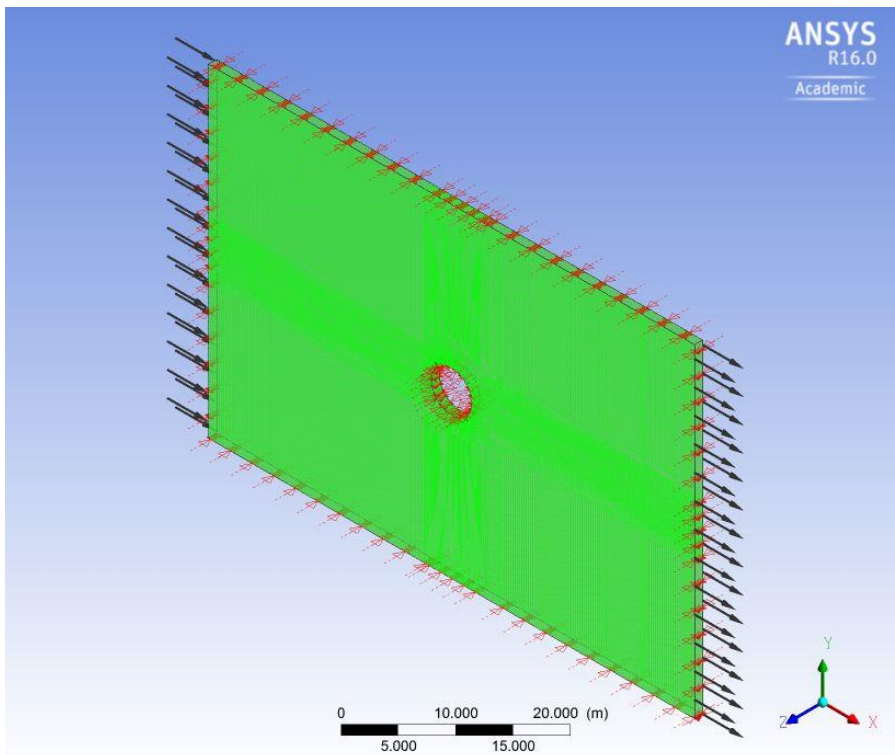


Figure 4.7: The representation of the outer domain.

In the figure 4.6 and Figure 4.7, the domains used in the analysis can be seen in detail. Besides, different types of boundary conditions, such as inlet, outlet, wall, symmetry, are defined on these domains.

4.2.3 Domain decomposition

Domain decomposition is also one of the major steps involved in pre-processing. For performing large calculations which are computationally expensive the underlying mesh is decomposed into various number of smaller meshes that are distributed to various processors for performing numerical calculations in parallel using many CPUs.

The number of partitions of the meshes, for parallel processing were made according to the complexity of the problem. For example, in this study, meshes used for flow simulations over the airfoil consisted of about 100,000 hexahedral elements.(see Figure 4.8) These meshes were decomposed into 4 smaller partitions such that the case runs on 4 processors with about 25,000 cells on each processor.

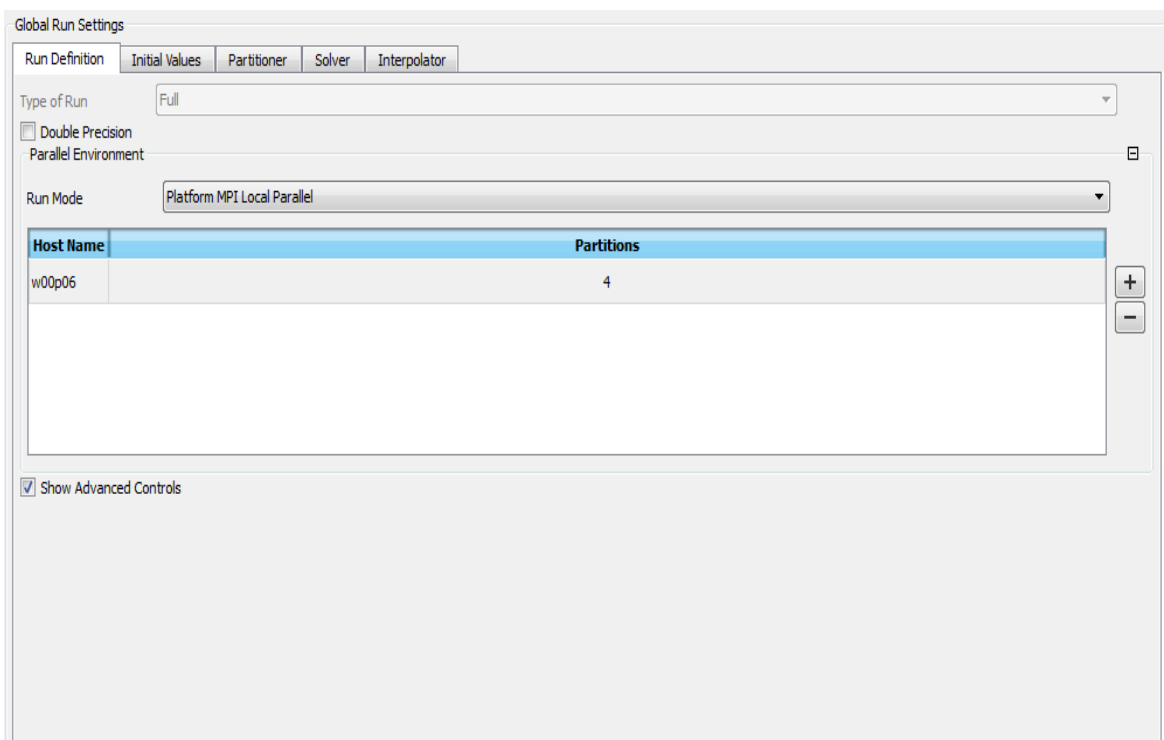


Figure 4.8: Domain decomposition in Ansys CFX.

4.2.4 Grid generation

As mentioned above, pre-processing is the first important step towards obtaining the CFX solution. Grid generation is the most important pre-processing step. It is very important to generate accurate grids for the solver so as to obtain correct results. The

accuracy of the CFX solution depends on the quality of the grid used to perform the calculations. The two types of grids that are mostly used are structured and unstructured grids.

A structured grid is a collection of regular repeating elements. Such grids are generally represented by quadrilateral elements in 2D and hexahedral elements in 3D. Since the elements are arranged in a regular repeating pattern, the connectivity information of the elements is stored implicitly. Each cell in the grid is directly addressed by the index (i, j) in 2D or (i, j, k) in 3D. This helps in saving a lot of computational effort while performing calculations. In order to improve the overall accuracy of the Ansys CFX solution, these grids can be made finer by stretching in a particular direction so that there is a large number of closely spaced grid points in a region where large gradients need to be solved [28]. The Figure 4.9 represents a typical structured grid consisting of quadrilateral elements. The downside of using such grids is their inability to resolve finely around complicated geometries, and over refinement away from the bodies.

Unstructured meshes consist of arbitrarily shaped elements which do not have any regularity among them. Such type of grids is mostly used to perform finite volume and finite element calculations. The main advantage of using unstructured meshes is their ability to resolve finely around very complex geometric topologies.

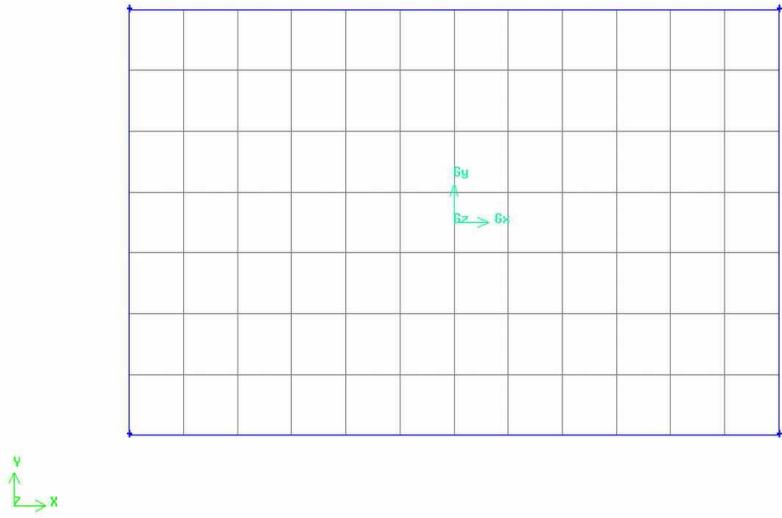


Figure 4.9: A typical 2D structured grid consisting of rectangular elements[28].

Such type of meshes is generally represented by triangles in 2D and tetrahedrons in 3D geometries. Since there is no repeating pattern of the elements, the connectivity information of the elements needs to be stored explicitly. This comes at some additional computational cost since extra memory is utilized in storing the mesh connectivity information. The advantage is that, algorithms exist to fill any space, no matter how complex the shape is, with an unstructured mesh. With the latest developments in the meshing algorithms, various mesh generators are equipped with advanced meshing options which give the user considerable control in generating very accurate unstructured meshes [29]. Figure 4.10 shows a cylindrical domain with typical unstructured (tetrahedral) mesh around a 3D finite cylinder. Unstructured meshes are used throughout this research so that accurate CFD calculations can be performed over the wind turbine blades which have reasonably complex geometry. [28].

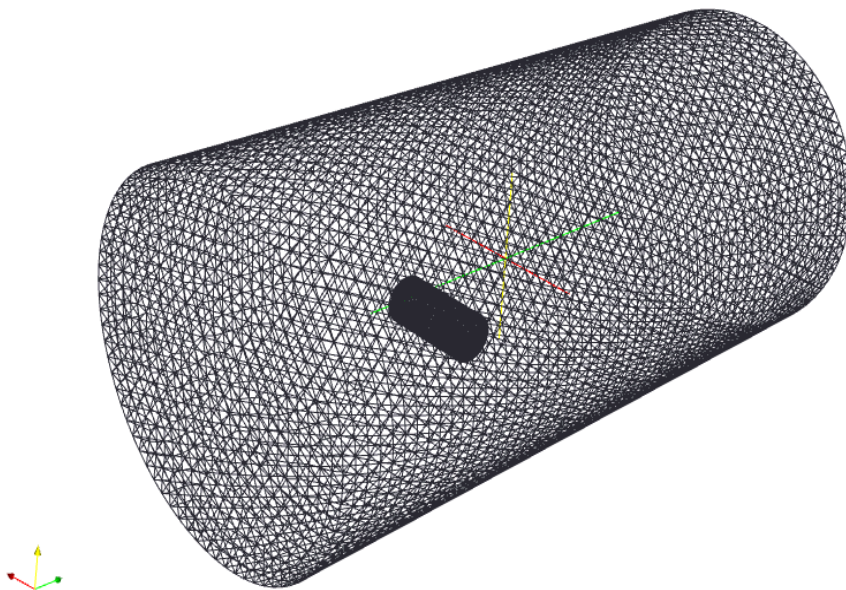


Figure 4.10: A 3D unstructured grid around a finite cylinder consisting of tetrahedral elements[28].

The mesh generation software, ICEM Cfx has been used throughout this work to generate meshes. In order to have a stable solution, care should be taken that the grid consists of least number of elements with high aspect ratios (skewed elements). Thus

good mesh generation requires a fair amount of experience, and some careful interpretation by the user. In this work, generating good quality (less skewed elements) tetrahedral meshes around wind turbine rotor, required spending a considerable amount of time and efforts.

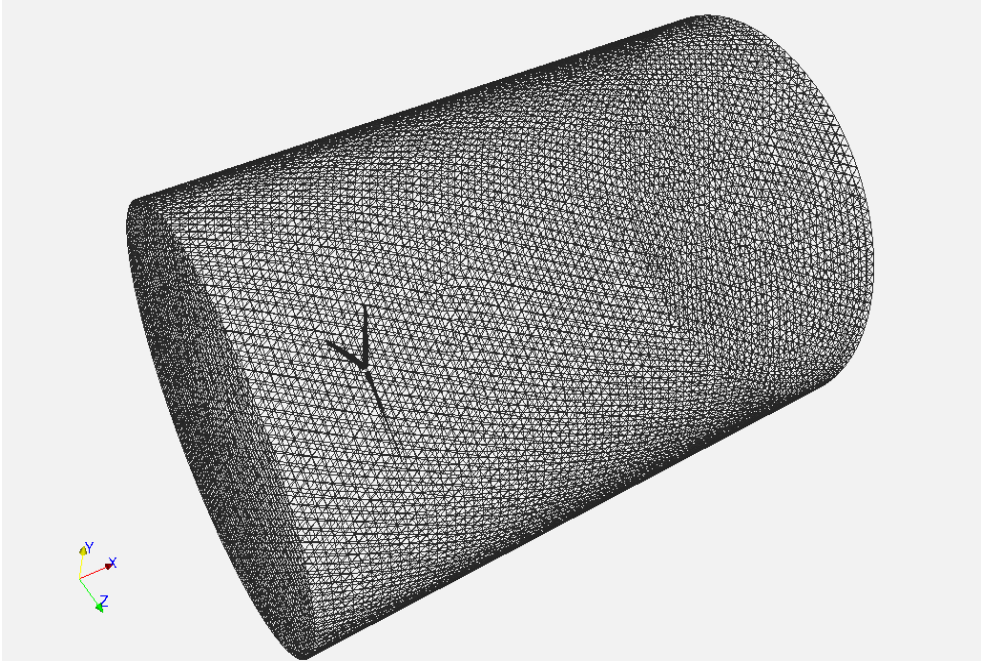


Figure 4.11: Unstructured mesh consisting of 2 million tetrahedral elements around a wind turbine rotor[28].

Figure 4.11 shows a 3D mesh around a wind turbine rotor while Figure 4.12 shows the surface mesh consisting of triangles on one of the wind turbine blades

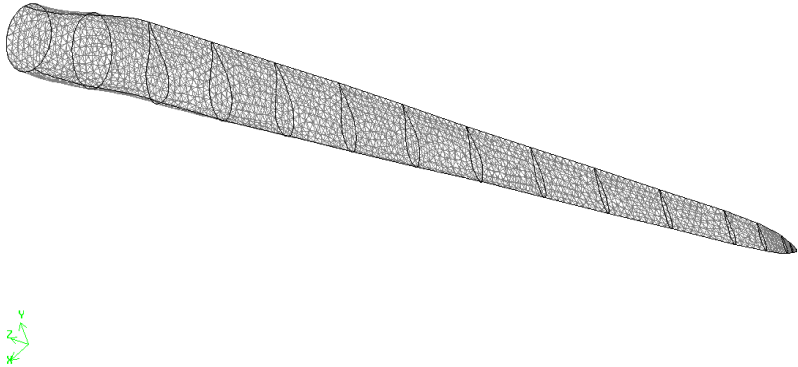


Figure 4.12: Surface mesh showing triangular elements on a wind turbine blade[28].

Approximations are used to solve the governing differential equations of fluid mechanics. This is accomplished by converting partial derivatives to a finite difference form. These finite difference equations, also known as approximate algebraic equations, are solved at discrete points inside the domain interest. Hence, a set of grid points need to be defined within the boundaries of the domain.

In order to obtain more accurate results in the boundary layer, a dense or fine mesh is necessary to calculate viscous shear layer behavior ($y^+ = 1$). However, a fine mesh throughout the domain causes an increase in grid points, and eventually the CPU time. It is recommended to tailor the grid size near the wall to add precision. This process is referred to as clustering, which is easier to implement by using structured mesh[29].

4.2.5 Solver

The CFD solver does the flow calculations and produces the results. FLUENT, FloWizard, FIDAP, CFX and POLYFLOW are some of the types of solvers. FloWizard is the first general-purpose rapid flow modeling tool for design and process engineers built by Fluent. POLYFLOW (and FIDAP) are also used in a wide range of fields, with emphasis on the materials processing industries. FLUENT and CFX two solvers were developed independently by ANSYS and have a number of things in common, but they also have some significant differences. Both are control-volume based for high accuracy and rely heavily on a pressure-based solution technique for broad applicability. They differ mainly in the way they integrate the fluid flow equations and in their equation solution strategies. The CFX solver uses finite elements (cell vertex numerics), similar to those used in mechanical analysis, to discretize the domain. In contrast, the FLUENT solver uses finite volumes (cell centered numerics). CFX software focuses on one approach to solve the governing equations of motion (coupled algebraic multigrid), while the FLUENT product offers several solution approaches (density-, segregated- and coupled-pressure-based methods).

ANSYS CFX solver can replicate a wide range of physical models including steady-state or transient incompressible or compressible flows varying from subsonic to hypersonic, laminar or turbulent flows, Newtonian or non-Newtonian flows and ideal or real gases. The main focus of ANSYS CFX software is to deliver fast and reliable convergence, which is scalable with mesh size. This is achieved by using coupled algebraic multi-grid techniques. Boundary layers can be captured efficiently with high-

aspect ratio mesh cells without influencing the accuracy. The accuracy is also enhanced by using a second-order advection numerical scheme by default[29].

4.2.6 Post-processing

ANSYS CFX has post-processing tools able to translate the results from the CFD simulations to graphs, animations and reports that are easily transferable. The data can also be exported to ANSYS CFD-Post, third-party graphics and CAE packages for further interpretation. Using ANSYS Workbench CFD data can be mapped to ANSYS simulation surfaces as added thermal and pressure loads.

5. RESULTS

The numerical analyses of the NACA 64(3)618 have been carried out by using the Panel and RANS calculation methods in this part. *Ansys CFX* and *panMARE* simulation tools were used by working on these methods to analyse the airfoil in two dimension.

In the sections below, there are important points related to the analyses performed *Ansys CFX* and *panMARE* and the graphs and tables with regard to the results of the analyses. At the end of this part, the comparative examination between the results of these programs was included.

5.1. *Ansys CFX* Analysis

Pre-processing and post-processing are two important steps in achieving the *Ansys-CFX* solution. Pre-processing involves grid generation and converting the grid into a format which can be understood by the *CFX* solver. It is often the most time consuming and tedious jobs in achieving the *CFX* solution. Post processing is the final step in a *CFX* analysis of a problem. It involves visualization of the results obtained from the solver. It is often done by a post-processing software which is coupled to the *CFX* solver. The following sections explains in the steps involved in pre-processing and post-processing in different cases used in this study.

As angle of attack of blade profile between -5 and 15 degrees has been investigated in numerical simulation. The two simulations with different values of the Reynolds number (4.22×10^4 ve 1.6×10^5) were made. In resolution, pressure-dependent analysis methods providing more accurate results were used for the incompressible flows. In analysis, k-epsilon realisable turbulence model has been preferred. As fluid, the air with $1,225 \text{ kg/m}^3$ density and with $1,7894 \times 10^{-5} \text{ kg/m.s}$ viscosity has been used. For convergence, the situation has been continued until the remains of each parameter is resolved up to 1×10^{-7} .

Reynolds number is determined from the equation

$$\text{Re} = \frac{U \cdot L}{\nu}$$

ν - fluid velocity

d - diameter of the pipe

μ - dynamic viscosity of the fluid

ν - kinematic fluid viscosity: $\nu = \mu / \rho$

Table 5.1: Lift and drag coefficients ($\text{Re}=4.22 \times 10^4$).

Re=4.22x10⁴				
Angle of Attack(Degrees)	F_L(N)	F_D(N)	C_L	C_D
-5	0,69518	0,120787	0,126592	0,021995
-4	0,10317	0,113618	0,018762	0,020661
-3	0,49348	0,107921	0,089643	0,019604
-2	1,09359	0,104953	0,198505	0,019051
-1	1,69295	0,104652	0,307158	0,018987
0	2,29465	0,105658	0,416263	0,019167
1	2,88345	0,108287	0,522529	0,019647
2	3,46627	0,112479	0,629185	0,020417
3	4,02791	0,117889	0,731689	0,021415
4	4,58178	0,125881	0,833192	0,022891
5	5,09965	0,136048	0,928641	0,024774
6	5,59685	0,149421	1,020894	0,027255
7	6,03677	0,164221	1,103332	0,030014
8	6,43032	0,180772	1,167962	0,033115
9	6,82487	0,204344	1,223504	0,037531
10	7,12677	0,230497	1,262782	0,042459
11	7,34361	0,262986	1,287108	0,048612
12	7,50469	0,307535	1,291809	0,057035
13	7,62849	0,355853	1,270254	0,066251
14	7,62366	0,413446	1,235315	0,077298
15	7,55962	0,484585	1,189732	0,091008

In table 5.1, it can be seen the lift and drag coefficient data obtained from simulation of NACA 643618 blade profile at Reynolds number 4.22×10^4 . By increasing the angle of attack of the blade profile it can be understood that there are increasing at the lift and drag coefficients up to a certain point.

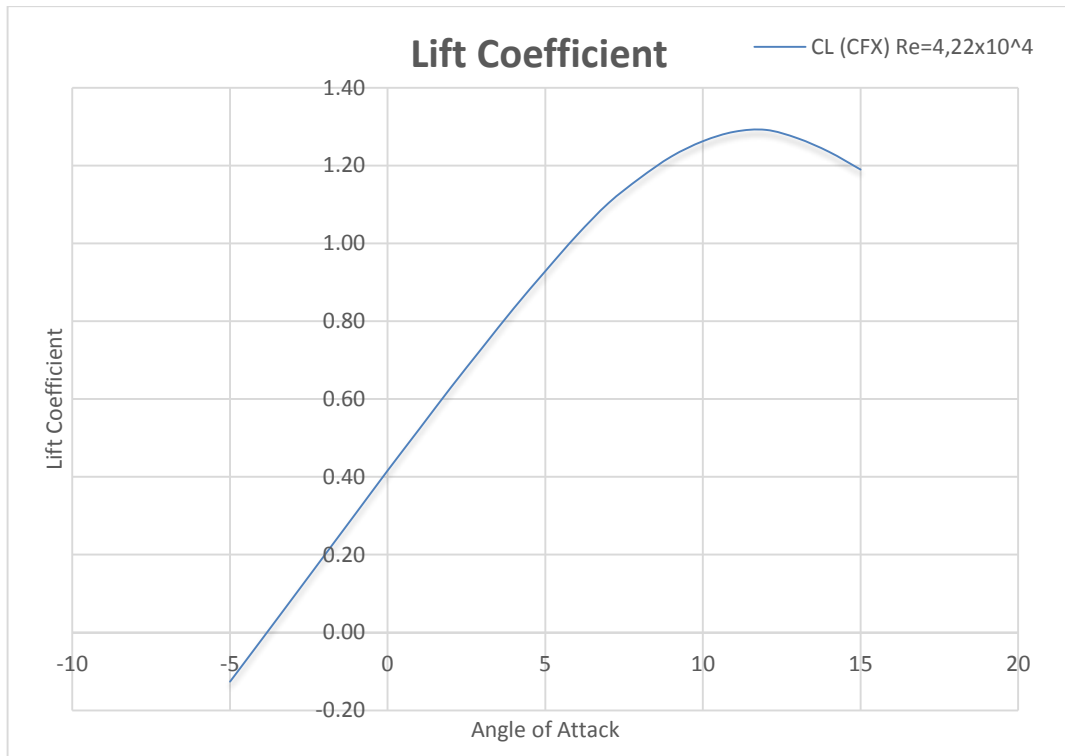


Figure 5.1: Lift coefficient vs angle of attack ($Re=4.22 \times 10^4$).

The variation of lift and drag coefficient datas with regard to the angle of attack has been presented at Figure 5.1 and Figure 5.2. It is the fact that the C_L values with regard to Reynold Number don't change too much until 10° angles of attack. However, it is seen that the lift coefficient changes between 10° - 15° angles of attack, therefore in low Re numbers (42.200) it can be understood that the lift loss is more.

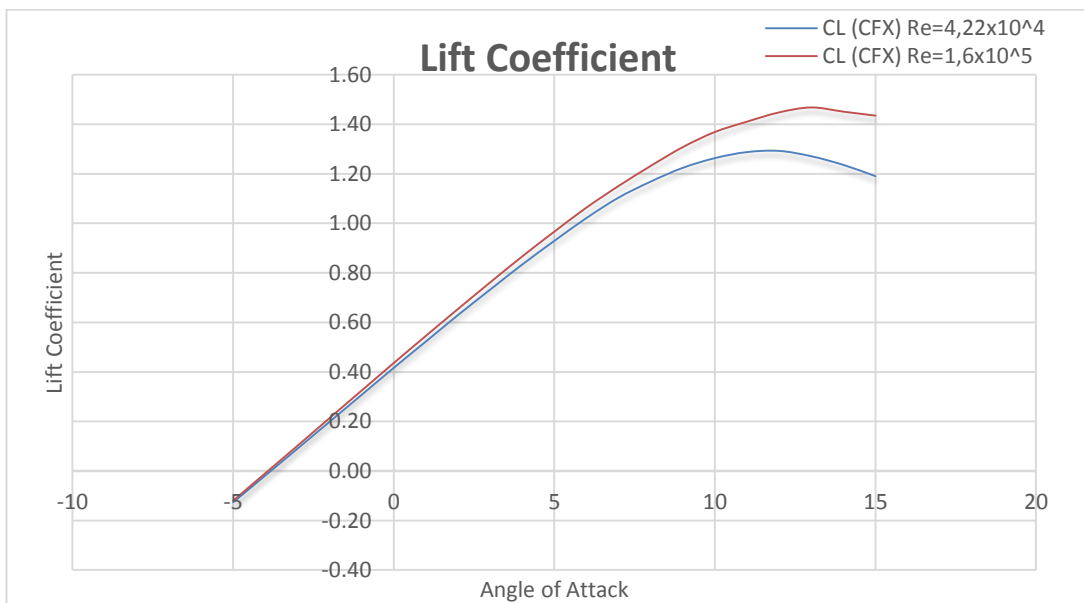


Figure 5.2 Lift coefficients for Reynolds numbers 1.6×10^5 and 4.22×10^4 .

In Table 5.2, it is showed the lift and drag coefficient data obtained from simulation of NACA 643618 blade profile for Reynolds number 1.6×10^5 .

Table 5.2: Lift and drag coefficients ($Re=1.6 \times 10^5$).

Re=1.6x10⁵				
Angle of Attack(Degrees)	F_L(N)	F_D(N)	C_L	C_D
-5	-9,52299	1,38239	-0,12009	0,017433
-4	-0,7316	1,28956	-0,00921	0,01624
-3	8,05591	1,21824	0,101343	0,015325
-2	16,9799	1,1803	0,213444	0,014837
-1	25,8447	1,1786	0,32473	0,014809
0	34,702	1,19035	0,435952	0,014954
1	43,4267	1,22092	0,545641	0,01534
2	52,0377	1,26949	0,654134	0,015958
3	60,518	1,3338	0,761315	0,016779
4	68,7919	1,42463	0,866325	0,017941
5	76,6457	1,54421	0,966558	0,019474
6	84,1962	1,70426	1,063561	0,021528
7	90,924	1,87081	1,150832	0,023679
8	97,1053	2,08183	1,231897	0,026411
9	102,831	2,36535	1,307942	0,030086
10	107,317	2,70584	1,368993	0,034517
11	110,236	3,13892	1,410786	0,040171
12	112,748	3,70891	1,448067	0,047635
13	113,86	4,42944	1,468018	0,05711
14	112,072	5,34621	1,451033	0,069219
15	110,324	6,36781	1,434863	0,082819

Also it can be obtained in Figure 5.3 that the drag coefficient shows a rapid rise after approximately the number of 12° in Reynolds Numbers.

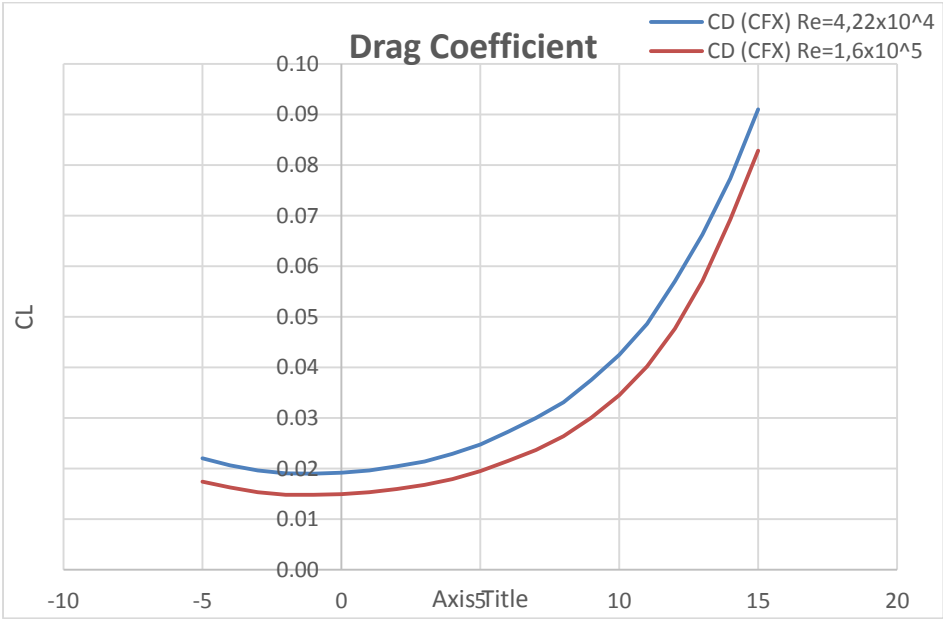


Figure 5.3 Drag coefficients for Reynolds numbers 1.6×10^5 and 4.22×10^4 .

In Figure 5.4, the changing of C_L/C_D with the angle of attack for different Reynolds Numbers is shown. It is seen that C_L/C_D increases until approximately 9° angle of attack and after that value it decrease. It is understood that drag forces begin to increase and lift forces to decrease after that point.

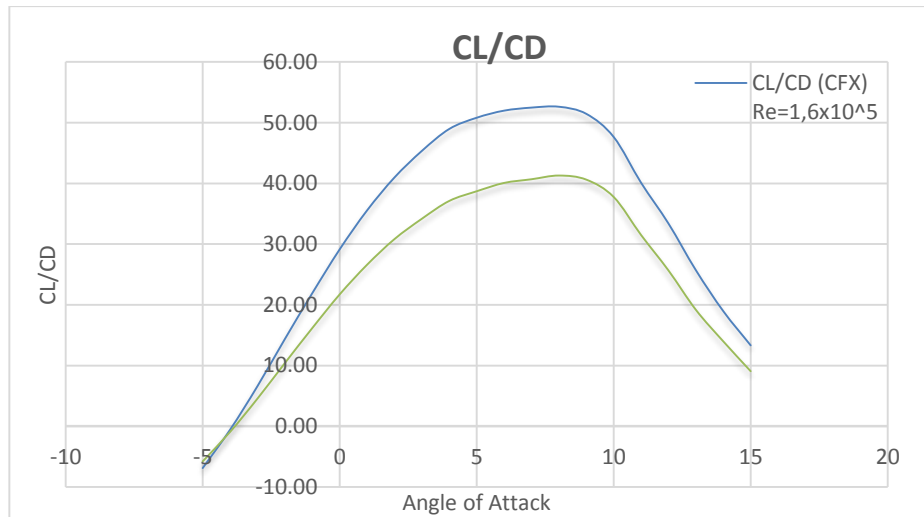


Figure 5.4: The changing of the C_L/C_D via angle of attack.

Air Flow around NACA 64(3)618 at Zero Degree

Figure 5.5 shows static pressure distribution at 1.66×10^5 Reynolds Number. It can be observed that there is high pressure of 78.05 Pascal and at trailing edge pressure is 34.01 Pascal. Resultant pressure is 34.04 Pascal.

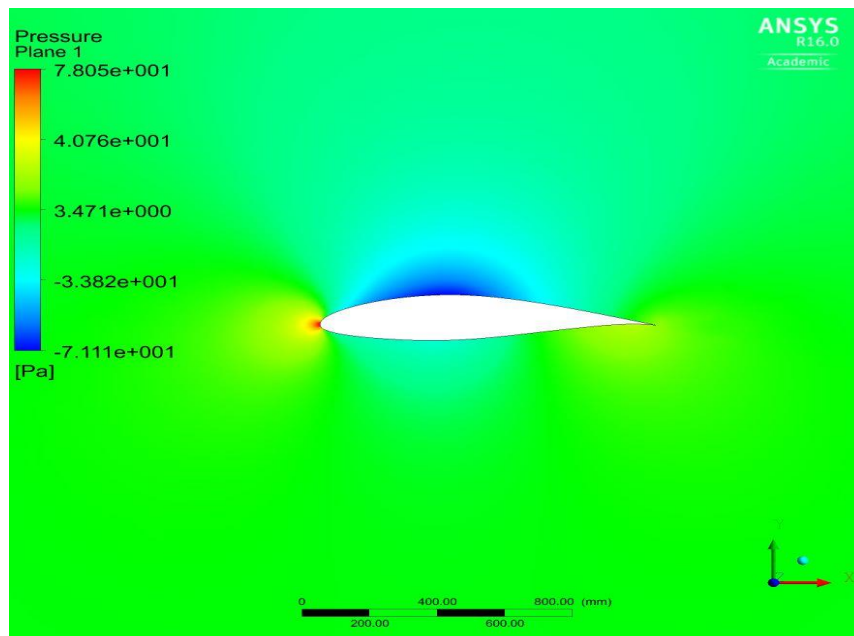


Figure 5.5 : Static pressure at zero degree(Ansys CFX).

Figure 5.6 indicates dynamic pressure at zero degree. As shown in the figure, a weak shock is formed near the trailing edge of the airfoil.

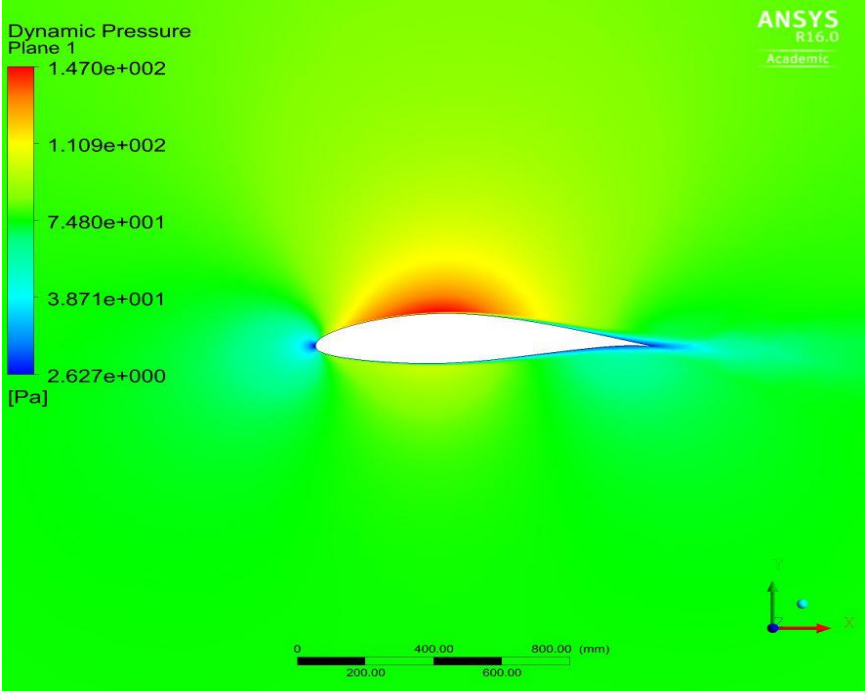


Figure 5.6 : Dynamic pressure at zero degree(Ansys CFX).

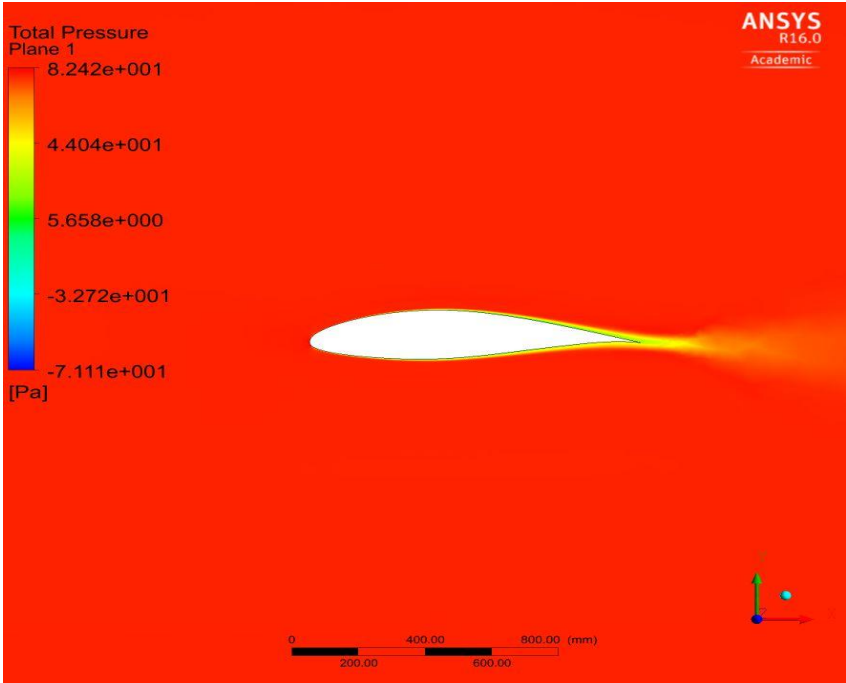


Figure 5.7 : Total pressure at zero degree(Ansys CFX).

In Figure 5.7 it can be seen the total pressure values and the dynamic pressure can be also calculated by using the static pressure and total pressure values. A reduction is observed in dynamic pressure at the points where the air layer meets and leaves the

profile, and correspondingly a decrease is observed in the air speed at the same points (see Figure 5.8).

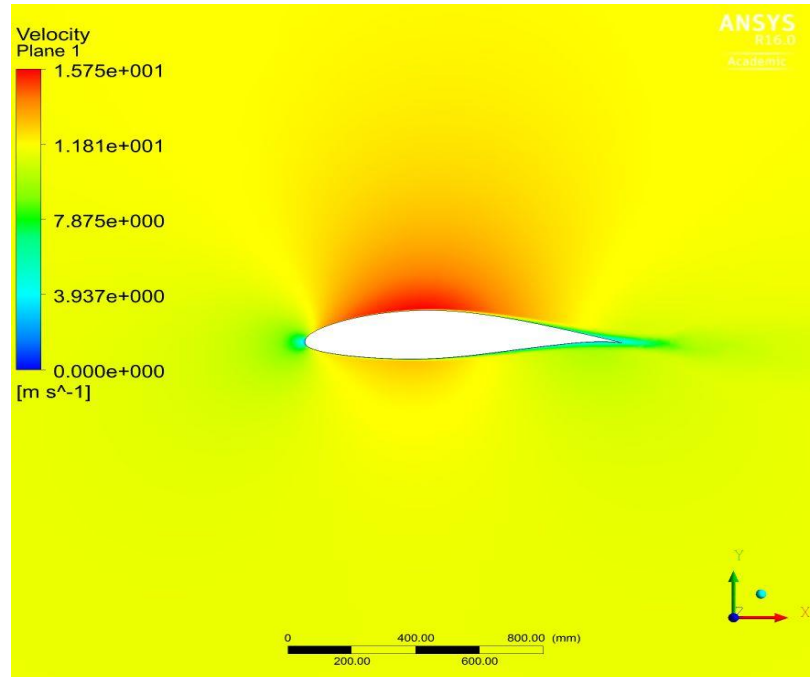


Figure 5.8 : Velocity at zero degree (Ansys CFX).

In Figure 5.9 the resulting flow turbulence distribution on the airfoil at 0° angle of attack.

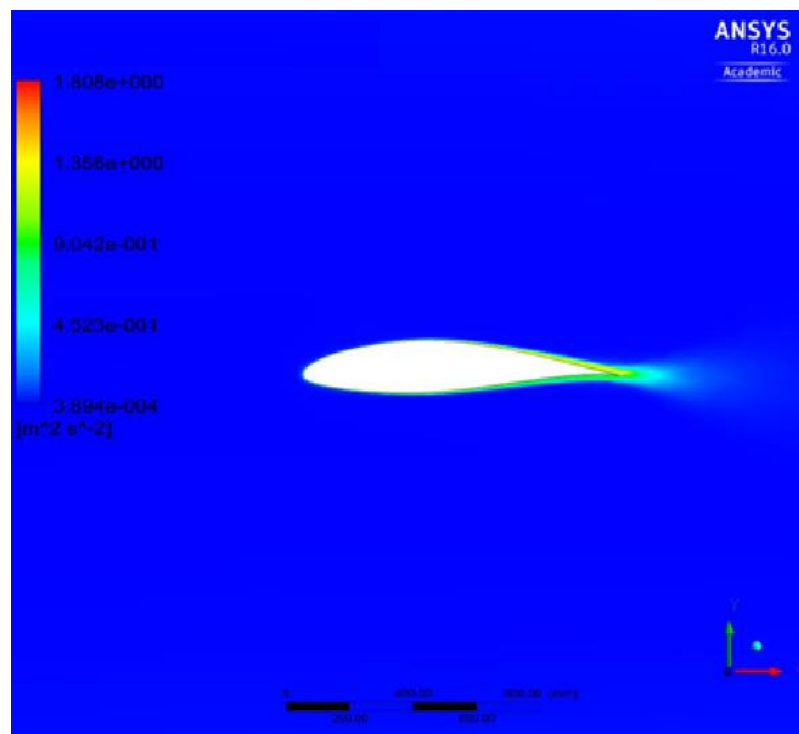


Figure 5.9 : Flow turbulence on the airfoil at zero degree(Ansys CFX).

Air Flow around NACA 64(3)618 at Five Degrees

Figure 5.10 shows static pressure contour at 1.6×10^5 Reynolds number. It can be observed that there is high pressure of 81,64 Pascal and at trailing edge pressure is 19,62 Pascal. Resultant pressure is 62,02 Pascal.

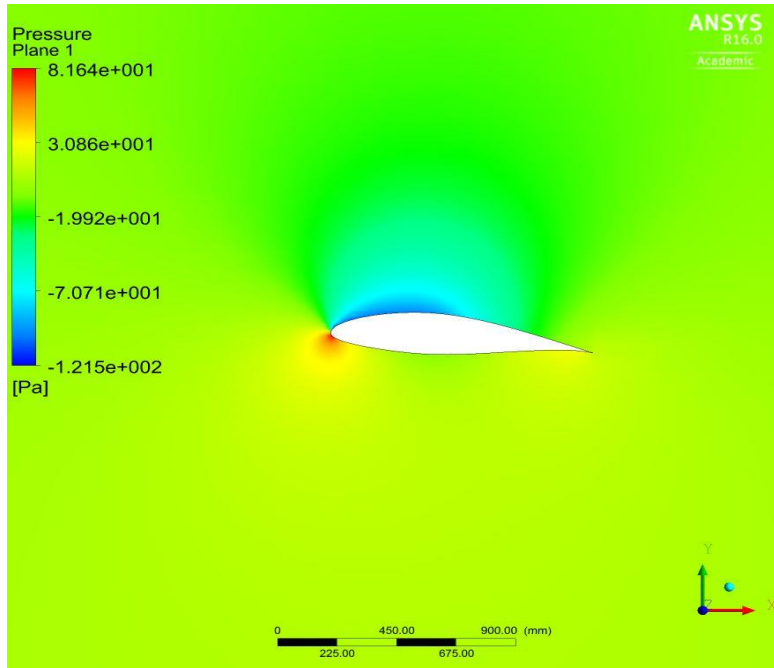


Figure 5.10 : Static pressure at five degrees(Ansys CFX).

Figure 5.11 indicates dynamic pressure at five degrees. It can be seen that at the lower surface of the trailing edge high pressure region is there which compensates for lift loss due to flat upper surface.

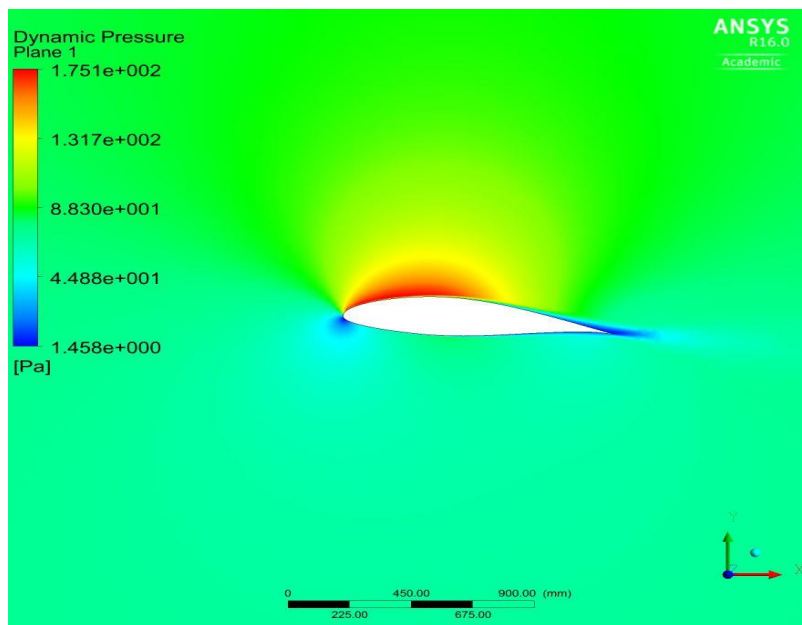


Figure 5.11 : Dynamic pressure at five degrees(Ansys CFX).

With reaching the angle of attack to 5° , static and dynamic pressure distribution in 0° the angle of attack gets lost, and on the upper surface of the profile high pressures and on the bottom surface of profile low pressure zones are occurred. It can be understood that these pressure zones creates the lifting. The total pressure distribution is as Figure 5.12.

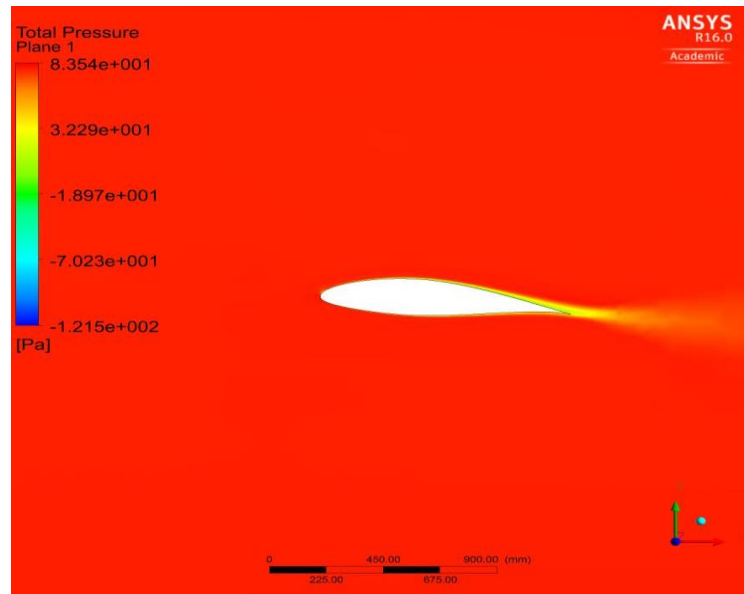


Figure 5.12 : Total pressure at five degrees (Ansys CFX).

In Figure 5.13 the velocity distribution at 5° angle of attack, and in Figure 5.14 the flow turbulence are given.

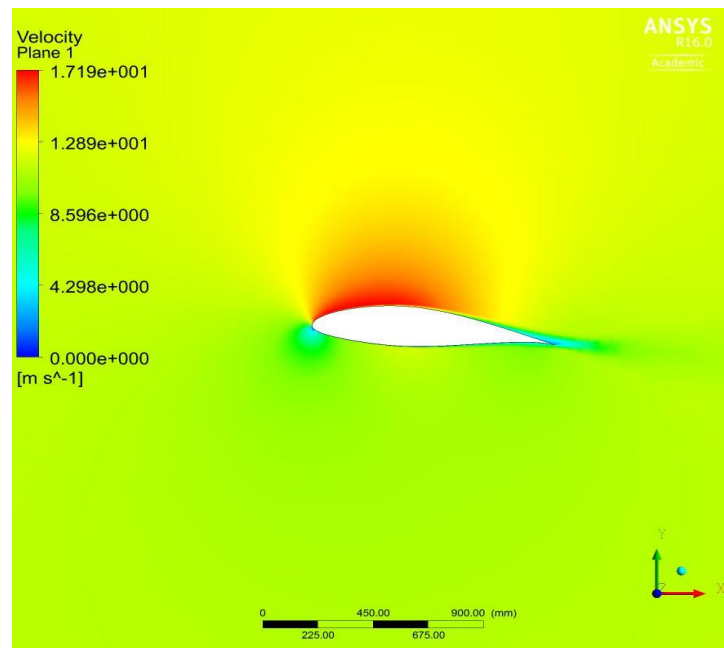


Figure 5.13 : Velocity at five degrees (Ansys CFX).

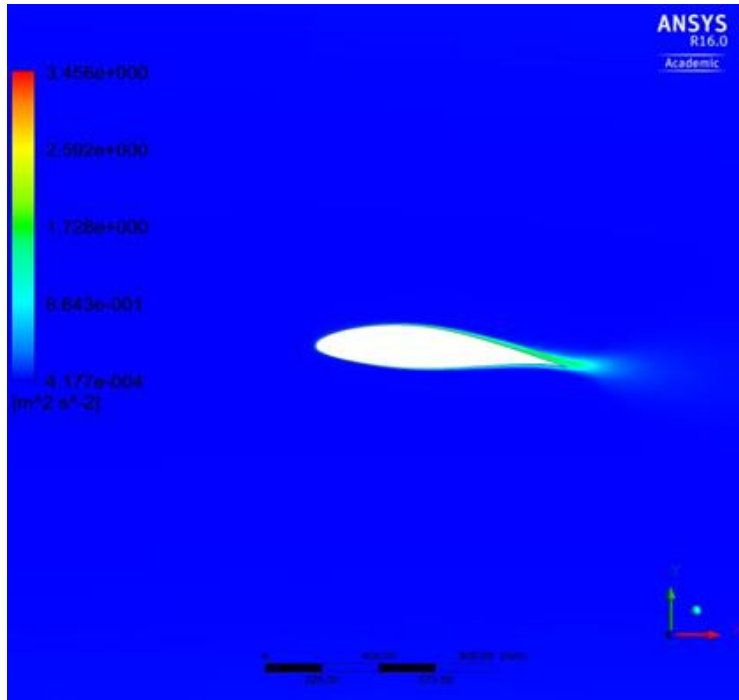


Figure 5.14 : Flow turbulence on the airfoil at five degrees (Ansys CFX).

Air Flow around NACA 64(3)618 at Ten Degrees

Figure 5.15 shows static pressure contour at 1.6×10^5 Reynolds number. It can be observed that there is high pressure of 81,32 Pascal and at trailing edge pressure is -19,96 Pascal. Resultant pressure is 101,28 Pascal.

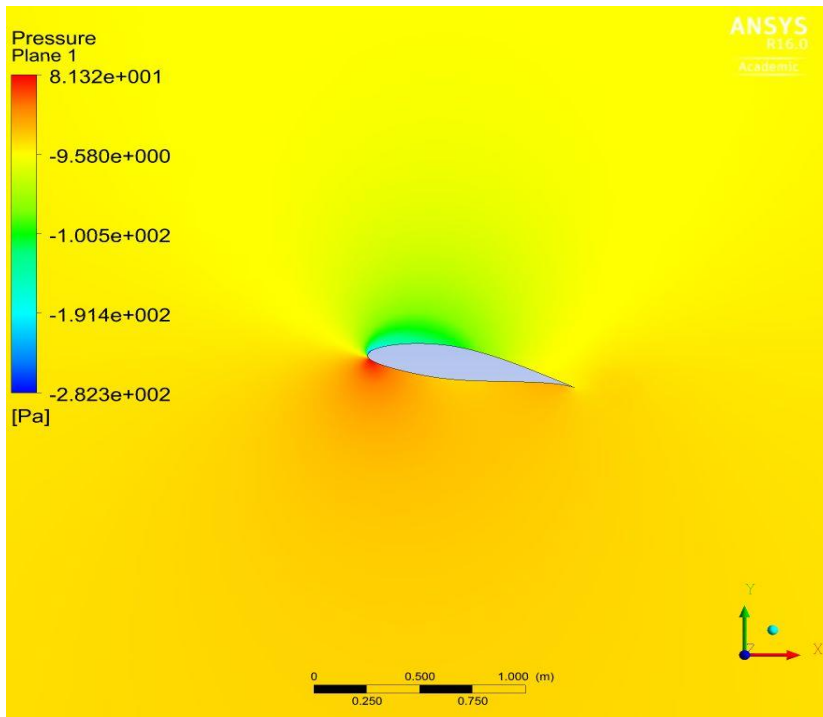


Figure 5.15 : Static pressure at ten degrees (Ansys CFX).

In 10° angle of attack, it can be seen that the increment of dynamic pressure generated on the upper surface of the profile becomes more apparent, and dynamic low pressure area occurred on the bottom surface of the profile enlarges in Figure 5.16.

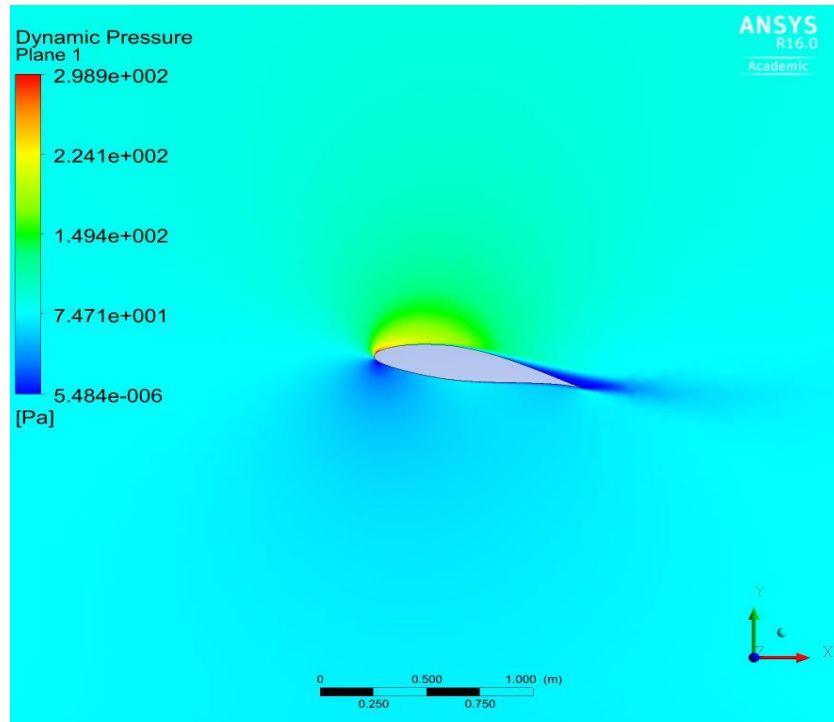


Figure 5.16 : Static pressure at ten degrees (Ansys CFX).

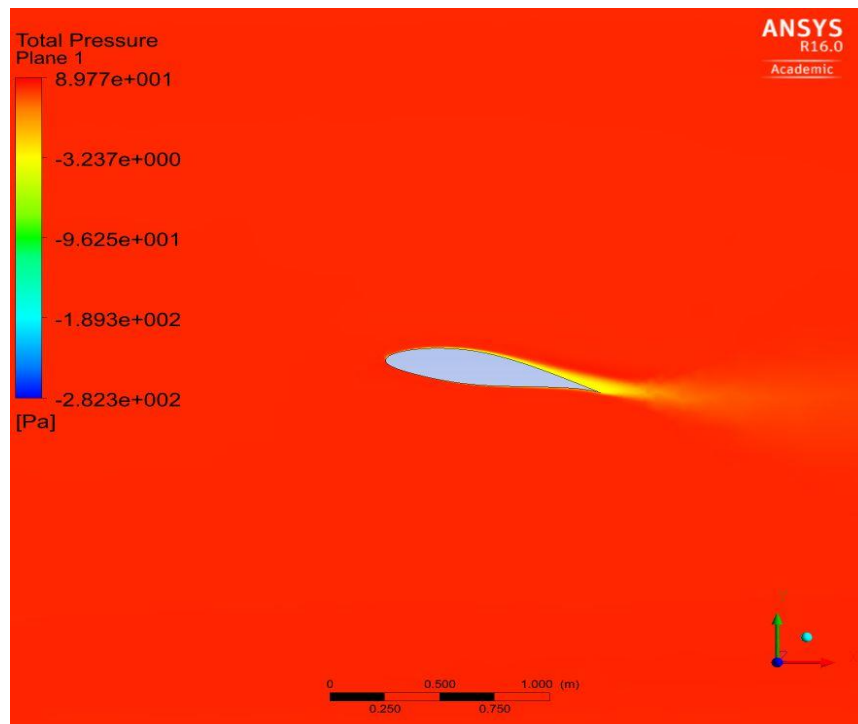


Figure 5.17 : Total pressure at ten degree (Ansys CFX).

Figure 5.17 shows contours of total pressure ,combined effect of static pressure and dynamic pressure.

In Figure 5.18 the distribution of air velocity at 10° angle of attack, and the resulting flow turbulence distribution is given in Figure 5.19.

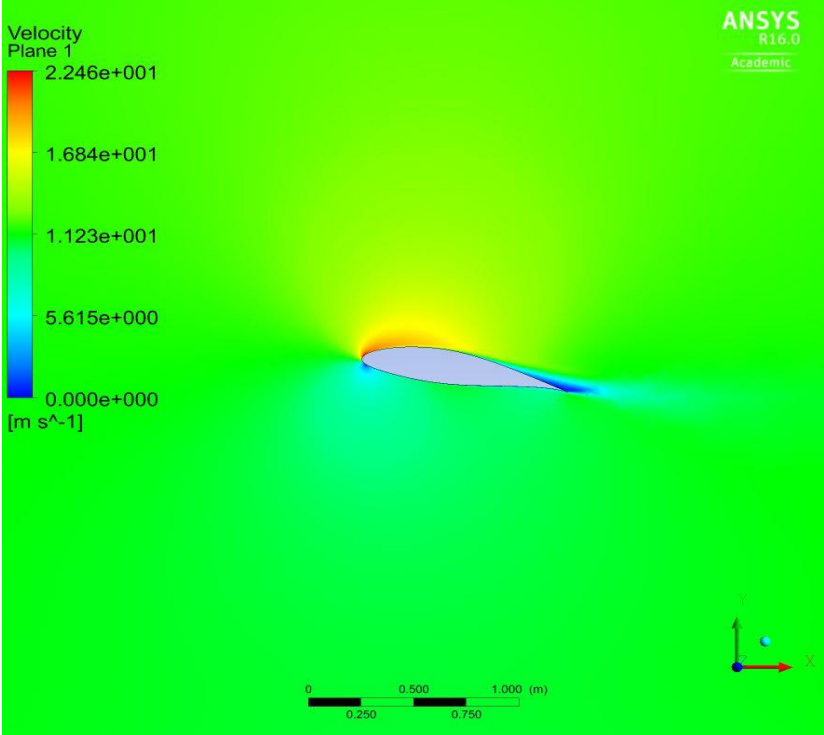


Figure 5.18 : Velocity at ten degrees (Ansys CFX).

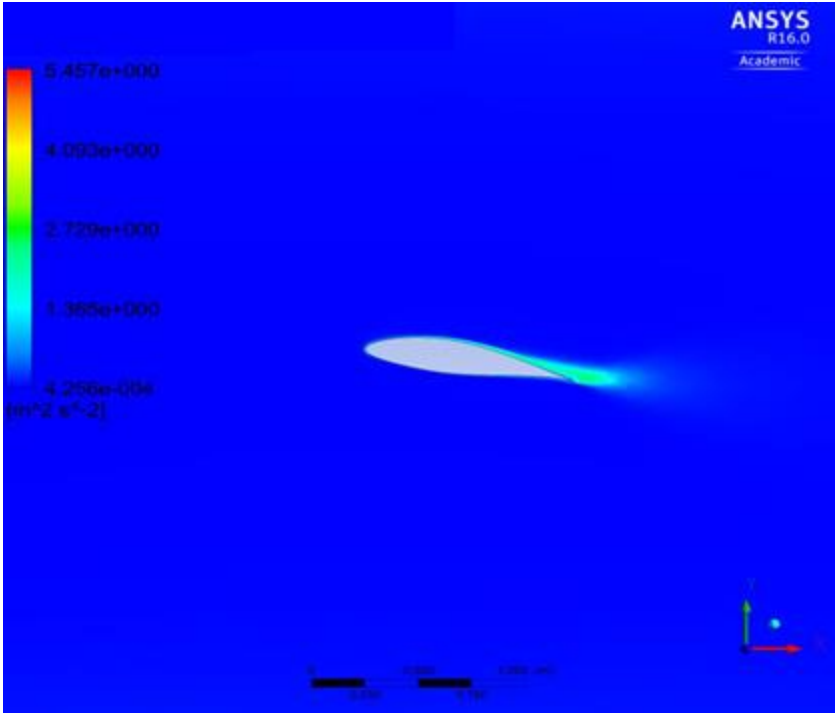


Figure 5.19 : Flow turbulence on the airfoil at ten degrees (Ansys CFX).

Air Flow around NACA 64(3)618 at Fifteen Degrees

Figure 5.20 shows static pressure contour at 1.6×10^5 Reynolds number. It can be observed that there is high pressure of 80,32 Pascal and at trailing edge pressure is -1,16 Pascal. Resultant pressure is 81,48 Pascal.

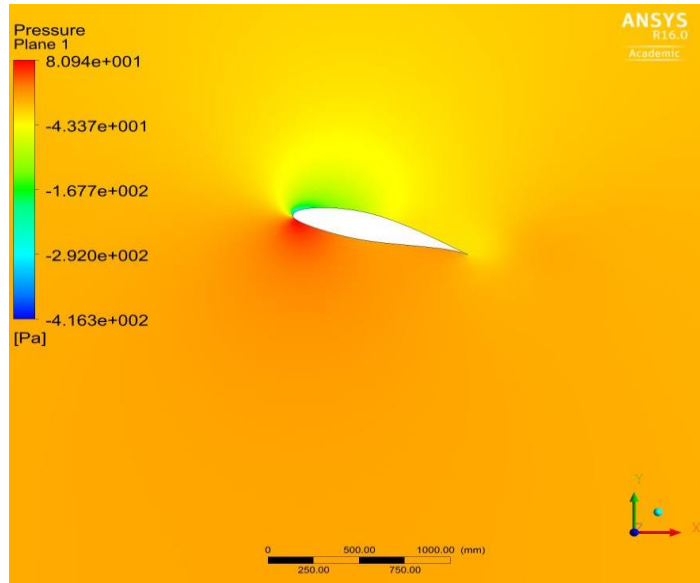


Figure 5.20 : Static pressure at fifteen degrees (Ansys CFX).

It is seen that the high dynamic pressure region which generates lifting saves its presence at 15° angle of attack. (see Figure 5.21) Furthermore it is leapt out that the boundary layer separation begins at near the trailing edge of the profile's upper surface, and if it is continued to increase the angle of attack, it is certain that the lifting losses will rise.

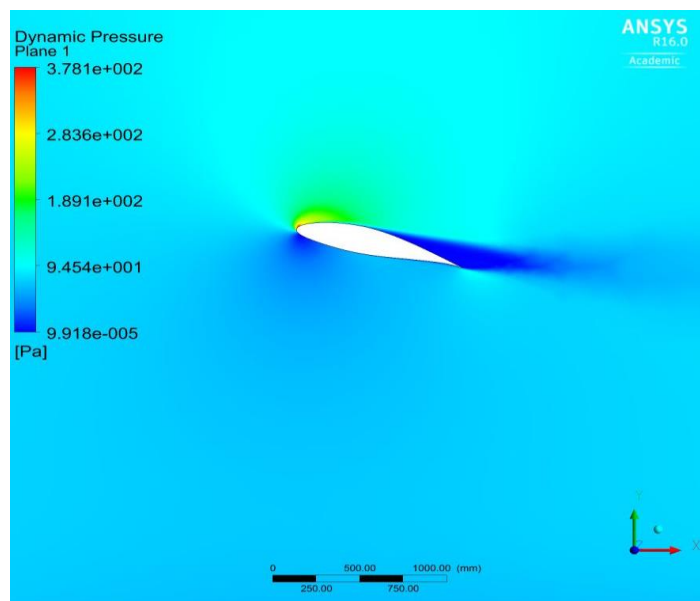


Figure 5.21 : Dynamic pressure at fifteen degrees (Ansys CFX).

Figure 5.22 shows contours of total pressure ,combined effect of static pressure and dynamic pressure.

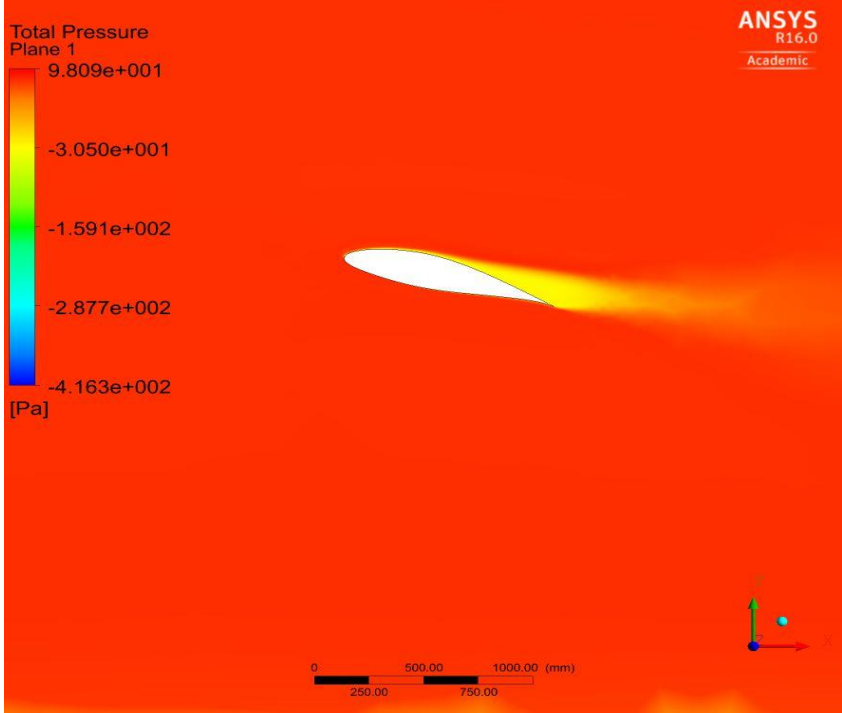


Figure 5.22 : Total pressure at fifteen degrees (Ansys CFX).

In Figure 5.23 the distribution of air velocity at 15° angle of attack, and the resulting dynamic pressure distribution is given in Figure 5.24.

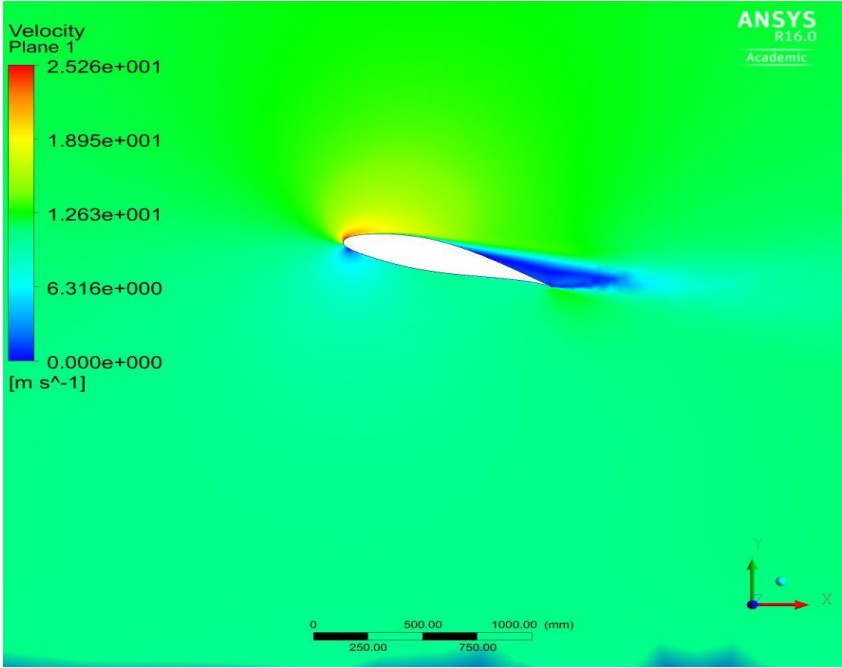


Figure 5.23 : Velocity at fifteen degrees (Ansys CFX).

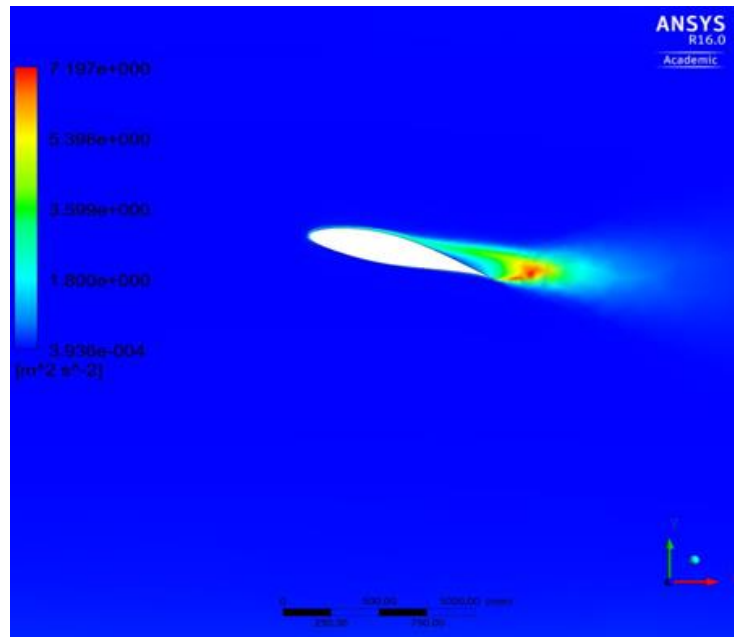


Figure 5.24 : Flow turbulence on the airfoil at fifteen degrees (Ansys CFX).

5.2 panMARE Analysis

The simulation tool used here for the computation of the airflow around the blade profile is the boundary element solver *panMARE* which is aimed to simulate arbitrary potential flows in marine applications.

As mentioned in the Section 4, Panel Method is a numerical method based on panel method. Thanks to the speed and the pressure values found by the means of this method, the lifting and dragging effects to be occurred on airfoil can be effectively calculated within a much shorter time than Ansys CFX.

In this thesis, the speed and the pressure values in the range of -5° and 15° of angle of attack is numerically calculated by panel method for different Reynolds numbers and these calculations is compared with solutions of Ansys CFX program. The solution is subsonic and the flow has considered as incompressible and inviscid.

First, the script file has been written by using the datas related to the blade profile. In Figure 5.25 consists of these datas need to form the blade geometry in *panMARE*.

However, *panMARE* is able to calculate the equations in a short time, generating the program to get solutions is the phase takes the most time in the numerical analysis.

The number of panels used, theirs size and the distrubition on a blade body are effective on the accuracy of the results. For this reason, it is better to put panel more frequently through the trailing and leading edge.

Number	x/c	y/c	Number	x/c	y/c	Number	x/c	y/c	Number	x/c	y/c
1	1	0	52	0,22	0,101985	103	0	0	154	0,22	-0,05905
2	0,99	0,003385	53	0,21	0,100084	104	0,0001	-0,00209	155	0,23	-0,05966
3	0,98	0,006126	54	0,2	0,098068	105	0,0002	-0,00295	156	0,24	-0,06022
4	0,97	0,008767	55	0,19	0,095934	106	0,0003	-0,00361	157	0,25	-0,06072
5	0,96	0,011357	56	0,18	0,093676	107	0,0004	-0,00417	158	0,26	-0,06116
6	0,95	0,013921	57	0,17	0,091291	108	0,0005	-0,00466	159	0,27	-0,06155
7	0,94	0,016478	58	0,16	0,088772	109	0,00075	-0,0057	160	0,28	-0,06187
8	0,93	0,019036	59	0,15	0,08611	110	0,001	-0,00657	161	0,29	-0,06214
9	0,92	0,021598	60	0,14	0,083298	111	0,00125	-0,00734	162	0,3	-0,06234
10	0,91	0,024163	61	0,13	0,080329	112	0,0015	-0,00803	163	0,31	-0,06249
11	0,9	0,026733	62	0,12	0,077188	113	0,00175	-0,00865	164	0,32	-0,06258
12	0,875	0,033169	63	0,11	0,073862	114	0,002	-0,00923	165	0,33	-0,0626
13	0,85	0,039603	64	0,1	0,070334	115	0,003	-0,01118	166	0,34	-0,06256
14	0,825	0,046004	65	0,095	0,068489	116	0,004	-0,01273	167	0,35	-0,06246
15	0,8	0,052337	66	0,09	0,066584	117	0,005	-0,01403	168	0,36	-0,06229
16	0,775	0,058566	67	0,085	0,064617	118	0,006	-0,01516	169	0,37	-0,06204
17	0,75	0,064656	68	0,08	0,062583	119	0,007	-0,01617	170	0,38	-0,06172
18	0,725	0,070573	69	0,075	0,060478	120	0,008	-0,0171	171	0,39	-0,0613
19	0,7	0,076285	70	0,07	0,058297	121	0,009	-0,01795	172	0,4	-0,06078
20	0,675	0,081773	71	0,065	0,056032	122	0,01	-0,01875	173	0,41	-0,06014
21	0,65	0,087012	72	0,06	0,053676	123	0,0125	-0,02054	174	0,42	-0,05939
22	0,625	0,091967	73	0,055	0,051218	124	0,015	-0,02211	175	0,43	-0,05854
23	0,6	0,096599	74	0,05	0,048647	125	0,0175	-0,02352	176	0,44	-0,05762
24	0,575	0,100887	75	0,045	0,04595	126	0,02	-0,0248	177	0,45	-0,05663
25	0,55	0,104799	76	0,04	0,04311	127	0,025	-0,02709	178	0,475	-0,0539
26	0,525	0,108299	77	0,035	0,040102	128	0,03	-0,0291	179	0,5	-0,05085
27	0,5	0,11136	78	0,03	0,036899	129	0,035	-0,0309	180	0,525	-0,04754
28	0,475	0,113937	79	0,025	0,033454	130	0,04	-0,03255	181	0,55	-0,04401
29	0,45	0,11599	80	0,02	0,029694	131	0,045	-0,03406	182	0,575	-0,04032
30	0,44	0,11665	81	0,0175	0,027666	132	0,05	-0,03547	183	0,6	-0,03649
31	0,43	0,117211	82	0,015	0,025511	133	0,055	-0,03679	184	0,625	-0,03257
32	0,42	0,117667	83	0,0125	0,023197	134	0,06	-0,03804	185	0,65	-0,02859
33	0,41	0,118003	84	0,01	0,020674	135	0,065	-0,03921	186	0,675	-0,0246
34	0,4	0,118204	85	0,009	0,019587	136	0,07	-0,04032	187	0,7	-0,02066
35	0,39	0,118258	86	0,008	0,018447	137	0,075	-0,04138	188	0,725	-0,0168
36	0,38	0,118168	87	0,007	0,017241	138	0,08	-0,04239	189	0,75	-0,01305
37	0,37	0,117946	88	0,006	0,015955	139	0,085	-0,04335	190	0,775	-0,00947
38	0,36	0,117607	89	0,005	0,014565	140	0,09	-0,04427	191	0,8	-0,00612
39	0,35	0,117159	90	0,004	0,013037	141	0,095	-0,04515	192	0,825	-0,00307
40	0,34	0,116603	91	0,003	0,011296	142	0,1	-0,04599	193	0,85	-0,00038
41	0,33	0,115942	92	0,002	0,009227	143	0,11	-0,04758	194	0,875	0,001859
42	0,32	0,115181	93	0,00175	0,008633	144	0,12	-0,04905	195	0,9	0,003536
43	0,31	0,114319	94	0,0015	0,007997	145	0,13	-0,05042	196	0,91	0,004023
44	0,3	0,113356	95	0,00125	0,007312	146	0,14	-0,05169	197	0,92	0,004387
45	0,29	0,112292	96	0,001	0,006555	147	0,15	-0,05287	198	0,93	0,00462
46	0,28	0,111127	97	0,00075	0,005695	148	0,16	-0,05397	199	0,94	0,004702
47	0,27	0,109863	98	0,0005	0,004672	149	0,17	-0,05499	200	0,95	0,004614
48	0,26	0,108497	99	0,0004	0,00419	150	0,18	-0,05593	201	0,96	0,004338
49	0,25	0,107027	100	0,0003	0,003636	151	0,19	-0,05681	202	0,97	0,003829
50	0,24	0,105454	101	0,0002	0,00297	152	0,2	-0,05762	203	0,98	0,003042
51	0,23	0,103774	102	0,0001	0,002104	153	0,21	-0,05837	204	0,99	0,00191
									205	1	0

Figure 5.25 : The coordinates of the airfoil NACA64(3)618.

Python programming language is used for writing codes for panMARE. Figure 5.26 shows an example of a panMARE code used during the analyses.

```
# panMARE.GUI.windowEx(SurfaceModel)

GridGenerator = panMARE.Import.Grid.tGridGenerator()

GridGenerator.AddSurface(SurfaceSS)
GridGenerator.AddSurface(SurfacePS)
#
LeadingEdgeAskKnuckle = True
if LeadingEdgeAskKnuckle:
    GridGenerator.EdgeFlags(SurfaceSS.wEdge(), [panMARE.edgeflagLeading, panMARE.edgeflagKnuckle])
else:
    GridGenerator.EdgeFlags(SurfaceSS.wEdge(), [panMARE.edgeflagLeading])
GridGenerator.EdgeFlags(SurfaceSS.EEdge(), [panMARE.edgeflagTrailing, panMARE.edgeflagKnuckle])

# Tip Edge Flags
GridGenerator.EdgeFlags(SurfaceSS.NEdge(), [panMARE.edgeflagKnuckle])
GridGenerator.EdgeFlags(SurfacePS.NEdge(), [panMARE.edgeflagKnuckle])
# Blade Root Edge Flags
GridGenerator.EdgeFlags(SurfaceSS.SEdge(), [panMARE.edgeflagKnuckle])
GridGenerator.EdgeFlags(SurfacePS.SEdge(), [panMARE.edgeflagKnuckle])

GridGenerator.AssignRefinement(SurfaceSS.SEdge(), aRefinement.Value)
GridGenerator.AssignRefinement(SurfaceSS.NEdge(), aRefinement.Value)
GridGenerator.AssignRefinement(SurfacePS.SEdge(), aRefinement.ReversedValue)
GridGenerator.AssignRefinement(SurfacePS.NEdge(), aRefinement.ReversedValue)

GridGenerator.CreateGrid( aModel, SurfaceSS, aNumberOfPanels,
                          aNumberOfPanelsSpanwise, aFlipNormal=False )
GridGenerator.CreateGrid( aModel, SurfacePS, aNumberOfPanels,
                          aNumberOfPanelsSpanwise, aFlipNormal=True )

FoilName = 'NACA64_A17'
ChordPanels = 14
AoA = 0.
Velocity = 1.
Span = 10.
ChordLength = 1.
Iterations = 100
MaxWakeAge = 100
Density = 1.2250 # kg/m^3 @15deg https://de.wikipedia.org/wiki/Luftdichte
Viscosity = 1.48e-5 # kg/s/m @15deg https://en.wikipedia.org/wiki/viscosity
Threads = 4
TimestepSize = 0.1
SpanPanels = 1

FileName = "{}/.dat".format(FoilName)

Refinement = panMARE.Import.Grid.tExponentialSpacing(
    aStartParameter = 0.18,
    aMidParameter = 1.4,
    aEndParameter = 0.25)

aAngle2 = (AoA + 180.) * np.pi/180.
Global = panMARE.tGlobal()
Global.MotionVel(panMARE.tMatrix4x4.TranslationVel(panMARE.tVector3(-1, 0, 0), velocity))
Global.IsSteady(False)
Global.TimestepSize(TimestepSize)
Global.Density(Density)
Global.Viscosity(Viscosity)

Model = panMARE.tModel(Global, 'Model')
theFoil = panMARE.tLiftingPanelGroup( Model, 'theFoil')

Solver = panMARE.tPottisolver(Global, "solver")
Solver.NumberOfThreads(2)

FoilProfile = panMARE.Tools.turbine.tFoilProfileStandard(aFilename = FileName)
GenerateGridByFoilProfile(aModel = theFoil,
                          aFoilProfile = FoilProfile,
                          aNumberOfPanels = ChordPanels, aNumberOfPanelsSpanwise = SpanPanels,
                          aFoilLength = Span, aChordLength = ChordLength,
                          aRefinement = Refinement)

theFoil.PolygonsToPanels()

# add panel group to solver
solver.AddPanelGroup(theFoil)
```

Figure 5.26: An example of panMARE code.

As mentioned the previous parts, panMARE accepts airfoil as a geometry of the considered body discretized into flat quadrilateral elements. On the discretized body adequate boundary conditions are applied and a linear system of equations is solved to obtain local velocity and pressures distribution on the body. Figure 5.27 indicates the velocity distribution of the airfoil at 1.6×10^5 Reynolds number.

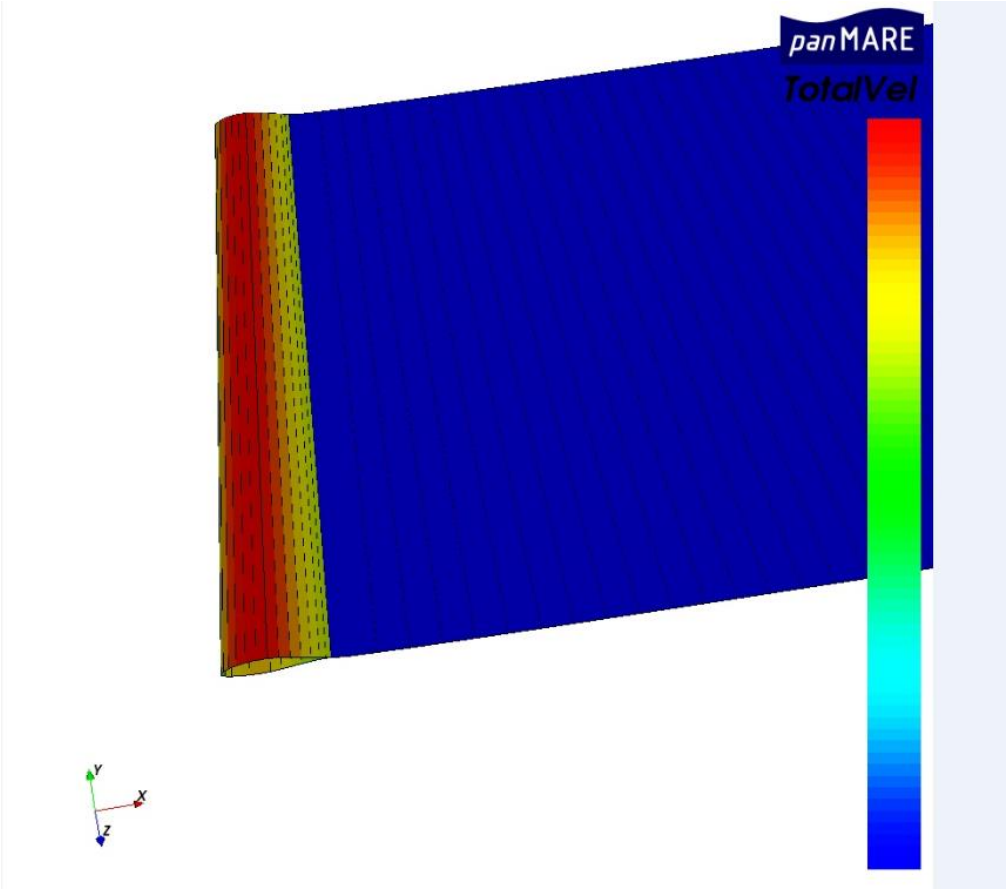


Figure 5.27: The velocity distribution at zero degree (panMARE).

The analyses has been carried out for two different air velocity between 10° - 15° angles of attack. Both the knowledge of Python and panMARE codes are required to write the program to use the solution. The program written in Python works on panMARE computation tool and the solution needed can be obtained immediately.

After the colution of the analyses have been performed, the velocity and pressure distribution around the airfoil can be monitored by using Paraview, multi-platform data analysis and visualization application.

Figure 5.28 and 5.29 show the force and pressure distribution of the airfoil at 1.6×10^5 Reynolds Number in Paraview.

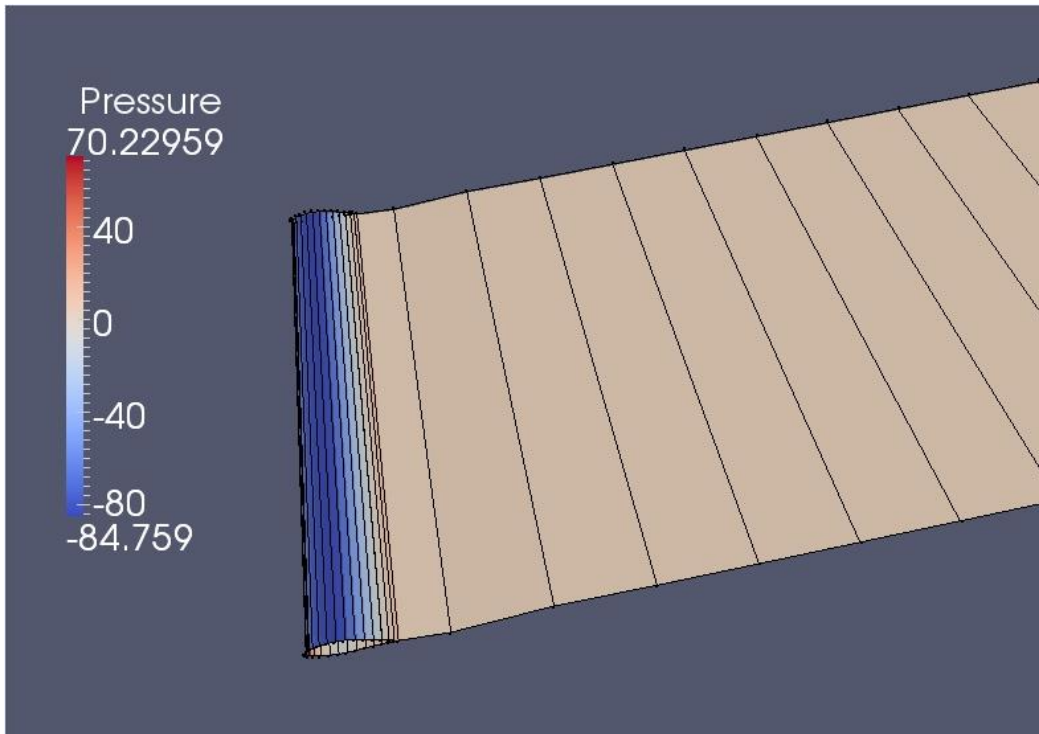


Figure 5.28: The pressure distribution at 5 degrees (panMARE).

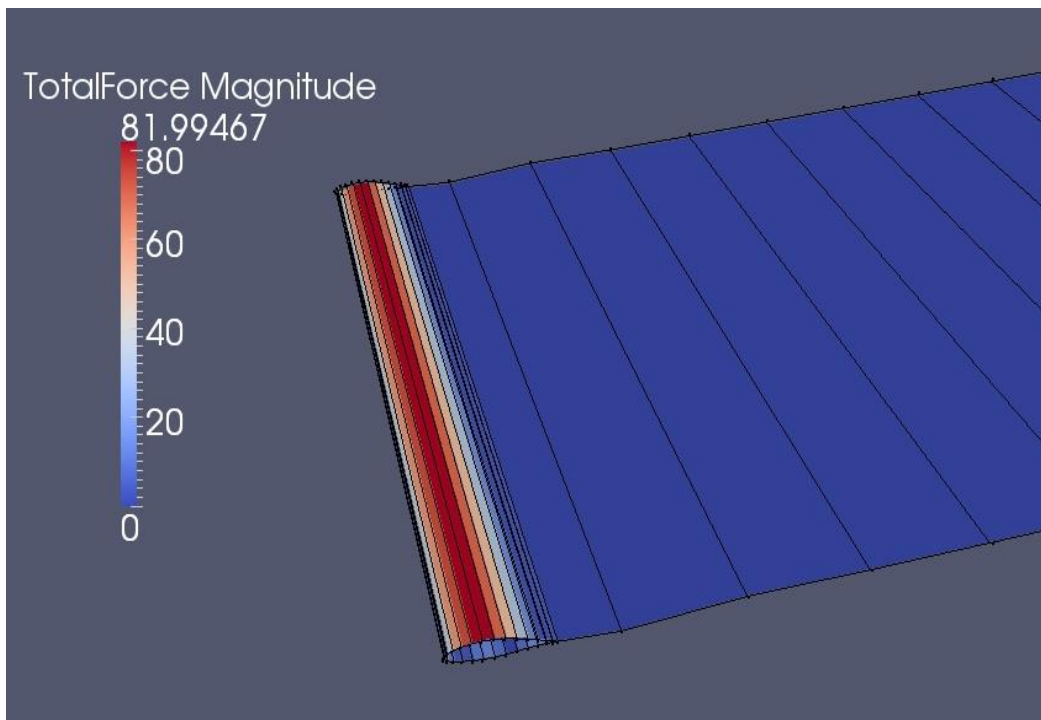


Figure 5.29: The force distribution at 5 degrees (panMARE).

Additionally, by means of the codes added to the program, the data files related to lift coefficient, drag coefficient and forces are obtained for each angle of attack at the end of the analysis. The Table 5.3 includes the data related to the lift and drag forces.

Table 5.3: Lift and drag forces ($Re=4.22 \times 10^4$) (panMARE).

Re=4,22x104		
Angle of Attack(Degrees)	FL(N)	FD(N)
-5	-1,11099	0,141655
-4	-0,50445	0,134514
-3	0,100282	0,12884
-2	0,703073	0,125888
-1	1,30378	0,125596
0	1,902267	0,126606
1	2,498404	0,129231
2	3,092065	0,133414
3	3,68313	0,138808
4	4,271482	0,146777
5	4,857011	0,162407
6	5,439616	0,181217
7	6,019198	0,207992
8	6,595665	0,253373
9	7,168926	0,302347
10	7,738898	0,360787
11	8,3055	0,425323
12	8,868659	0,48008
13	9,428301	0,543843
14	9,984358	0,616699
15	10,53677	0,708221

In Figure 5.30, it is showed the drag coefficient values obtained from analysis of NACA 643618 blade profile for Reynolds numbers 4.22×10^4 and $1,6 \times 10^6$.

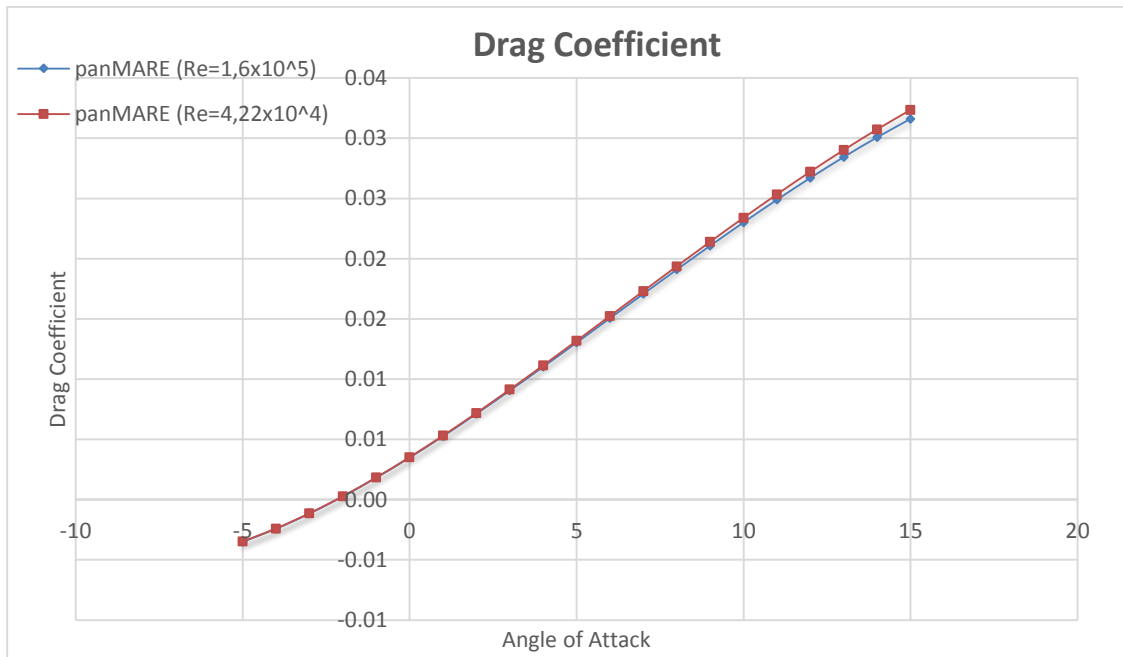


Figure 5.30: Drag coefficients for reynolds numbers 1.6×10^5 and 4.22×10^4 (panMARE).

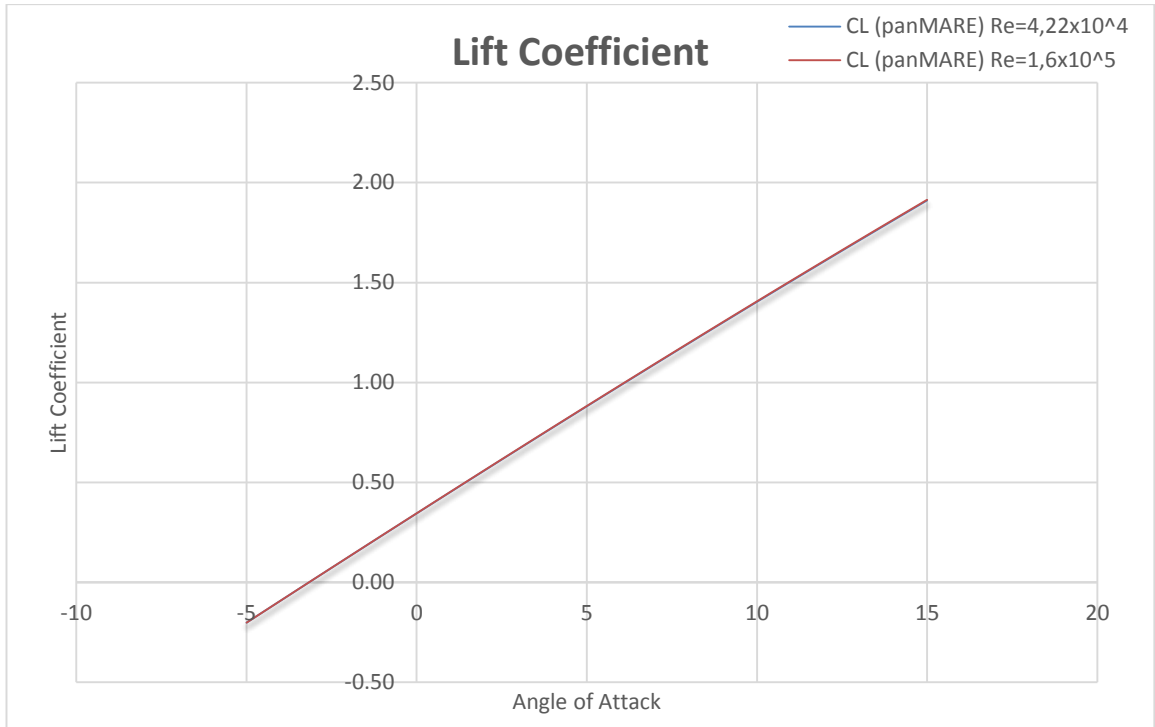


Figure 5.31: Lift coefficients for Reynolds numbers 1.6×10^5 and 4.22×10^4 (panMARE).

In Figure 5.31, the variation of lift coefficient data with regard to the angle of attack are presented. As it can be seen as the graph, the effect of increasing the Reynolds number on lift coefficient is not so much by comparison the influence of the angle of attack.

5.3 Comparison Between The Experimental Data And Numerical Values

In this section the results obtained by *Ansys CFX* and *panMARE* are presented and compared to each other.

The Figures 5.32 and Figure 5.33 refer to the comparison of the lift coefficient values between *Ansys CFX* and *panMARE* for Reynolds Numbers 4.22×10^4 and 1.6×10^5 .

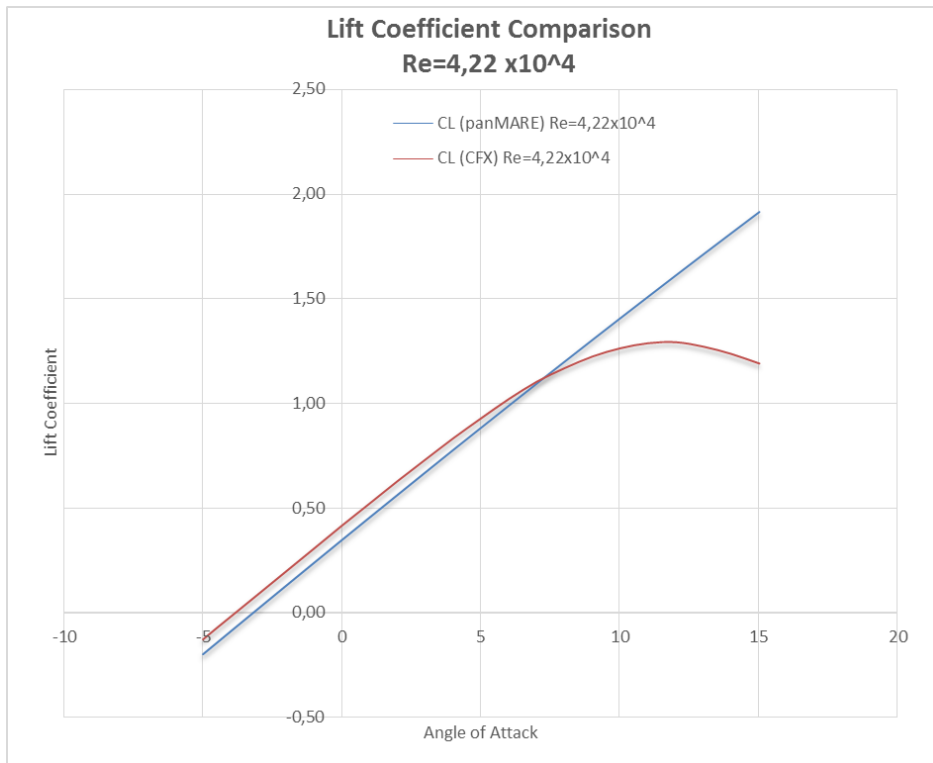


Figure 5.32: The comparison of the lift coefficients ($Re=4.22 \times 10^4$).

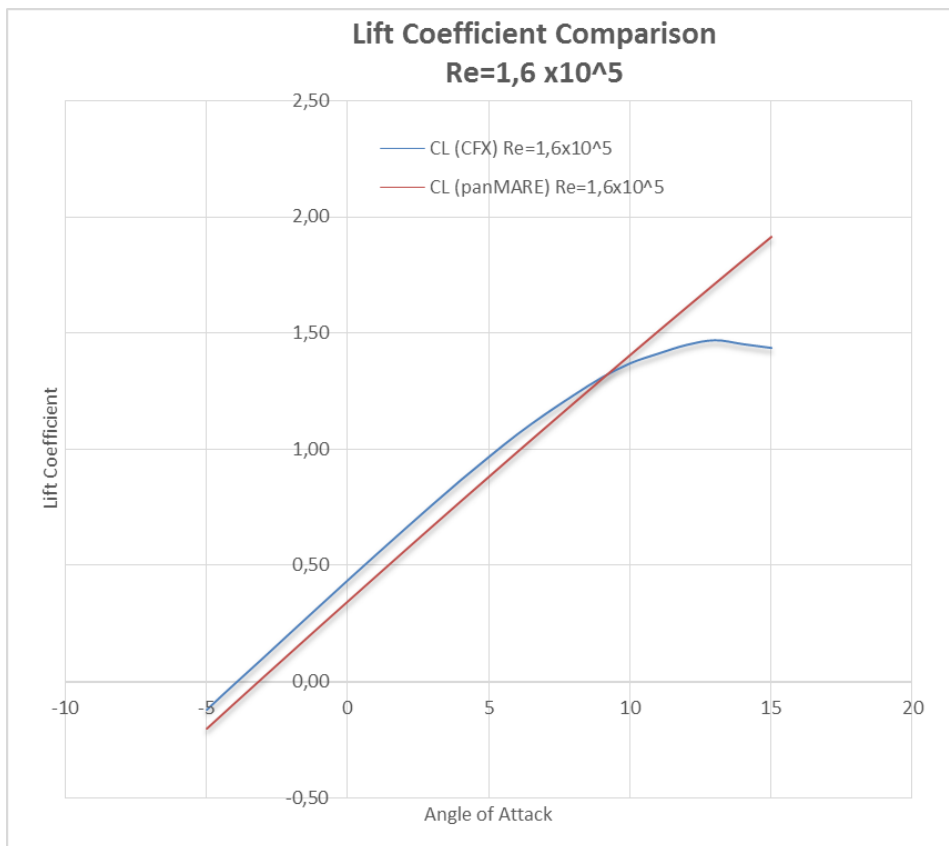


Figure 5.33: The comparison of the lift coefficients ($Re=1.6 \times 10^5$).

It is seen that C_L values in the result of simulation performed with ANSYS CFX and the values found by the program of panMARE are largely in compliance up to about 10° - 11° angle of attack . At 10° angle of attack, Ansys CFX lifting coefficient data is decreased considerably and in panMARE program the increasing of lifting coefficient continues.

After 10° angle of attack, the trueness of the data given by panMARE decreases. The gap between the values goes up later than. The reason for this is to close the stall angle and this causes the increase of the turbulence effect. The angle at which this occurs is called the critical angle of attack. Flow separation begins to occur at small angles of attack while attached flow over the wing is still dominant. As angle of attack increases, the separated regions on the top of the wing increase in size and hinder the wing's ability to create lift. At the critical angle of attack, separated flow is so dominant that further increases in angle of attack produce less lift and vastly more drag. Since viscosity factor is negligible on panMARE program operating according to the panel method, the influence of turbulence which are made by intensified on the blade after the stall angle affects the results. Therefore panMARE providing accurate results in much faster than Ansys CFX at changes in the angle of attack up to stall angle, after this angle it loses its accuracy.

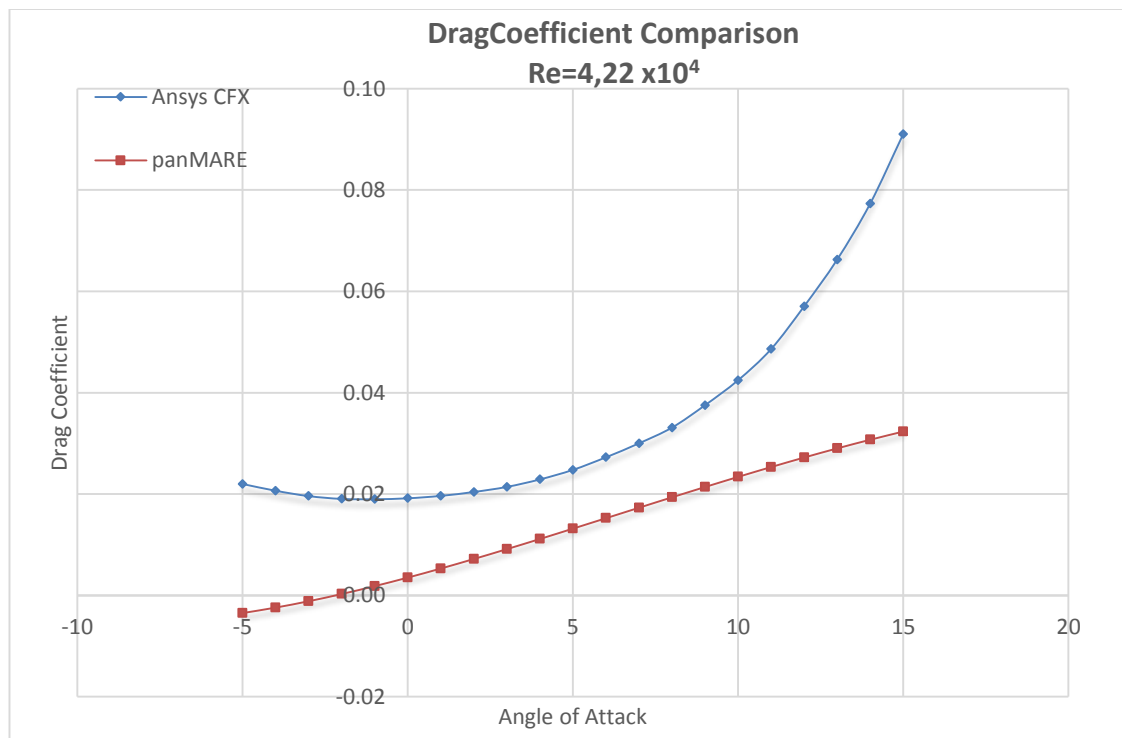


Figure 5.34: The comparison of the drag coefficients ($Re=4.22 \times 10^4$).

In Figure 5.34 and Figure 5.35 it can be said that CD values for both programs are approximate up to the certain angle of attack (6° - 7°). After that, it can be easily realised that there are differences between these values. CD values for panMARE begin to increase faster than Ansys CFX. The gap becomes maximum at 10° angles and this trend continues to the 15° angles of attack.

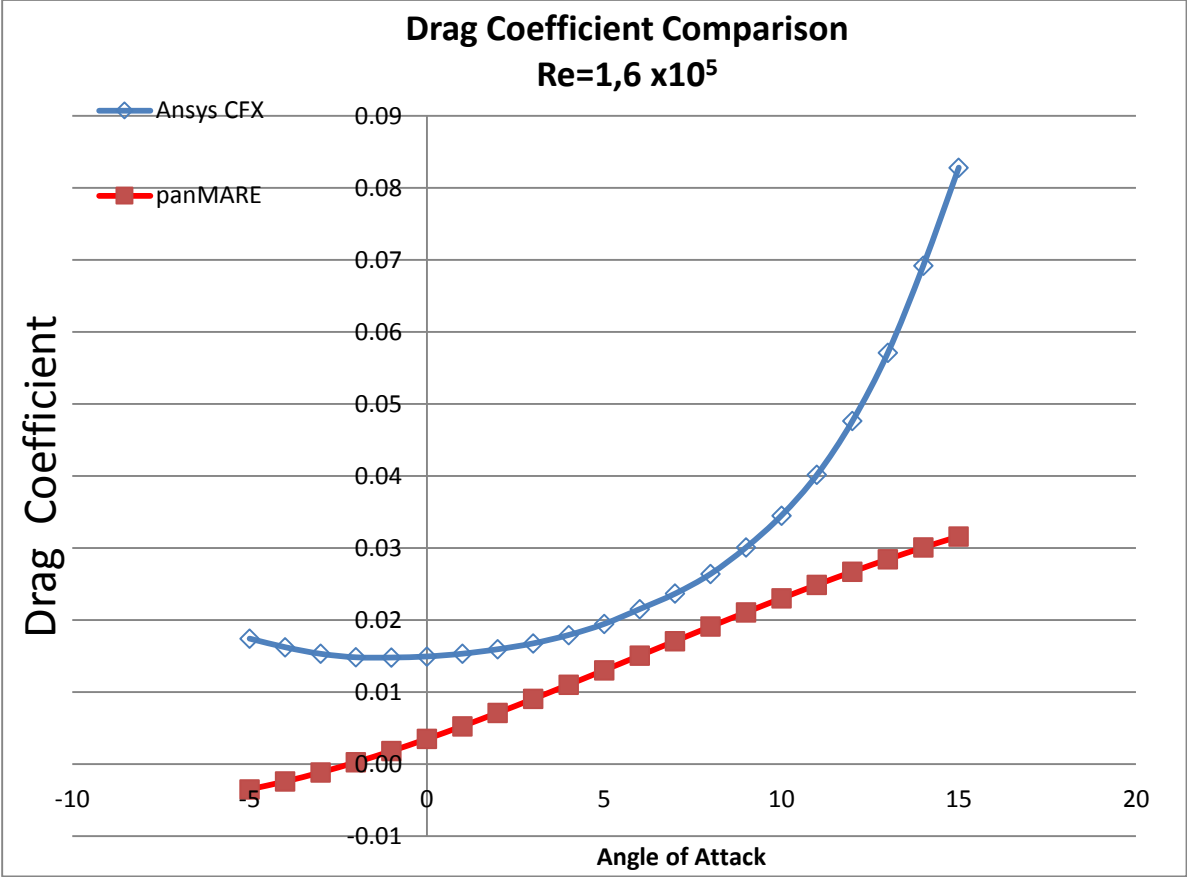


Figure 5.35: The comparison of the drag coefficients (Re=1.6x10⁵).

In order to demonstrate the behaviour of the chosen analysis methods, the results of the experiment carried out related to the flow around a rigid NACA 64₃618 airfoil at Re = 1,6 x 10⁶ for different angle of attack have been used.[30]

For zero angle of attack, the results for C_L deviate less than 1 % as per panMARE. The largest deviation can be found for high angle of attack, where the airfoil is fully stalled.

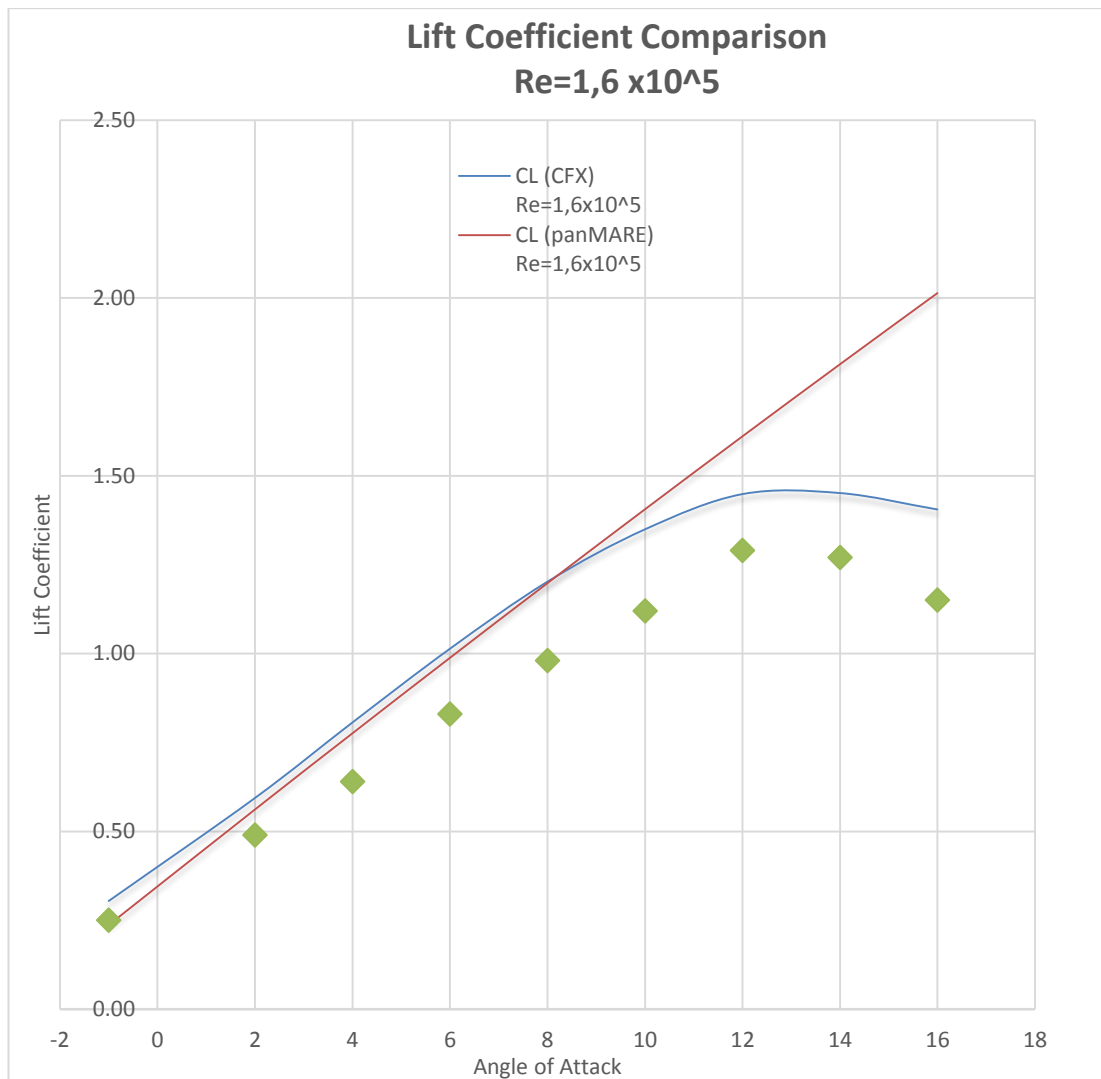


Figure 5.36: Lift coefficient Comparison of NACA 64₃-618(Re = 1,6x10⁵)[33]

As it is evident from Figure 5.36, both *Ansys CFX* program and *panMARE* model produce approximately similar results for low angles of attack which is near the experimental measurements. However for higher angles of attack, *panMARE* analysis has failed to reproduce experimental results, while *Ansys CFX* gives better results as in common with low angles of attack.

Table 5.4: Comparisons between calculated and experimental aerodynamic coefficients, lift coefficient.

Angle of Attack	C_L			
	calc (panMARE)	% error	calc (Ansys CFX)	% error
-1	0,236846496	0,06	0,304729579	0,18
2	0,561676338	0,13	0,594134324	0,18
4	0,775903732	0,18	0,806324744	0,21
6	0,988076448	0,16	1,01356086	0,18
8	1,198044848	0,18	1,201896902	0,18
10	1,405673411	0,20	1,348993131	0,17
12	1,610839984	0,20	1,448067002	0,11
14	1,813434872	0,30	1,451032728	0,12
16	2,013736808	0,43	1,404862964	0,18

Table 5.4 shows that the predicted lift coefficients are accurate to between 10% and 20% according to Ansys CFX analysis. panMARE results are also within 20% until stall angle.

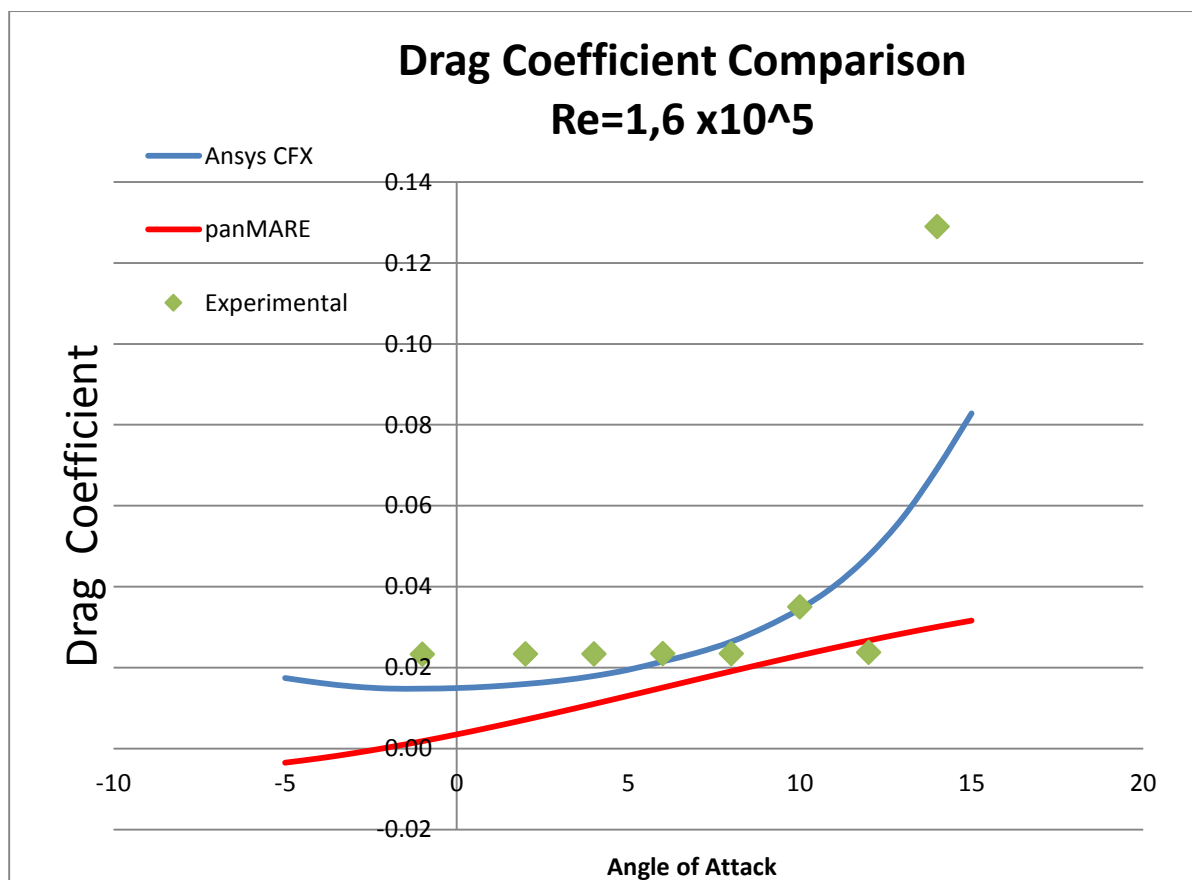


Figure 5.37: Drag Coefficient Comparison of NACA 64₃-618(Re = 1,6x10⁵)[30].

As shown in Figure 5.37, the data given by panMARE and Ansys CFX have compared with the experimental results. The error percentage is calculated based on the results obtained for each angle of attack(see Table 5.5).

Table 5.5 : Comparisons between calculated and experimental aerodynamic coefficients, drag coefficient.

Angle of Attack	CD			
	calc (panMARE)	% error	calc (Ansys CFX)	% error
-1	0,001830473	0,92	0,014808695	0,36
2	0,007136962	0,70	0,015957988	0,32
4	0,011036396	0,53	0,017940953	0,23
6	0,015067682	0,36	0,0215281	0,08
8	0,019103128	0,19	0,026410504	0,12
10	0,023023059	0,34	0,034517144	0,01
12	0,026717042	0,12	0,047634993	1,00
14	0,030085	0,77	0,069219124	0,46
16	0,128007584	0,62	0,082819103	0,05

During the calculations in panMARE analysis, viscous effects are taken into account but not directly. Depending on the kinematic viscosity a break off point is calculated on the panel and a friction force is estimated. But the friction is not taken into account for the calculation of the stream itself.

Due to the missing rotation in potential theory, friction effects can not be computed directly. Instead of this, empirical correlations are used in panMARE to determine the friction forces.

Kinematic viscosity is taken as 1.48×10^{-5} for air at 15°C by using Sutherland's formula. panMARE provides one resulting force dF_k for each panel k acting on the midpoint of this panel. This force contains both a part due to pressure and an empirically estimated part due to friction. Let $N_{\text{panel}} = N_B$ be the number of panels and NCV the number of control volumina in the viscous fluid domain. x_k is the current position of the force application point on the k_{th} panel, and x_m is the position of the vertex which the m_{th} control volume dV_m is constructed around. The task is to convert the distribution of N_{panel} panel acting forces into a distribution of volume-specific forces.

For each force application point k , a routine looks for the control volumes situated in the vicinity of the point k . For this purpose it is checked whether the grid vertex m lies

in an imaginarily drawn sphere with the radius r_{smt} around the point k . Respectively, the factor $a_{k,m}$ is defined as follows: (Eq. 5.1)

$$a_{k,m} = 1 \text{ if } \|x_m - x_k\| \leq r_{smt} \quad (5.1)$$

$$a_{k,m} = 0 \text{ if } \|x_m - x_k\| > r_{smt}$$

Finally, the m th control volume is charged with the volume specific force f_m (5.2):

$$f_m = \sum_{k=1}^{N_{panel}} a_{k,m} \frac{dF_k}{V_k} \quad (5.2)$$

with

$$f_m = \sum_{m=1}^{N_{cv}} a_{k,m} dV_m$$

being the sum of all control volumes within the sphere of the radius r_{smt} around x_k .

5.4 Cell Count Dependence Study

Choosing a mesh with the optimal number of cells in order to do a CFX simulation is very important. This optimal is based on both accuracy of the results and speed of the solution to converge. The meshes used for the different simulations performed have between 50.000 and 80.000 cells. Then some refinement is done in order to check how the number of cells affects the accuracy of the solution.

In Figure 5.38 it is shown the mesh dependence study for an angle of attack of 2 degrees. It is shown that decreasing the amount of cells to half of the number of cells used, yields higher differences than the ones obtained while making the different refinements.

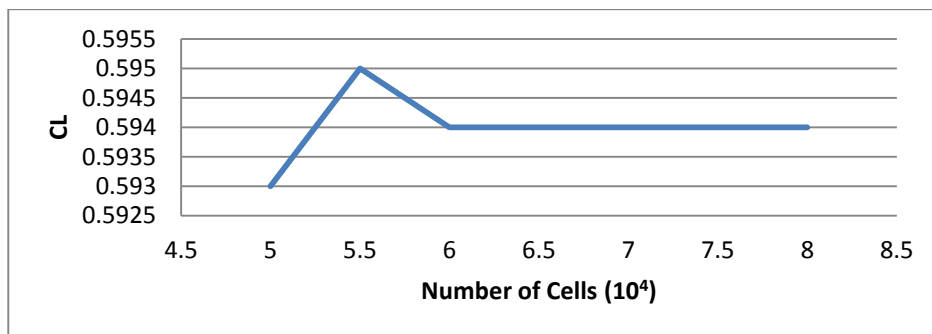


Figure 5.38: Mesh dependence study for the NACA643618.

6. CONCLUSIONS AND RECOMMENDATIONS

In this study, numerical analyses of the blade profile NACA 64(3)618 have been performed separately on Ansys CFX and on panMARE in the range of determined values -5° and 15° degrees of angle of attack, and in two different wind velocities. (3m/s, 11.4m/s)

The results obtained from numerical simulations are summarized below:

-In Ansys CFX numerical simulations, it has been determined that when the angle of attack of NACA 64(3)618 is increased from 0° to 13° , the lift coefficient values of the profile increase regularly. At 13° angle of attack these lifting coefficients show a sudden reduction (stall occurs). The airfoil reaches a stall condition, where the pressure distribution on the top and bottom are equal and a reduction in the lift coefficient is generated by the foil.

- In Ansys CFX numerical simulations, it has been determined that when the angle of attack of NACA 643618 blade profile is increased from 0 to 11° , the drag coefficient values of the profile increase regularly and between 11° - 15° angle of attack these drag coefficients show a sudden significant increase.

- In numerical analysis made in the programs; panMARE, based on panel method, and Ansys CFX, working according to RANS method, it was determined that the measured lift coefficient values are compatible between 0° and 10° angles in the range of different angles of attack of NACA 643618 blade profile.

-However, panMARE can reach the correct results up to stall angle much faster than ANSYS CFX, since neglecting the viscosity in the calculation method, it loses their accuracy after this angle. However, the reliability of this method can be said for certain intervals, panMARE is still high availability method within mostly used angle of attack area.

-The changes to be made in the code for each changing model is sufficient on panMARE, whereas it is necessary for Ansys Cfx to create the model, to be entered

the coordinates again for each model, and to generate mesh appropriately for the geometry. Although composing the program written for Panel Method takes time, after making once it can be gotten the results in a short time for each blade profile provided that requested speed and the angle of attack are entered. This demonstrates the practicality of the method.

-Consequently air flow calculations around the airfoil made by using Panel Method with the contribution of panMARE program, it provides fast and accurate solutions in a particular area.

Suggestions:

The consideration of the following cases is thought to be useful for the numerical and experimental studies which will be made in the future and which are related to blade profile:

-Different angle of attack and analysis can be done using the Reynolds number values for the numerical and experimental studies.

-The changing of aerodynamic coefficients on a different wing profiles can be studied experimentally and numerically.

-The effects of the flight control surfaces on the airfoil such as Flap and slat that provides the lifting at high angles of attack can be examined .

-The effects of different turbulence models can be studied in numerical study.

REFERENCES

- [1] **U.S. Gov, Dept. of Energy. Energy Information Administration**, (2009), Official Energy Statistics from the U.S. Government. <http://www.eia.doe.gov>
- [2] **DOE**, (2009). U.S. Fossil Energy. <http://www.fossil.energy.gov/index.html>
- [3] **U.S. Gov, Dept. of Energy. U.S. Dept. of Energy on Green House Gases**. (2009), <http://www.eia.doe.gov/bookshelf/brochures/greenhouse/Chapter1.html>
- [4] **Digraskar, Dnyanesh, A.** (2010). Simulations of Flow over Wind Turbines, University of Mumbai, UK.
- [5] **El-Wakil, M.M.**, (1998). Power Plant Technology, (McGraw – Hill Book Company, New York), pp. 589-590.
- [6] **Golding, E.W.**, (1977). The Generation of Electricity by Wind Power, (E.& F.N.Spon Ltd., London).
- [7] **Bischoff M., Wall WA, Bletzinger K-U, Ramm E.**, (2004). Models and finite elements for thin-walled structures. In Encyclopedia of Computational Mechanics, Volume 2: Solids, Structures and Coupled Problems, Stein E, de Borst R, Hughes TJR (eds), Chapter 3. Wiley: New York.
- [8] **C.Lins, L.E.Williamson, S.Leitner, S. Teske**, (2015). 10 Years of Renewable Energy Progress, REN21 Renewable Energy Policy Network for the 21st Century.
- [9] **M. Bilgili, A. Yasar and E. Simsek**, (2011). “Offshore wind power development in Europe and its comparison with onshore counterpart” , Renewable and Sustainable Energy Reviews 15.
- [10] **European Wind Energy Association**, (2009). “Wind Energy – The Facts”. Earthscan;
- [11] **Sathyajith, M.**, (2006). Wind Energy: Fundamentals, Resource Analysis and Economics, Springer, Netherlands.
- [12] **Fernando D. Bianchi, Hernán de Battista, Ricardo J. Mantz**, (2006). Wind Turbine Control Systems: Principles, Modelling and Gain Scheduling Design
- [13] **Hau, E.**, (2005). Wind Turbines-Fundamentals, Technologies, Application, Economics. 2nd edition. Springer.
- [14] **Ackermann, T.**, (2005). Wind Power in Power Systems. 1st edition, Wiley.
- [15] **Zaira Izaguirre Fernandez**, (2010). Offshore Wind Energy, Technical Aspects and Feasibility Study of Offshore on Spanish Coasts.

- [16] **EWA, The European Wind Energy Association**, (2014). The European Offshore Wind Industry- Key Trends and Statistics 2013
- [17] **EWA, The European Wind Energy Association**, (2015). The European Offshore Wind Industry- Key Trends and Statistics 2014
- [18] **Bonnie Ram**, (2006). Energy from Offshore Wind, Energetics, Inc. Washington D.C
- [19] **Fulton, G.R.**, (2006). Malcolm, D.J. and Moroz, E.; “Design of a SemiSubmersible Platform for a 5MW Wind Turbine”
- [20] **Musial, W.D.; Butterfield, C.P.**, (2005). “Deepwater Offshore Wind Technology Research Requirements”, Windpower 2005 Poster Presentation, May 15-18, Denver, CO
- [21] **Karna S. Patel, Saumil B. Patel, Utsav B. Patel, Prof. Ankit P. Ahuja**, (2014). CFD Analysis of an Aerofoil”. International Journal of Engineering Volume No.3
- [22] **Whitcomb, Richard T.**, (1974). Review of NASA Supercritical Airfoils. ICAS Paper No. 74-10.
- [23] **Frederick H. Lutze.**, (2015). Airfoil and Wing Properties, Basic Aerodynamics Lecture Notes.
- [24] **W.H. Mason.**, (1997). Applied Computational Aerodynamics, Appendix A Geometry for Aerodynamicists
- [25] **M. Bauer, M. Abdel-Maksoud**, (2012). A 3-D Potential Based Boundary Element Method for the Modelling and Simulation of Marine Propeller Flows, Vienna, Austria
- [26] **J. Katz, A. Plotkin**, (2001). Low-Speed Aerodynamics, Cambridge University Press, Cambridge
- [27] **ANSYS Inc.**, (2010). ANSYS CFX Brochure.
- [28] **Anderson, J.D.**, (1995). Computational Fluid Dynamics: The Basics with Applications McGraw-Hill, New York, NY, USA
- [29] **ANSYS. Gambit**, (2008). Computational Fluid Dynamics Preprocessor from Fluent. <http://www.fluent.com/software/gambit/>
- [30] **M.P.Thake**, (2011). Investigation of a Laminar Airfoil with Flow Control and the Effect of Reynolds Number, Ohio State University.

CURRICULUM VITAE



Name Surname: Sertaç Bulut

Place and Date of Birth: Çanakkale 09.12.1985

E-Mail: bulutse@itu.edu.tr

EDUCATION:

B.Sc.: Istanbul Technical University (2005-2010)